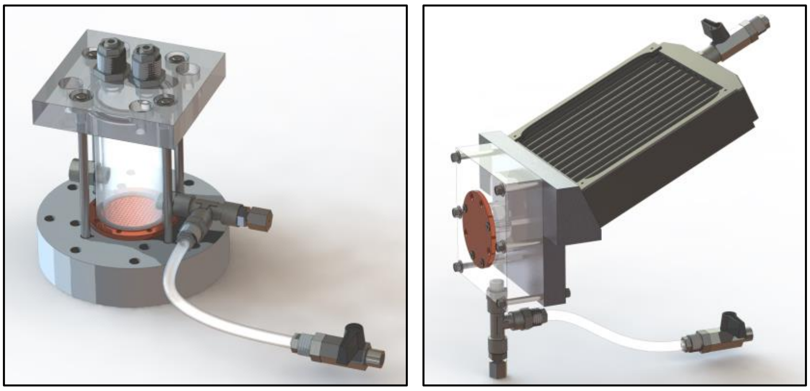

Test and optimization of a two-phase thermosyphon cooling system for microprocessors under real working conditions

Vasco Tavares Brito e Abreu

Thesis to obtain the Master of Science Degree in

Mechanical Engineering

Supervisors: Prof. António Luís Nobre Moreira

Dr. Ana Sofia Oliveira Henriques Moita

Examination Committee

Chairperson: Prof. Edgar Caetano Fernandes

Supervisor: Dr. Ana Sofia Oliveira Henriques Moita

Member of the Committee: Prof. José Maria Campos da Silva André

June 2017

Acknowledgements

Gostaria primeiro de agradecer muito sinceramente aos meus orientadores Professor Doutor Luís Nobre Moreira e Doutora Ana Moita, pelo apoio incessante, paciência, e abertura de espírito, além de um grande sentido de tranquilidade e confiança. De seguida gostaria de agradecer ao Engenheiro Miguel Moura e ao Emanuele Teodori, que pavimentaram o caminho deste trabalho, e em especial ao Miguel, cujo contributo inicial e apoio constante foram essenciais para a sua conclusão. Sem eles esta dissertação não teria sido nunca realizada.

Agradeço às oficinas do IN+ e do NOF que me ajudaram a produzir os componentes essenciais do protótipo, com mestria e rapidez singulares; à Acrilfer de São João da Talha por ter fornecido o material necessário; ao Senhor Venes da Cenfim, no Beato, que proporcionou uma semana divertida de aprendizagens e me dotou da arte de tornear e fresar, essenciais para a posterior manufatura de peças do protótipo; à AquaPC do Areeiro que também forneceram o radiador e a massa térmica usados neste projeto; à Veda Mais que me ajudou com os inúmeros O-rings; à LEDs & Chips pelo filamento de impressão 3D fornecido; aos Professores Relógio Ribeiro e Luís Sousa pelo apoio prestado na impressão 3D.

Um muito obrigado à Mãe, a minha fonte primária de apoio, motivação e energia, que torce verdadeiramente e acredita profundamente na minha competência para com esta missão e que me oferece tantos momentos de descontração, descanso e divertimento.

Agradeço à Olga e ao Pai, que sempre me apoiaram ao longo do curso, me mostraram os caminhos de excelência na investigação, além de me terem continuamente lembrado de atacar esta missão com todas as minhas forças, nos momentos em que a mente deambulava por outras vias. De forma alguma teria terminado esta tese sem eles.

Dedico esta dissertação aos meus queridos irmãos António, Guilherme e Mariana, cujas inúmeras conquistas pessoais e académicas me inspiram e motivam continuamente. Fui verdadeiramente abençoado por os ter na minha vida.

Aos meus amigos, companheiros de curso ou colegas de laboratório, Tiago, Gonçalo, Diogo, Filipa, Pedro, Artur, Inês, Dalila, Joana e Nuno, gostaria de agradecer os inúmeros momentos de lazer vividos quer seja nos almoços algures pelo Técnico, quer por todos os outros momentos de enriquecedora e inesquecível partilha, além do apoio incondicional e mútua distribuição da carga emocional relacionada com as responsabilidades académicas e, mais recentemente, este projeto de tese.

A Santa Cecília e Appolo líder das Musas, padroeiros guardiões da Música, essa, que me comanda a vida e é parte da sua essência, que me acompanhou durante os longos meses desta tese, assim como em todas as outras jornadas da vida, fico eternamente grato.

Finalmente, agradeço à Fundação para a Ciência e a Tecnologia (FCT) pelo apoio financeiro a esta investigação no âmbito do projeto RECI/EMS-SIS/0147/2012 e pela atribuição de uma bolsa de investigação.

Abstract

The present work features the test and optimization of a two-phase thermosyphon cooling system for microprocessors, initially validated at simulate boundary conditions and later tested on a real CPU, under stress operation. Microcavities arrays are structured on the thermosyphon hot surface, for nucleate pool boiling enhancement. The inter-cavity distance, S is the tested parameter with surfaces ranging from S = 100 µm to S = 600 µm and a smooth surface as reference. This set of surfaces is tested both for a horizontal and a vertical surface orientation, at steady-state and transient conditions. The working fluid is 3M's Novec HFE-7000, a dielectric engineering liquid.

Results have shown the effect of structuration is more noticeable for the horizontal orientation, with an average 14°C wall superheat differential between the smooth surface and any structured surface during nucleate pool boiling, whereas for the vertical situation, there is no differential. Smaller cavity distance, S resulted in lower wall superheat for both orientations. Cavities also promoted an earlier onset of pool boiling. For the vertical oriented prototype, results account heat transfer coefficient improvement to be stronger and correlated with a reducing S parameter. Transient tests have shown the critical design parameter for such systems to be the stabilized steady state temperature.

Optimal results were obtained with the smallest parameter, S = 100 µm, suggesting further research with smaller S parameters.

The final proof of concept application on a real processor was successfully demonstrated, with an average 5°C reduction and a lower thermal response time than the conventional cooling fan, during stress test. Results are thus beneficial for microprocessor performance and lifespan.

Keywords

Thermosyphon, CPU cooling, pool boiling, micro-cavities, heat transfer coefficient enhancement, product development.

Resumo

Este trabalho compreende o teste e otimização de um termossifão, para arrefecimento de microprocessadores, inicialmente validado em condições de fronteira simuladas e mais tarde testado numa unidade de CPU. Padrões de microcavidades são estruturados na superfície do termossifão que dissipa o calor gerado no CPU, com o objetivo de melhorar a ebulição nucleada em meio quiescente no seu interior. A distância entre cavidades, S, é o parâmetro de teste para avaliar superfícies que variam de S = 100 µm a 600 µm e uma superfície lisa como referência. Este conjunto de superfícies é estudado nas orientações horizontal e vertical, em estado estacionário e transiente, para uma completa caracterização sistema. O fluido de trabalho usado é o HFE-7000, um líquido de engenharia dielétrico.

Os resultados mostram que o efeito da estruturação é mais notável na orientação horizontal, com um diferencial médio de 14°C entre a superfície lisa e qualquer superfície estruturada, em regime de ebulição nucleada. Para a orientação vertical, este diferencial não existe. As mais pequenas distâncias S resultaram num mais baixo sobreaquecimento da superfície para ambas as orientações. As cavidades promoveram uma mais precoce ativação da ebulição nucleada. Para a orientação vertical, resultados apontam para uma mais notável e correlacionada com a redução de S melhoria do coeficiente de transferência de calor. Resultados otimizados foram obtidos com a superfície S = 100 µm, o que sugere a continuação desta investigação com malhas de cavidades ainda mais finas.

A demonstração conceptual final a um microprocessador real foi realizada com sucesso, com uma redução de temperatura média de 5°C, e um mais baixo tempo de resposta térmica em teste de desempenho, quando comparado com uma ventoinha de arrefecimento convencional. Estes resultados são benéficos para o tempo de vida e desempenho do microprocessador.

Palavras-chave

Termossifão, arrefecimento de microprocessadores, ebulição em meio quiescente, microcavidades, otimização do coeficiente de transferência de calor, desenvolvimento de produto.

Table of contents

List of figures

List of tables

Nomenclature

Acronyms

ABS	Acrylonitrile butadiene styrene
AD	Analog to digital
AI	Analog input
AO	Analog output
BSPT	British standard pipe taper
CAD	Computer-aided design
CHF	Critical heat flux
CPU	Central processing unit
DAQ	Data acquisition
EP	Ethylene propylene
EPDM	Ethylene propylene diene monomer
FC	Fluorocarbon
FSO	Full scale output
GUI	Graphical user interface
HFE	Hydrofluoroether
IC	Integrated circuit
IHS	Integrated heat spreader
MOSFET	Metal-oxide-semiconductor field-effect transistor
NOF	Núcleo de oficinas (IST)
OEM	Original equipment manufacturer
PEEK	Polyether ether ketone
PID	Proportional-integral-derivative
PIV	Particle image velocimetry
PLA	Polylactic acid
PTFE	Polytetrafluoroethylene
PVC	Polyvinyl chloride

RAM	Random-access memory
RPM	Rotations per minute
TDP	Thermal design power
USB	Universal serial bus
VGA	Video graphics array

Latin letters

C	Constant in eq. 3.5	-
c_p	Specific heat	J/kg.K
C_{sf}	Empirical fitting constant in Rohsenow's correlation, eq. 3.4	-
E	Error	-
g	Acceleration of gravity	m/s^2
h	Heat transfer coefficient	W/m^2.K
h_{fg}	Latent heat of vaporization	J/kg
I	Electric current	A
k	Thermal conductivity	W/m.K
L	Characteristic length as in eq. 3.2	m
m	Empirical fitting constant in Rohsenow's correlation, eq. 3.4	-
n	Empirical fitting constant in Rohsenow's correlation, eq. 3.4	-
Nu	Nusselt number	-
p	Pressure	bar
P	Electrical power	W
Pr	Prandtl number	-
q	Heat transfer rate	W
q''	Heat flux	W/m^2
R	Thermal resistance, Electrical resistance	K/W, Ω
R_a	Roughness parameter	mm
R_b	Bubble radius as in eq. 3.3	m
S	Cavity distance parameter	µm
T	Temperature	K, ºC
U	Uncertainty	-
V	Voltage	V

Greek symbols

β	Transistor current gain parameter	-
μ	Viscosity	N.s/m^2
ρ	Density	kg/m^3
σ	Surface tension	N/m

Subscripts

amb	At ambient conditions
B	Burdon high-precision resistors
c	Control
CE	Collector-emitter
cp	Converted power source voltage
cur	Current
d	Divided
f	Fluid
in	Input
j	Junction, Joule effect
l	Liquid phase
max	Maximum
min	Minimum
NB	Nucleate boiling
out	Output
ps	Power source
S	From sensor
sat	At saturation conditions
sur	Surroundings
T	Transistor
v	Vapour
w	Wall

1. Introduction

This chapter intends to give an overview on the thesis scope. The context and motivation are introduced followed by the objective which outlines the development of this work in all its stages. To finish, a brief paragraph introducing the organization of the document is presented.

1.1. Context and motivation

Since the very first emergence of the transistor, processors have gone through a continuously growing development, either at its shape and size, or at the number of transistors they contain. In 1965, Gordon Moore, co-founder of Intel, foresaw the number of transistors in an integrated circuit (IC) would approximately double every 2 years (Moore's Law, [1]). These predictions have held true up to today, and became one of the driving principles of the semiconductor industry. In fact, by 1965, the minimum production cost figures were at about only 50 transistors per circuit. 10 years later, in 1975, those figures were already as big as 65 thousand, and today we have devices which exceed thousands of millions of transistors.

However, Gordon Moore himself [1] has pointed out a thermal management issue, raising the question to whether it will or not be possible to remove the heat from tens of thousands of components in a single silicon chip. He argued that, due to the two-dimensionality of these chips, there will be an available surface for cooling close to each centre of heat generation (transistors). As we move towards billion transistor microprocessors, the growing power dissipation of these chips must be conveniently addressed.

Besides the thermal management requirements, microprocessor junction temperature must be addressed too. It should be maintained to maximum values ranging from 85 to 100ºC, or lower depending on specific purpose applications, in order to avoid damage and lifespan shortening. Additional common issues to address during thermal design phases are the existence of hot-spots within a CPU (Central Processor Unit) core surface and insufficient heat exchange surface area availability for common employed technologies. Besides the CPU, more components within a computer architecture will often need or benefit from cooling too, such as the VGA (Video Graphics Array) card, the motherboard's chipset, the RAM (Random Access Memory) or the Hard disk drive, requiring for a more complex integrated solution. Some modern liquid cooling commercial solutions are able to cool down these multiple components.

With ever-increasing chip heat fluxes, new cooling solutions have been developed during the past couple of decades, such as microchannel cooling, impingent liquid jet cooling, liquid spray cooling, immersion cooling, thermosyphons and vapour chambers. These technologies share the characteristic of high heat flux absorption rates at low temperature variation, benefitting from substance phase change latent heat of vaporization, being addressed as two-phase cooling technologies. However, some exhibit quite a complex implementation approach while others are more practical and affordable. The thermosyphon is a simple system in particular, yet very efficient due to the high heat exchange potential at a fully developed nucleate pool boiling regime, and it is sustainable, requiring no pumping power and only an electric 12V fan to force air convection through a condenser.

With the choice of thermosyphons as the technology to develop for the current work and following the previous context, this work intends to proceed the previous efforts by Moura within his master's thesis project [2], on the design and development of a pool boiling thermosyphon CPU cooling system. As he took the first steps in the development of the proposed product, going through the first stages of functional design, this work now follows it further into the test and optimization phases, as well as improving some design concepts.

1.2. Objective

Having introduced the context which frames the proposed work, the main objective is now presented.

The work comprises a number of tasks which are divided in two major parts, being the first a systematic study which precedes the final tests of the system under real working conditions.

The systematic study concerns the characterization of the thermosyphon's evaporator component by evaluating the Critical Heat Flux (CHF) and Heat Transfer Coefficient (h) achieved for each configuration, when the surfaces of the evaporator and of the Integrated Heat Spreader (IHS - the surface which dissipates the thermal load from the processor) are micro-structured.

The micro-structured test surfaces are composed by regular square matrix patterned cavities, etched by laser, with a fixed size and depth. The tested parameter is the distance between cavities [3]. Following the results reported in [2], [3], numerous micro-structured surfaces will be tested, to identify the distance between cavities allowing the highest CHF and h, thus leading to the lowest absolute thermal resistance. Preliminary tests will be performed for the evaporator working on the horizontal position, to validate the measurements for this new experimental campaign, but the remaining will mainly address a configuration in which the evaporator is fixed in the vertical position, as this will be its actual working position in the final tests, being the condenser in a reflux configuration through all stages of this work.

At this stage, tests are performed under well-defined boundary conditions (e.g. well-defined imposed power values). This study will provide the best performing micro-pattern and design modifications to adapt the evaporator to the new orientation.

Finally, the system will be tested in a processor working under real conditions. For this part of the work the candidate will consider the assembly of the improved system to a real processor and evaluation of its cooling performance under typical and full CPU load real working conditions.

1.3. Document organization

The present document features seven main chapters, being chapter 1 the current introduction.

Chapter 2, State of the art, introduces a comprehensive literature review on the most recent advances in CPU cooling technologies, thermosyphons and enhanced pool boiling, under current wide research, to garner the reader with a framework related to the current work and to better understand the developed cooling system and all its features and components.

Chapter 3, Theoretical background, introduces the main physical phenomena involved in the function of the devised system, relevant for its design of the cooling system as well as for interpreting and discussing the results in the later chapter 6.

Chapter 4 covers the Design and optimization of the thermosyphon system, where manufacturing challenges and how they were overcome is introduced, besides the justified option for the cooling liquid and the CPU thermal simulation solution for further experimental tests.

Chapter 5 introduces the Experimental Methodology followed through the realization of the work's different tasks. A special focus is given to the control of acquisition and actuation instruments and signal processing with tools such as LabVIEW or QuickDAQ. Typical experimental tests are also described in all their steps, carefully registered for repeatability, for different experimental situations.

Chapter 6, Results and discussion finally presents the outcome of the many experimental approaches during the current work, with their respective analysis and interpretation, while chapter 7 wraps-up with final Conclusions and future work suggestions.

2. State of the art

The present chapter introduces the current literature state of the art on various topics related to the present work, such as microprocessors cooling strategies, two-phase thermosyphons development, pool boiling enhancement recurring to surface modification and pool boiling in vertical surfaces.

2.1. Microprocessor cooling strategies

In 2003, Hennessy and Patterson [4] observed how heat dissipation by electronic devices was increasing, due to the exponential increase of transistors in continuously reduced chip sizes. While the first microprocessors consumed less than one Watt, an Intel 32 GHz Pentium 4 Extreme Edition consumes 135 Watts, and this heat must be dissipated, through often quite small microprocessor cores, sometimes with 1 cm side or less. The authors finally stated that the limits of the heat flux that could be cooled by air were being reached and that heat dissipation was then the major limitation to using transistors [4]. Brooks and Martonosi [5] also stated the performance benefits brought by the increasing number of transistors in chips were gradually becoming over-shadowed by increased design complexity and heat dissipation.

Excessive temperature was also mentioned as one of the main issues to address. Temperatures should be kept under maximum values of around 85°C. Exceeding temperatures might bring along issues as solder joints melting, laminate out-gassing, oxidation or materials migration, shortening the life-cycle of the microprocessor, and increasing their failure frequency [6], [7]. Other authors, as Peterson [8], state the frequency of chip failures induced by thermal crisis increases exponentially with the chip temperature, over recommended values (70 – 85ºC). Both the previous author and Tonapi et al. [9] state an increase in 10 to 15ºC could reduce chips lifespan by half.

Another common issue is the existence of hot-spots over dissipation surfaces, instead of an even thermal distribution. These hot-spots are small in size, large in amplitude (heat flux) and transient, meaning that they change their location and fluxes through time [10]. This requires solutions to be designed for a worst-case scenario. In the early 2000s, the usual response from manufacturers was to increase the size and exchange surface area of their heat sinks, as well as their weight and flow rates [10]. However, latest years brought further increases in heat dissipation, up to values in the order of 10^6 W/m^2 [11], [12], exceeding the capacity of conventional heat sinks.

Figure 2.1 depicts how Richard Chu [13], an IBM fellow, previews the heat fluxes generated by chips through the upcoming years, and how recent technologies perform to manage these fluxes, considering a chip temperature of 85ºC and 25ºC room temperature.

The author had predicted heat fluxes as high as $2{,}5\times10^6$ W/m^2, for which new solutions would be necessary. On the other hand, El-Genk and Bostanci [6] consider forced air convection adequate for cooling needs up to 3x10^3 W/m^2, while liquid cooling or impingent jet cooling are preferred for heat fluxes up to 1 – 1,5x10^5 W/m^2.

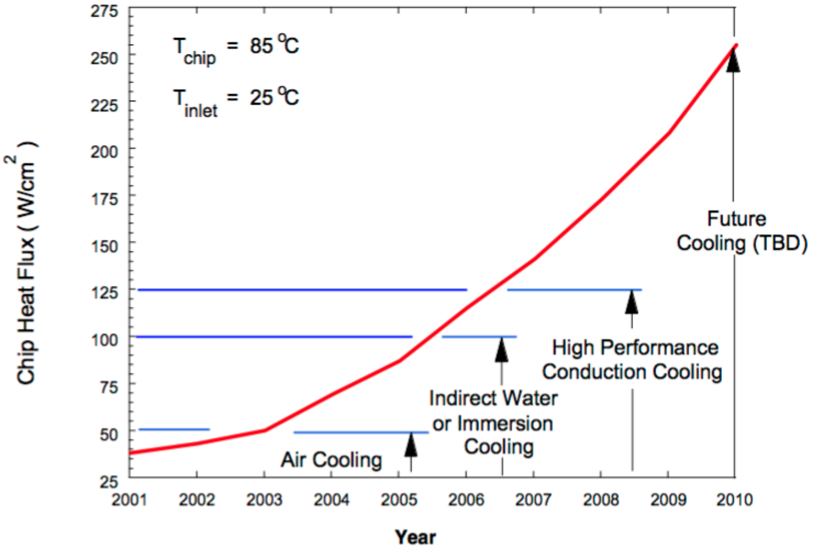

Figure 2.1 - Projected chip heat flux and cooling technology limits, [13].

In an overview, timely predictions and heat flux values might not always match through literature but there is a general consent regarding the need of new solutions for high heat flux dissipation in microprocessor cooling technologies. According to Panão et al. [11], this motivated the appearance of new different approaches for cooling and heat spreading, such as microchannel cooling, impingent liquid jet cooling, liquid spray cooling, immersion cooling, thermosyphons and vapour chambers. All these solutions benefit from the latent heat of vaporisation, which enables the liquid phase to absorb large quantities of heat at a constant saturation temperature, during phase change, which is why these are referred to as two-phase cooling technologies. Some of these two-phase approaches benefit from the nucleate regime of pool boiling heat transfer, which is considered to be promising for high dissipation heat fluxes, as it removes heat within a wide range of fluxes and at relatively small surface temperature superheats [6]. Phase-change solutions also benefit from much larger heat transfer coefficients, compared to those of single-phase liquid cooling or air forced convection cooling, with values within the range 2 - 200 x10^3 W/m^{2}K, as depicted in Figure 2.2, for water as the phase changing substance.

Lasance and Simons [14] compare other cooling methods as natural and forced air convection, the industry standard cooling method, liquid helium cooling, known for having enabled the computer clock speed world record at 8.429GHz [15], forced convection and impingent jet of fluorocarbons and finally water boiling and condensation.

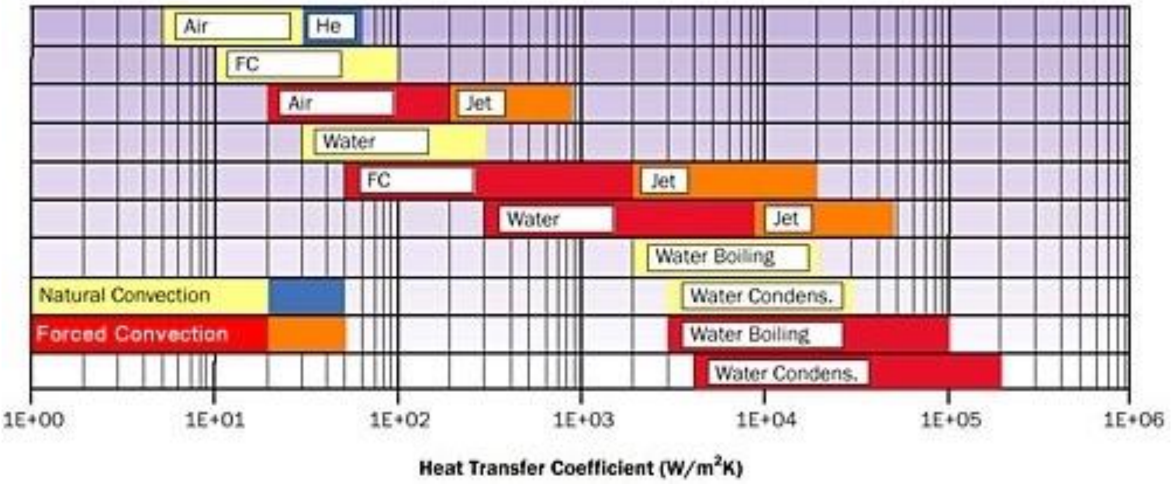

Figure 2.2 - Order of magnitude for heat transfer coefficients as function of cooling technology, [14].

In fact, previously mentioned phase changing technologies as micro-channels, spray cooling or jet impingement face implementation issues for broad usage and commercialization within the scope of CPU cooling. Micro-channels face pumping control challenges and design complexity issues for heat exchange area augmentation, which is lowering its cost effectiveness. Spray and jet cooling have pumping control issues as well, besides unsuitable size, weight and power requirements for market implementation and for inclusion within a computer architecture design. On the other hand, pool boiling is a solution with potential for CPU cooling as it requires no pumping power and has no moving parts, making it easy to implement [16], [17]. The thermosyphon is a practical setup recurring to pool boiling for CPU cooling, with the addition of a condenser component to close the fluid cycle, turning it into an affordable and sustainable solution. Thermosyphons are thus further explored in the next section.

2.2. Two-phase thermosyphon development

A two-phase thermosyphon normally consists in an evaporator and a condenser, connected through supply pipes, thus establishing a closed loop. Heat is transferred from a hot source through an interface surface into the evaporator, where a working fluid removes heat through convective heat transfer. When boiling occurs at the solid-liquid interface, vapour is generated. The released heat is then dissipated from the condenser to the enclosing environment, with the condenser working as a heat sink, and the condensed saturated liquid is returned to the evaporator. The density difference between the downward saturated liquid and the upward saturated vapour creates a pressure head, which drives the flow through the loop, thus no pumping force being required.

Contrarily to heat pipes, thermosyphons allow to decouple the condensation and the evaporation system. This makes thermosyphons suitable to be used in the dissipation of higher heat rates, while providing an additional advantage in terms of design for solutions in often quite complex environments, as is the case of CPU cooling with elaborate desktop computer architectures and still being able to fit them into the computer case.

Looking at the available literature on the topic of thermosyphons development and its use for cooling purposes, the effect of the various operational parameters within these systems was studied by several authors. For instance, in 1992, Vincent and Kok [18] found out that parameters such as the density ratio from vapour to liquid, the dimensionless friction coefficient and the water column height influence overall dynamic behaviour characteristics, such as response time, damping and oscillation frequency, for a co-current thermosyphon setup with water as a working fluid, using a control volume approach.

Pal et al. [19], who performed a quite similar experimental study to the real conditions test presented within this work, were the first known authors to apply a thermosyphon in the cooling of microprocessors in desktop computers. The authors used water and PF5060 as working fluids and experimentally studied the effects of inclination of the thermosyphon, concluding that the evaporator bottom temperature didn't significantly vary until above positive angles of 36° when dry-out occurred and temperature drastically increased. Instead they found the working fluid to deeply impact the performance, with water outperforming PF5060 with average thermal resistances of 0,4°C/W and 0,95°C/W respectively. The higher thermal conductivity and specific heat of water and the improper degassing of PF5060 contribute to this result. They also addressed the transient thermal behaviour of the evaporator with changing processor power output, obtaining periodic temperature oscillations and noticing a phase shift in the observed temperature oscillations before and after the condenser, with the fan playing an important role to regulate the evaporator bottom temperature. This transient behaviour of thermosyphons was also investigated by Farsi et al. [20], who have observed two kinds of system responses, one with regular monotonous thermal progressions and a second with sudden temperature excursions (sudden decreases of temperature) associated with the onset of boiling nucleation. Observations fairly match what is observed later during this work. The authors also developed a mathematical model to obtain an analytical expression of the system time response, depending on geometry and heat transfer parameters. It is a simple and efficient tool for designing two-phase closed loop thermosyphons both in steady and transient regimes. Zhang et al. [21] have also developed a mathematical model of a two-phase thermosyphon with a flat disk shape and manufactured it to compare experimental and numerical results, having arrived at some fair degree of comparability.

Inoue and Monde [22] investigated the operating limit of heat transport in a two-phase thermosyphon with a single connecting adiabatic pipe, water as working fluid and atmospheric pressure, having observed heated surface temperature fluctuations due to an unstable vapour-liquid counter current flow inside the pipe, comparable to observations in this work's later section 6.2.2 regarding the reflux condenser setup. They attached a bell mouth to the entrance of the pipe and observed an enhancement of the operating limit, with the bell mouth controlling the vapour flow into the pipe. They also found the heat flux at the onset of the temperature fluctuations increases with an increase in the pipe inner diameter and can be fairly predicted by an equation derived from the flooding velocity expression presented by Wallis [23].

More recently, Tsai et al. [24] have developed and studied a two-phase closed thermosyphon vapour-chamber system for electronics cooling and Samba et al. [25] applied the same technology to cool outdoor telecommunications equipment. Both results point towards a cooling performance improvement when compared to conventional forced air convection.

Chehade et al. [26] and Franco and Filippeschi [27] have performed experimental analysis of two-phase closed loop thermosyphons. The first used water as a working fluid and evaluated the thermosyphon performance dependence on parameters like the fill charge ratio, the condenser coolant inlet temperature (the condenser was a liquid to liquid heat exchanger instead of the usual forced air convection radiator) and the mass flow rate. The second authors studied compact thermosyphons using water and FC-72 as working fluids. For the device using water, the performance is only influenced by the heat-transfer regime in the evaporator while for the other type, using FC-72, performance is also strongly influenced by the fluid-dynamic characteristics of the whole loop and the mass flow rate.

Many of previously presented references have investigated the influence of different physical and geometrical parameters on often very specific and hardly application-oriented thermosyphon prototypes. Some have also taken some degree of scenario simplification to develop numerical models of thermosyphons, looking at very specific performance matters. The current work on the other hand focuses on a thermosyphon overall efficiency optimization approach allied to a strong application-oriented product development component. The devised solution proposes a step back onto the integrative coupling of the evaporator and condenser components, offering a yet compact design and proposing a freer, unconstrained liquid-vapour flow to maximize performance. In that manner, it could perhaps be classified as a hybrid solution between the conventional thermosyphons and heat pipes, synthetizing the advantages of both into a single product.

2.3. Pool boiling heat transfer enhancement using modified surfaces

The modification of heat transfer surfaces with the purpose of improving nucleate pool boiling parameters such as the heat transfer coefficient h and the critical heat flux CHF has long been studied in literature.

According to Vlachou et al. [28], there are many different types of techniques for pool boiling heat transfer enhancement, including diverse surface modifications methods, such as: surface roughness alteration, artificial cavities etching, pin-fins attachment and changing the wettability characteristics of the surface. The purpose of such methods is to improve the heat transfer characteristics, allowing for higher heat fluxes at lower wall superheats. That is accomplished in two possible ways: improving nucleation by increasing the number of active nucleation sites for a given wall superheat, ΔT, or by increasing the surface exchange area, with comparison to the smooth (unmodified) surface.

The present work will mainly focus on surfaces with cavities, also addressed as micro-structured surfaces in the literature. These micro-structures actively promote the occurrence of nucleation sites, since, despite the well wetting nature of the working fluid used in the present work, it will still allow the formation of nuclei by gas/vapour entrapment in the cavities. Once critical size and energy (wall superheat) required to grow a stable nucleus are achieved, as revised in detail for instance in [29]–[31], a bubble grows, until detachment, determined by the balance of the forces acting on it, and breaking the thermal boundary layer, which is regenerated afterwards, during the rewetting of the liquid. This mechanism is known to be responsible for high heat flux removal from the surface [32]. The mechanism of heterogeneous nucleation and bubble formation summarized above, which is described in detail for instance in [29], [30], [33], occurs generally in the crevices and cavities of any rough surface. Hence, pool boiling heat transfer enhancement by modifying the surface roughness was one of the most popular and pioneering techniques to be tested. Max Jakob [34] was in 1937 among the first to witness the boiling curve changes due to surface roughness alteration. More recently, Poniewski and Thome [33] and Kim et al. [31] have provided an extensive overview of the theoretical background on the topic. Jones et al. [35] have also studied the influence of surface roughness on nucleate pool boiling heat transfer. The authors have used both water and FC-77 to test boiling surfaces and observed the heat transfer coefficients h were more strongly influenced by surface roughness with FC-77 than with water. For FC-77, the roughest surface resulted in 210% higher h than the polished surface while for water, a 100% enhancement was measured between the same two surfaces. A correlation between the heat transfer coefficient h and the roughness parameter R_a was observed, confirming previous studies' results. However, such relation was strongly empirical and could not be used to deepen the understanding on the boiling mechanisms which would allow to produce systematically surfaces promoting boiling with high and known heat transfer coefficients. In fact, as experimentally proved by McHale and Garimella [36], no correlation could be observed between the characteristic parameters characterizing bubble dynamics (e.g. bubble departure diameter) and the surface mean roughness, as this or any similar average parameters could not include the specific geometric characteristics of the surface topography (e.g. shape and depth of the cavities and distance between them). As the bubble departure mechanisms affect the heat transfer, a more systematic approach was sustained by some other authors, who addressed surfaces structured with a regular pattern of cavities and or pillars [36]–[38]. Several other authors, [39], [40] have reviewed the topic of pool boiling heat transfer with micro and nano-structured surfaces, with overall observations that agree on topics such as the microstructures ability to enhance the activation and density of bubble nuclei, reducing the wall superheat and enhancing heat flux. The authors observed nano-structures can accelerate bubble departure by decreasing the bubble departure diameter and increasing the departure frequency. They also observed an earlier onset of nucleate boiling, besides a heat transfer coefficient and critical heat flux increase due to the structuration. The tested surfaces manufacturing processes include machining, coating or chemical and electrochemical processes. Moita et al. [41] studied the influence of surface topography in the boiling mechanisms. The covered topographic setups ranged from micro-cavities to micro-pillars with results showing a significant increase of h of about 10 times for water and 8 times for a dielectric fluid, HFE-7100, when comparing a smooth surface to micro-pillars patterning. Gess et al. [42] have studied two types of surfaces as heat sinks for a high power consumption, low form factor server cooled in liquid immersion. The first was microporous sintered copper and the former contained a dense array of microscale fins. The working liquid was 3M™ Novec 649 and a dielectric pump was used with 300% h improvements obtained with temperature reductions of roughly 18°C at the highest tested heat fluxes. Micro-fined surfaces revealed to be more beneficial when dielectric fluids are used at high flow rates and microporous showed better results at low flow rates or when the pump is not used.

Most of the aforementioned studies refer to an inter-cavity distance parameter S, later used throughout this work. Following the pioneering work, for instance of Chekanov [43], who related this distance with the interaction mechanisms between nucleation sites, these authors, e.g. Moita et al. [41] observe the declining of the heat transfer coefficient for critical values of S below which the interaction mechanisms and the coalescence would overcome the benefits of increasing the number of nucleation sites (lower S leads to a larger number of cavities in the same surface area), as they would promote the generation of large vapour bubbles that would insulate the surface and endorse the conditions to anticipate the occurrence of the Critical heat flux. In this context, Teodori et al. [3] used Particle image velocimetry (PIV) techniques to observe the near-wall boiling flow and mechanisms over micro-patterned surfaces. They tested surfaces with different inter-cavity distances ranging from 200 to 2000 µm, having concluded the positive effect of smaller distances causing more nucleation sites and improving latent heat transport must be balanced with the negative effect of coalescence between consecutive bubble nuclei, to avoid the emergence of a large vapour film which could isolate the hot surface and induce transition to a film boiling regime.

Framed within this work's product optimization objective, there is an underlying parametrical study of the influence of cavity distance, S, on performance indicators such as the heat transfer coefficient h, the Critical heat flux, CHF or the onset of nucleate pool boiling, as part of the product optimization process. The proposed outcome is to obtain the best performing micro-structured surface to fit the final prototype, or to suggest future related work, if evidence leads to the need for more results and differently disposed micro-structured arrays of cavities, with different S parameters or patterns. The surfaces to test feature inter-cavity distances ranging from 100 to 600 µm.

2.4. Pool boiling on vertical oriented surfaces

Where for the previous case of horizontal hot surfaces in pool boiling regimes, natural convection caused the heated liquid and later bubbles to flow upwards, away from the surface, in the case of vertical surfaces, this movement will be parallel to the surface, with a given flowing control mass of liquid or bubble continuously absorbing heat through the movement. That causes an irregular boiling regime distribution all across the surface, depending on height, with cooler liquid in the bottom, followed by beginning of boiling, and increasingly bigger bubbles as we go upwards. If the surfaces were "tall" enough, at a certain height, boiling crisis would occur where eventually all the rising bubbles would coalesce and that would mark the transition to film boiling, with an abrupt increase in wall superheat. Film boiling (as identified in chapter 3) in vertical surfaces has been a subject of research due to a wide array of applications. For instance, Das et al. [44] have developed a model for film boiling heat transfer scale analysis in a vast range of vertical flat plate configurations and Ishigai et al. [45] reported a CHF decrease with increasing heating surface area. Although scarce information is available about nucleate pool boiling on vertical surfaces, some studies have been reported. Howard and Mudawar [46] identified three different CHF triggering mechanisms associated with different ranges of surface inclination, upward-facing, near-vertical and downward-facing, focusing on the near-vertical (60°-165°) case. They developed a comprehensive model to predict CHF, which shows good agreement with experimental data. So far, from mentioned literature, one could infer vertical orientation causes a CHF reduction, although more studies should be performed to verify this statement, since many dimensional and contextual factors are to be taken into account. Hall et al. [7] have developed a numerical model which makes possible to predict wall temperature distributions in vertical, uniformly and symmetrically heated rectangular channels. Nishikawa et al. [47] have used water at ambient pressure to study pool boiling over a heated copper flat plate at different inclination angles. In the low heat flux region, the authors observed how the heat transfer coefficient increases remarkably as the inclination angle is increased, while there is no marked effect in the high heat flux region. Ferjančič and Golobič [48] have studied the effects of roughness on pool boiling CHF both for horizontal and vertical surfaces. They have used steel plates manufactured through sanding and chemical etching processes and water and FC-72 as test fluids and observed a 51% water CHF improvement in the etched surface when compared to the sanded one.

A relevant work by Jiao et al. [49] was reviewed, with many common grounds with the current work. The authors developed a comprehensive model for the investigation of the effect of filling ratio on the steady-state heat transfer performance of a vertical two-phase closed thermosyphon, with three types of flow pattern and two types of transition regimes, according to the distribution of film and nucleate regime regions. This model also takes into account the effects of heat input, operating pressure and thermosyphon geometry. The model was validated with experimental data with nitrogen as working fluid, allowing the authors to obtain a range of filling rates to keep the thermosyphon steady and effectively functioning.

As previously mentioned, this work is characterized by a strong orientation to application purpose product development, namely in the context of vertical optimized compact thermosyphons mounted in vertically oriented motherboards, to cool CPUs in desktop computers, most often nowadays used in their upright vertical position. This goal overshadows the fact that few resources are available to frame the current aspect of this work, offering an opportunity to launch new discussions and present new results regarding the overall pool boiling performance of thermosyphons in vertical orientation, both subject of interest to the scientific community and the likes of industries such as cooling for gaming computers, servers or data centres. In fact, the current work paves the way for the parametric research of how the cavity micro-structures under study influence the h and CHF of the thermosyphon system, for a vertical configuration.

3. Theoretical background

The present chapter will introduce some basic concepts in pool boiling heat transfer, in which the present work was based. Awareness of such concepts is of crucial importance to understand the physical mechanisms underlying the development of cooling systems such as the present work's two-phase closed loop thermosyphon.

3.1. Basic concepts in pool boiling heat transfer

Among most relevant basic heat transfer concepts targeted throughout within this work's scope are the heat transfer coefficient, a transversal parameter to infer on any type of heat transfer mode, being this conduction, radiation or convection, being the latest the most present mode within a thermosyphon, hence the most important for this work. Since thermosyphons recur to pool boiling heat transfer, the fundamental concept of boiling curve is also introduced, as well as a specific analysis of the nucleate pool boiling heat transfer regime, finalizing this section with an overview of the critical heat flux to which transition from the nucleate to film pool boiling regime occurs, a very important parameter to consider when designing the devised cooling system.

3.1.1. Heat transfer coefficient

The heat transfer coefficient is denoted by letter h and may be defined as the heat flowing in unit time through a unit area of a medium or system with 1K temperature difference between its boundaries [50]. It is a measure of the ability of a given heat transfer mode of given substances and materials and specific dynamic characteristics to transport heat in space, being also defined as the thermal admittance, film coefficient or film effectiveness. It is the proportionality constant between the heat flux, q'' and the thermodynamic driving force for the flow of heat, the temperature difference, ΔT:

$$h = \frac{q''}{\Delta T} \tag{3.1}$$

Its units are h [$\mathrm{W\cdot K^{-1}\cdot m^{-2}}$], that is the heat transfer rate per unit kelvin per unit area. It is a recurring parameter through this work, used to characterize the copper surfaces ability to dissipate the heat absorbed from the processor heat source into the boiling liquid. It is typically used in calculating the heat transfer by convection or phase transition between a fluid and a solid, as the current work's case. The heat transfer coefficient is often calculated through the dimensionless Nusselt number, Nu, which is defined as the ratio of convective to conductive heat transfer across the normal to a liquid-solid boundary:

$$\mathrm{Nu} = \frac{hL}{k} \tag{3.2}$$

Where L is a characteristic length of the specific geometry and k is the thermal conductivity of the fluid. Different correlations were adopted to obtain the Nusselt number depending on flow characteristics (e.g. Reynolds number), geometry and employed materials.

Later during this work, the heat transfer coefficient is obtained directly applying equation 3.1 knowing the predetermined applied heat flux to the thermosyphon and the measured wall superheat as the temperature difference ΔT.

3.1.2. Boiling curve

Pool boiling is a special type of convective heat transfer mode, where the fluid will start from a quiescent state inside a pool (i.e. an open or fully closed container enclosing the liquid), and as soon as a hot surface superheat (temperature difference above the saturation temperature of the liquid, T_{sat}) is present, natural convection will start and the fluid will circulate inside the pool, eventually leading to the emergence and growth of nucleation sites in the hot surface. As wall superheat increases, the flow will then develop into a fully developed nucleate boiling regime, until a certain heat flux is achieved for which a vapour blanket will start to form above the surface, causing a heat transfer coefficient major reduction and a wall superheat steep increase. This point is called the Critical heat flux, being often a critical design point for most applications. Pool boiling under different experimental conditions has been studied since the early 20th century, being the most relevant work the study carried through by Shiro Nukiyama in 1934 [51], where he first draw the curve relating the wall superheat in an open pool boiling water experiment at atmospheric pressure with the respective heat flux.

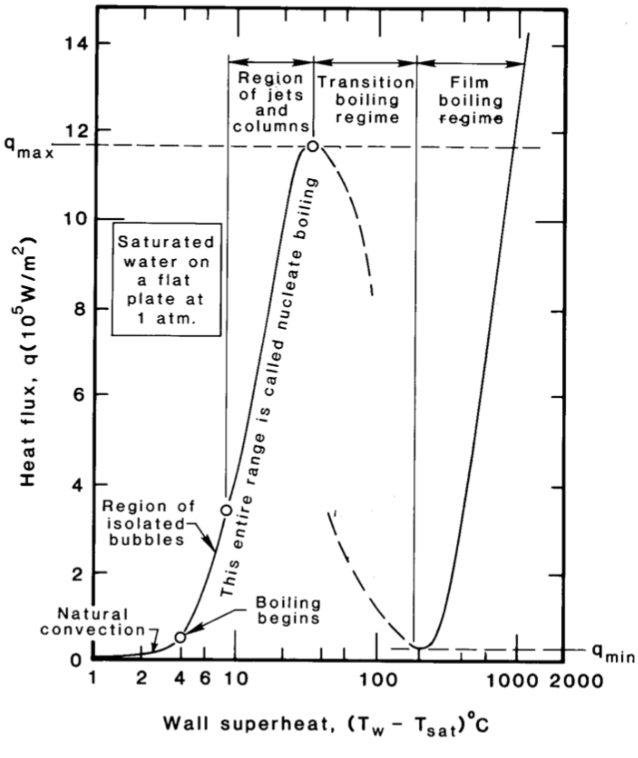

Figure 3.1 - Boiling curve of saturated water on a flat plate at 1 atm, [52].

This curve became known as the boiling curve, present throughout all further boiling studies up to nowadays, including this work. Figure 3.1 is a quite explanatory adaptation from Nukiyama's original curve, where Critical heat flux is represented as q_{max} [52]. A boiling curve is typically built considering the heat flux as the independent variable, with the steep temperature transition to film boiling regime when critical heat flux is achieved (dashed line in figure 3.1). Nevertheless, measurements obtained when the heat flux is decreased from film boiling regime show temperature to continuously decrease with no steep jump at the Critical heat flux value, thus creating a hysteresis behaviour. Nukiyama conjectured there would be a continuous transition in heat flux when performing experiments with temperature as the independent variable, thus connecting the broken dashed lines in previous figure. In 1937, Drew and Mueller [53] successfully accomplished to do so by boiling organic liquids outside a tube, allowing steam to condense inside the tube at an elevated pressure. The steam's saturation temperature, hence the tube-wall temperature—was varied by controlling the steam's pressure. This permitted them to obtain a few scattered data although measurements of this kind are inherently hard to make accurately. For the next forty years, the relatively few nucleate boiling data obtained by researchers were usually interpreted as verifying Nukiyama's suggestion that this part of the boiling curve is continuous. The q_{min} point in figure 3.1 is the minimum heat flux to which a layer of vapour separates the liquid and the surface and is called Leidenfrost point, after the 18th century scientist Johann Gottlob Leidenfrost. With decreasing heat flux, it is the point when surface wetting occurs.

There are five identified boiling regimes as seen in figure 3.1: Natural convection; Nucleate boiling, composed of two regions, the first being isolated bubbles and the second the region of slugs and columns when bubbles coalesce; Boiling crisis, peak heat flux or critical heat flux; Transition boiling regime when occasional wetting still occurs; Film boiling, when a full vapour layers is created. The regime to which heat transfer is the greatest is the fully developed, slugs and columns nucleate boiling regime, being the main interest of the current work, thus being addressed in the next section.

3.1.3. Nucleate pool boiling regime

As previously introduced, heterogeneous nucleate pool boiling occurs when bubbles of any evaporated substance are generated on a heated surface. A real surface will have a microscopic height profile of the following kind, more or less irregular depending on its roughness:

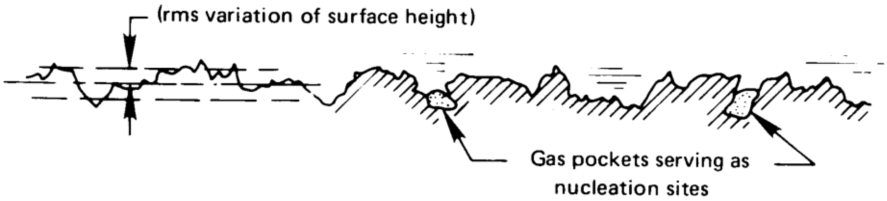

Figure 3.2 - Typical surface roughness profile.

When the surface is wetted, surface tension prevents liquid from entering these holes, so small gas or vapour pockets are formed. These little pockets are the sites at which bubble nucleation occurs. To understand why these pockets serve as nucleation sites, a spherical bubble of a pure saturated gas at equilibrium with an infinite superheated corresponding liquid is idealized. To determine the size of such a bubble, conditions of mechanical and thermal equilibrium are imposed. The bubble will be in mechanical equilibrium when the pressure difference between the inside and the outside of the bubble is balanced by the forces of surface tension, σ, as indicated in figure 3.3:

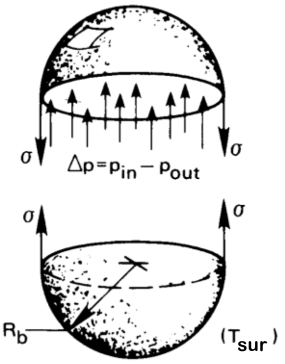

Figure 3.3 - Spherical bubble of a pure saturated gas at mechanical and thermal equilibrium.

Since thermal equilibrium requires that the temperature must be the same inside and outside the bubble, and since the vapour inside must be saturated at T_{sur} because it is in contact with its liquid, the force balance takes the form

$$(p_{in} - p_{out})\pi {R_b}^2 = (2\pi R_b)\sigma \Leftrightarrow R_b = \frac{2\sigma}{p_{sat}(T_{sur}) - p_{amb}} \tag{3.3}$$

The equilibrium bubble, whose radius is described by equation 3.3, is unstable. If its radius is less than this value, surface tension will overbalance $p_{sat}(T_{sur}) - p_{amb}$. When that happens, vapor inside will condense at this higher pressure and the bubble will collapse. If the bubble radius is slightly larger than the equation specifies, liquid at the interface will evaporate and the bubble will begin to grow. Thus, as the heater surface temperature is increased, higher and higher values of $p_{sat}(T_{sur}) - p_{amb}$ will result and the equilibrium radius, R_b, will decrease in accordance with equation 3.3. It follows that smaller and smaller vapor pockets will be triggered into active bubble growth as the temperature is increased. A more accurate estimate can be made using the subsequent work by Rohsenow [54], who proposed a semi-empirical correlation to predict the relation between heat flux and wall superheat on nucleate boiling heat transfer. The author assumed heat flux q''_{NB} to be dependent on some function of the fluid properties and surface characteristics, multiplied by a temperature difference between the wall temperature and saturation temperature at a given liquid pressure, to the power of a parameter a, $\Delta T = [T_w - T_{sat}(P_l)]^a$. Through his experimental results, the famous empirical relation was obtained:

$$q''_{NB} = \mu_l h_{fg} \left[\frac{g(\rho_l - \rho_v)}{\sigma}\right]^{1/2} \left[\frac{c_{pl}\Delta T_{sat}}{C_{sf} h_{fg} {Pr_l}^{m+1}}\right]^{1/n} \tag{3.4}$$

where c_{pl} is the specific heat of the liquid, σ is the surface tension, h_{fg} is the latent heat of vaporization, μ_l is the viscosity of liquid working fluid, g the gravity, $\Delta T_{sat} = T_w - T_{sat}(P_l)$ is the surface superheat and q''_{NB} is the heat flux across the heating surface. Pr is the Prandtl number $Pr = c_p\mu/k$. Values of C_{sf},

m and n, are empirical fitting constants that take into account the properties of the surface and fluid, such as the wettability associated to the contact angle and the micro-roughness, and their effect in the nucleation site intensity. At a certain point throughout the nucleate regime, a crisis occurs known as Critical heat flux, substantially important for the current work and will be explored next.

3.1.4. Critical heat flux

The Critical heat flux, sometimes addressed as Boiling crisis or Peak heat flux, is the heat flux value for which vapour blankets start to form from merging bubbles of relative big dimensions, causing the until then main heat transfer mechanism of convection to fail, with radiation and conduction through gas prevailing. Heat transfer coefficients associated with these mechanisms are lower, so heat is less efficiently removed and surface superheat shoots up. Many authors propose correlations for CHF, with major approach differences pertaining surface characteristics such as chemistry or topography, which alter wettability. For instance, Kutateladze [55] and Zuber [56] studied the CHF phenomena within the scope of hydrodynamics theory. According to the authors, CHF occurs when the surface-fluid interface is disrupted as the result of the velocity difference between the ascending vapour column and the liquid descending due to gravity. The CHF expression can be approximated as

$$q''_{max} = C h_{fg} \rho_v \left[\frac{\sigma g (\rho_l - \rho_v)}{\rho_v^2} \right]^{1/4} \tag{3.5}$$

where C is a correction factor accounting for different heater geometries. $C = \pi/24$ is the recommended factor by Zuber for a variety finite geometries and C = 0,149 is recommended for large plates. Lienhard and Dhir [57] and Lienhard and Hasan [58] provide an extensive summary of the CHF for various geometric configurations. Hydrodynamic theories weren't able to successfully predict CHF in more recent studies, being one main reason that surface characteristics as wettability are not taken into account. This influence of surface characteristics has been studied by Kim et al. [59], who have shown their effectiveness in influencing CHF.

CHF Enhancement

An important concept to introduce is the Critical Heat Flux Enhancement parameter. Vlachou et al. [28] define it as the increase in CHF of a surface which has been modified by any of the presented enhancement methods, compared to the CHF of a smooth surface as a percentage, as follows:

$$CHF\ enhancement = \frac{CHF_{modified} - CHF_{smooth}}{CHF_{smooth}} .100\ [\%] \tag{3.6}$$

It is of major importance to maximize this parameter through surface modification techniques as it sets new boundaries for the usage of the devised cooling systems.

3.1.5. Thermal resistance

Analogous to an electrical resistance in circuits, a thermal resistance may be defined as a measure of how much a body or material can resist to heat flow. As a resistance, it is a ratio of a driving potential and a corresponding transfer rate, being in this thermal context a temperature difference and a heat transfer rate, respectively [60]. Thermosyphons just as the one developed in the present work and other heat sinks as such are often characterized according to their absolute thermal resistance, R, which is a measurement of that component's resistance to heat flow. Equation 3.7 applies the mentioned reasoning to define the thermosyphon absolute thermal resistance, R:

$$R = \frac{T_j - T_{amb}}{\mathrm{q}} \ [\mathrm{K/W}] \tag{3.7}$$

being $T_j - T_{amb}$ the driving potential temperature difference from surface junction to ambient, and q the heat transfer rate.

4. Design and optimization of the thermosyphon system

The present chapter covers the design and development efforts carried through with the objective to obtain the final layout of the proposed cooling system. With the ultimate purpose of developing a compact and functional commercial product for CPU cooling, the final design does not yet correspond to the objective, being part of a longer-term project, within which this master thesis' scope is framed. Nevertheless, important steps were taken, and the devised final prototype is now closer to the intended aim of obtaining a final product. This prototype and its design and optimization phases are introduced in the fourth section of the present chapter, being the third section an overview of the initial experimental facility's design process. The design efforts of the later prototype were strongly based on experimental outcomes and experience obtained during design phases of the former facility, hence the structuration of the present chapter. Figure 4.1 schematically represents this evolution process. An initial section covers the process for choosing the cooling liquid to use in the thermosyphon system, followed by an introduction on the use of a transistor to simulate the CPU die thermal behaviour simulator.

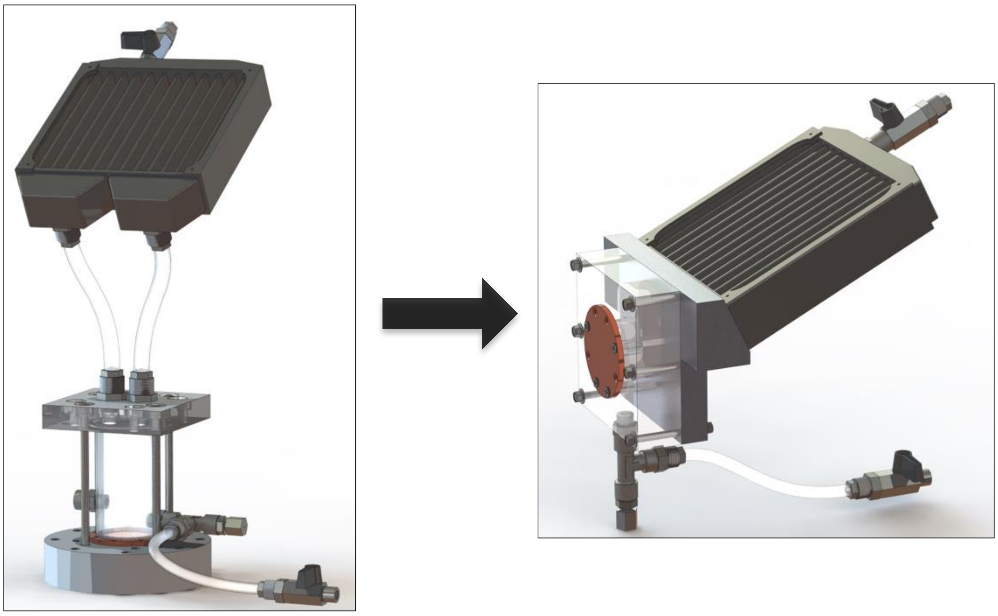

Figure 4.1 - Product development process.

4.1. Cooling liquid

The options regarding the choice of liquid to use in such a pool boiling thermosyphon system are based in an important criterion: whether to design the system for direct liquid cooling or using a solid interface on the chip or its packaging. Both have associated benefits, which are briefly introduced in the following paragraphs. In the case of solid interface, it allows for the use of water, which has a large latent heat of vaporization, meaning larger nucleate boiling and critical heat fluxes. It is also less complex and easier to manufacture and implement than a direct immersion solution as it enables the development of a closed package product instead of some device to be fully integrated within the computer production process. Direct liquid cooling on the other hand enables one thermal resistance layer to be removed, increasing heat fluxes and the overall efficiency of the system. However, it narrows the choice down to dielectric fluids, which have non-conductive electric properties to allow them to be in contact with the processor's hardware. Fortunately, these fluids, such as perfluorocarbons (FC-40, FC-72) and hydrofluoroethers (HFE-7000, HFE-7100, HFE-7200), widely used in literature for electronics cooling applications, [6], [12], [16], [17], have excellent qualities as low saturation temperatures at common working pressures (0,1 MPa), small temperature variation over the hot surface which accounts for the neutralization of hot-spots, and chemical properties compatible with the surface and other components. Additionally, HFE fluids are environmentally friendly, with zero Ozone depletion potential, which is not the case of FC fluids.

Table 1 - Thermophysical Properties of Dielectric Liquids and Water at 1 atm and 25°C [16], [17].

Property	FC-40	FC-72	HFE-7000	HFE-7100	HFE-7200	Water
T_{sat} (ºC)	156	56	34	61	76	100
ρ_f (kg/m^3)	1870	1623	1386.2	1500	1430	957.8
ρ_v (kg/m^3)	25	12.7	8.22	9.6	9.26	0.5956
μ_f (N.m/s^2) x10^3	3.54	0.457	0.431	0.61	0.61	0.279
C_{pf} (J/kg.K)	-	1097.8	1327.93	1180	1210	4217
k_f (W/m.K)	-	0.052	0.075	-	-	0.68
h_{fg} (kJ/kg)	711.6	84.97	132.16	125.6	122.6	2257
σ_f (mN/m)	16	8.4	12.4	14	14	58.9

However, their relatively low latent heats of vaporization (see table 1 for complete properties) comparing to water, reduce their pool boiling cooling potential. To overcome this, enhancement of the pool boiling mechanisms must be addressed, usually by enhancing the heat exchange surface. This is accomplished by multiple techniques, such as surface roughness alteration, artificial cavities etching, pin-fins attachment and changing the wettability characteristics of the surface. This work considers the utilization of HFE-7000, a dielectric liquid manufactured by the 3M® corporation, as a working fluid throughout all its stages, since one of the project purposes is to develop the final product for direct liquid cooling.

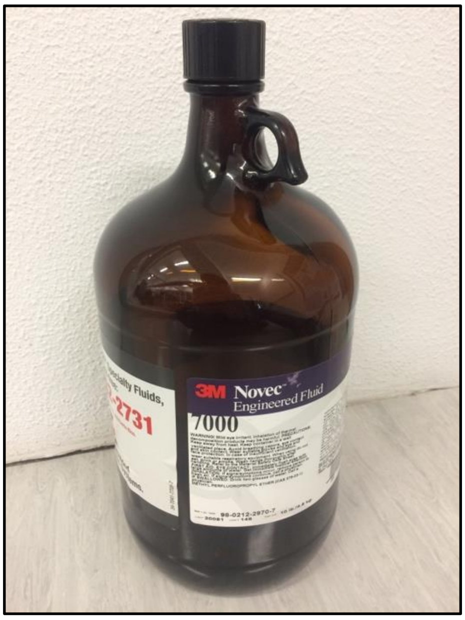

Figure 4.2 - 3M Novec HFE-7000 container.

Material compatibility

The option for 3M® HFE-7000 as a cooling liquid introduces some material compatibility constrains, for the many components in direct contact with the fluid. Following the previous research on the topic, carried on by Moura on his framework thesis [2], it was concluded that compatibility issues are plasticizers and additives added in the production of elastomers. Being polymeric materials the most affordable and suitable construction material for the facility's components, hydrofluoroethers are known to easily dissolve hydrocarbon plasticizers, which can cause the polymer to harden, crack or shrink. Moura performed extensive compatibility tests for when he chose the materials for sealing components, submerging the materials into a HFE-7000 bath for one week, with results showing that Viton™ O-rings, Araldite® epoxy and a Teflon™ anaerobic adhesive could effectively resist to the liquid, having been these materials used for all sealing in the two developed facilities. Structural components were made of metallic materials as copper and aluminium, and acrylic transparent polymer. below, Table 2 shows a compilation chart of all 3M's HFE fluids compatibility with polymeric materials.

Table 2 – Polymeric materials compatibility chart with 3M® HFE fluids, [2].

Compatible		Non-compatible	
Polyethylene	Rulon™	Nitrile	Polysulfide
Polypropylene	PTFE(Teflon™)	Silicone	Polyacrylate
ABS	Polysulfone	Butyl	Polyurethane
Nylon	PEEK	Fluorocarbon	Styrene
PVC	Thermoplastics	Fluorosilicone	Butadiene
Polycarbonate	Acrylic(Plexiglas™)	Natural Rubber	Ethylene
		Chloroprene	EP or EPDM

4.2. Transistor thermal simulation of a CPU die

Addressing the urging necessity for the cooling system to be experimentally tested under boundary conditions representative of the real working conditions, some system had to be developed to accurately simulate the quite complex mechanism of heat dissipation in a CPU package. Following previous approaches in the same research group [2], [61], a transistor component with macroscopic dimensions was used with this purpose. It is used as the heat source for all experiments in this work, both for the horizontal and vertical experimental facilities and in both steady-state and transient tests, being later replaced by the actual CPU in the tested desktop computer, in the final real working conditions tests. The adopted transistor is a IRFP450 N-channel power MOSFET with a TO-247 package. Figure 4.3 shows a schematic representation of the transistor and its electrical diagram.

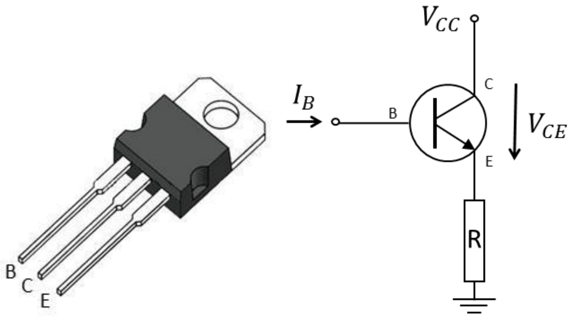

Figure 4.3 - N-channel TO-247 MOSFET.

This transistor has a maximum dissipated power of 190 W and its heat spreading surface has a contact area of 172 mm^2. The allowed maximum surface temperature is 150°C. Being this value considerably higher than in any CPU, it allows for the system to operate safely, during CPU simulated conditions. For the proposed full characterization of the testes surfaces and their CHF values, caution was undertaken not to achieve limit temperatures, before occurrence of CHF. As will be seen in chapter 6, maximum junction temperatures at imminence of CHF didn't surpass 120°C, preserving the transistor. This transistor has three terminals, namely base (B), collector (C) and emitter (E), as seen in figure 4.3. Dissipated power follows Joule's law and is equal to the product of the Collector-Emitter current and the voltage drop across these terminals, as stated in equation 4.1:

$$P = V_{CE}.I_{CE}\ [W] \tag{4.1}$$

The current applied to the Base terminal changes the internal resistance between the Collector and Emitter. The gain β of a transistor is quantified as the ratio between the current flow through the Collector-Emitter and the drive current applied to the Base. Controlling this drive current and knowing the gain of the transistor, one can control the dissipated power. The transistor's resistance is also temperature-dependant, which would change the dissipated power as temperature would rise and make it impossible to control with Base current tuning solely. An operational amplifier is then used to control the power circuit, as will later be described in chapter 5 overview of the electronic control system.

To further simulate the thermal behaviour of a CPU, the transistor (equivalent to the CPU die) would need to be coupled to an Integrated heat spreader, such as those in conventional CPU packages. An IHS was adapted from a 2005 Intel Pentium 4. Figure 4.4 shows the adapted IHS, the processor and its die and the transistors.

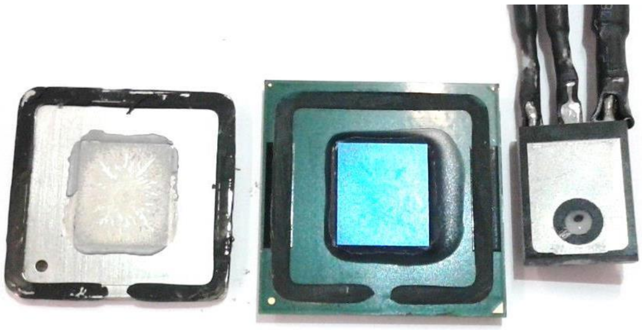

Figure 4.4 - IHS; Processor; Transistor.

With an area of 200 mm^2, the CPU die has very similar dimensions to the transistor, with 172 mm^2 reassuring the later as a good thermal simulator. Previous work by Moura includes a validation study in which the transistor approach was compared to a CPU in its thermal behaviour, analysing pictures obtained with a thermographic camera. Similar results were obtained here, being the current work's option for the transistor as a CPU simulator based on the previous validation. The transistor is a very important component for the design phases, as its size and characteristics define some constraints to the remaining experimental facility. Its size, close to that of a CPU core, allows for the use of an available conventional Intel® IHS, which size was then taken as a reference when designing the copper surfaces. These had to be big enough to fully cover the IHS in its surface area. The manufacturing of these surfaces will later be addressed in section 5.2. As a result, for a 31 x 31 mm IHS, surfaces with 50 mm diameter were designed and manufactured. It is this surface dimension and its available heat transfer area that determine the evaporator's dimensions, as will later be seen.

4.3. Horizontally oriented experimental facility

Taking off from Moura's previous work [2], in which both a "proof of concept" prototype and a final experimental facility were developed, a similar design approach was followed for the initial horizontal experimental facility. This facility was aimed for a full characterization of the tested heat exchange surfaces, in both their steady-state and transient responses to different heat loads and heat time-dependant profiles, so Moura's experience with similar experiments was a valuable input during this design phase. In fact, some structural components were reused from his "proof of concept" facility. The facility considered in the present work and following the thermosyphon methodology consists of an evaporator, where heat is absorbed from the environment through a hot surface, and a condenser, where this heat is returned to the environment. The working fluid flows inside these elements in a closed loop. It is also a two-phase system, with both liquid and vapour phases constantly present within the loop. An initial prototype was developed with excessive evaporator size, for later tests and size optimization, as will be addressed. The final facility was obtained after the design phases introduced in the next sections, and later used in all horizontal orientation experiments within this work. The implemented final facility is shown below in figure 4.5, featuring the evaporator in its lower region and the condenser on top. Two clear rubber pipes connect the two components. The evaporator is mounted on a Teflon base block (round white block), for insulated heat transfer and for structural purposes. The transistor is mounted under the Teflon block, through an inner central cavity opening way to the copper surface's bottom. The condenser was designed following a reflux flow approach, as suggested by project peers who believed that this approach could improve the efficiency of the cooling system. Later results show this statement is depending on some other factors, although the final outcome confirms the proposed thesis. In fact, following a design point-of-view, the reflux condenser enables an overall more compact product, good for fitting inside the desktop computer to cool.

Figure 4.5 - Final design for prototype with horizontal oriented hot surface (CAD model - SolidWorks).

4.3.1. Evaporator design

For the horizontal facility, a cylindrical design was chosen for the evaporator, since the hot surfaces to test are circular. A clear acrylic tube was used for the main body of the evaporator. The bottom open end of the tube is closed by the hot surface, using a Viton™ O-ring and the Teflon™ adhesive for sealing under pressure. Due to its very small surface tension, HFE-7000 can effectively drain through very tiny leaks, hence the usage of the anaerobic adhesive, which gains consistency under pressure, for extra sealing. The top open end of the cylinder is sealed by another acrylic part, a square block with a groove for an additional O-ring, and two threaded holes for connecting pipe couplings leading to the condenser above. The adhesive is here again used for extra sealing guarantee. The whole evaporator assembly is structurally kept together by four threads with nuts and washers for an adequate tightening. Figure 4.6 shows the resulting CAD model, with the assembly mounted on the Teflon (PTFE) base. Some additional components were added for the inclusion of sensors in the system, namely, the pipe coupling as can be seen in the left wall of the evaporator's cylinder in figure 4.6, which connects a clear rubber pipe with 3 mm inner diameter leading to the used differential pressure sensor. The right side of the evaporator features a T pipe connecting a thermocouple to measure near-wall saturation temperature and a 4 mm pipe leading to a tap used for inserting and removing the working liquid. This and remaining instrumentation and control electronics will later be introduced in chapter 5. A critical decision to be made pertained to the inner diameter of the acrylic tube. It must account for the heat dissipation area of the IHS coupled to the transistor. With an approximate 31x31 mm area (fillet corners with 3 mm radius) a cylinder with 32 mm inner diameter was chosen, which covers most of the IHS. On the other side, the cavity etched region of the structured surfaces has a 30 mm diameter which allows using this inner diameter.

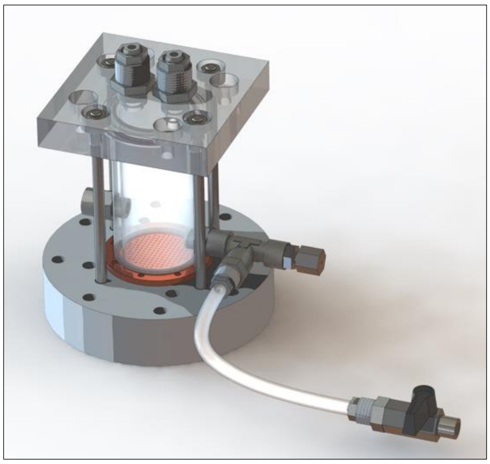

Figure 4.6 - Final evaporator design with horizontal oriented surface (CAD model - SolidWorks).

The outer diameter of the cylinder is 40 mm which allows for a wall thick big enough to resist the considerate compression load applied to properly seal the assembly, with 4 mm thickness. The cylinder dimensions were also limited to available offer from suppliers in the region. The local acrylic products manufacturer Acrilfer was chosen as a supplier for the acrylic components, having the required material availability. Later machining works for the manufacturing of the evaporator with the pretended size, threaded holes and O-ring grooves were performed during this work, in the university department's shop floor.

Optimum liquid fill charge

It's common practice in thermosyphon design to optimize the amount of working liquid to use inside the closed chamber [25], [26], [49]. Thus, a simple experiment is performed to evaluate the absolute thermal resistance of the devised system, function of a varying liquid phase fill, in order to obtain the optimal fill rates. Results obtained are shown in the following figure:

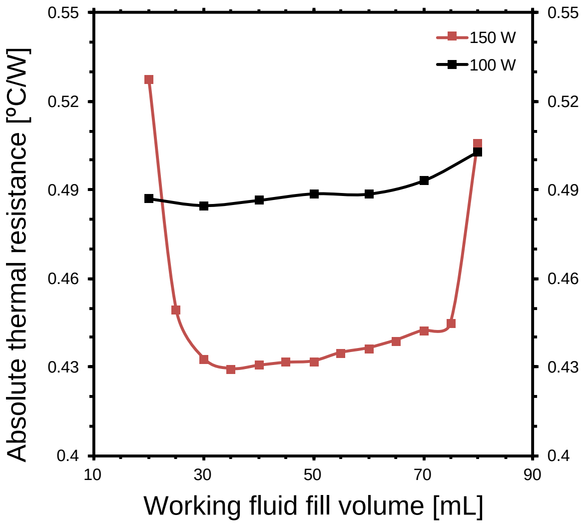

Figure 4.7 - Absolute thermal resistance in function of liquid phase fill.

One can observe in this figure that thermal resistance increases with higher fill volume values (>70 ml) as well as with lower ones (<30 ml). Both situations can be addressed with a theoretical explanation. In fact, high levels of liquid lead to a condenser flooding, reducing its ability to replenish the overall flow with liquid phase, as its useful heat exchange area is occupied by liquid phase. On the other hand, due to the reflux setup, subcooled condensed liquid hardly reaches the surface to be cooled, as it must be mixed into a large height of liquid in the evaporator. Ultimately, it gets mixed with warmer condensed liquid in the higher region of the liquid phase, thus the cooling efficiency of the overall system is reduced, increasing the thermal resistance. Another contribution to this increase is the higher equilibrium pressure caused by a lower volume available for the vapour phase, leading to a higher saturation temperature and a lower heat flux from the heat source to the liquid. In the case of low liquid fill quantities, the opposite occurs, there is a lack of subcooled liquid phase to cool down the hot surface, leading to an increase in its temperature and a subsequent increase in the heat load and flow rate, eventually leading to a dangerous surface dry-out. Finally, the optimization of the amount of liquid used can be important, given the decrease in the liquid level ratio, with increasing heat load. This results are in accordance with previous results obtained by Moura [2].

The resulting optimum liquid fill volume was set as 30 ml, out of a window of possibilities ranging from 30 to 70 ml. The smallest value was chosen in a logic of dimensions' minimization, requiring a smaller evaporator, with the benefit of less vapour friction losses during the flow and a more compact design.

Evaporator size

Following the previously introduced experiment, a straightforward test was performed to evaluate the desired size for the cylindrical evaporator. With the 30 ml working fluid quantity set, different heat loads ranging from 5 W to 200 W were applied in order to observe what was the maximum height reached by the turbulent liquid phase flow inside the evaporator chamber. The oversized evaporator initially had 100 mm height, and after this procedure, this size was cut down to 70 mm, as in figure 4.6 and again the final height for all further experiments with the horizontal facility.

4.3.2. Condenser design

For the condenser component, a commercial product was acquired and adapted to fit the requirements. The opted product was a conventional water cooling radiator, a NexXxoS ST30 Full Copper 120mm by the German OEM Alphacool®. Decision was based on availability and dimensional compatibility with the available materials. The chosen product's tubes and fins also met the requirements for the proper function of the condensation process. In fact, previous experience in the project had shown too narrow tubes could have a negative impact in condensation, so the decision was also influenced by this product having the biggest tube width in the available radiator marketplace. Adaptations were implemented in order to fit this radiator as a condenser for the current installation, such as the opening of threaded hole in the higher chamber of the radiator, to fit in a degassing tap, as seen in the upper part of figure 4.8.

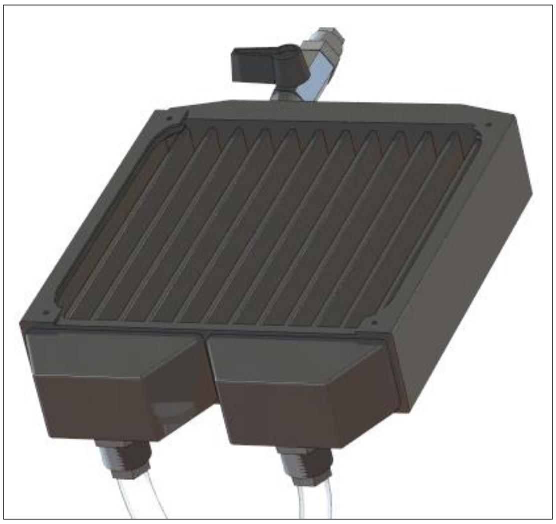

Figure 4.8 - Final condenser design with two pipes and degassing tap (CAD model - SolidWorks).

This degassing process will later be described in chapter 5. An advantage of the Alphacool® product is that it uses G¼ inch BSPT at the lower chambers, matching the available coupling accessories for the rubber pipes. In figure 4.8 the tube fins were suppressed for ease of representation during the CAD process and to make image rendering time shorter. During the experiments phases, a fan was used to force air convection to the developed condenser fins and tubes, although its representation was also suppressed from the above CAD model. The fan, a JetFlo 120 Blue Led by Taiwanese OEM Cooler Master®, was acquired at the same supplier as the radiator.

Reflux condenser setup

The inclination angle is the major parameter to assess when it concerns to reflux condensers. Several studies covered the subject of the inclination angle influence over heat transfer on reflux condensers with two-phase flow. Fiedler et al. [62] studied the effect of the inclination angle on heat transfer in a 7mm diameter pipe filled with refrigerant liquid R134a. Relevant results are summarized in figure 4.9.

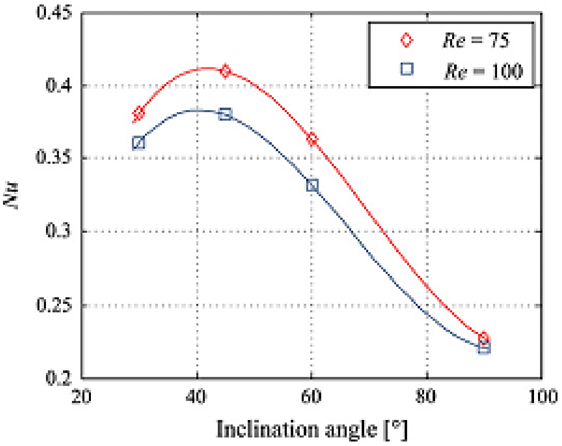

Figure 4.9 – Nusselts number as function of the inclination angle for a reflux condenser [62].

Fiedler et al. [62] claim the optimum inclination angle for the heat transfer lies close to 40° from the horizontal, with double the Nusselt number as in the vertical case, when flow is axisymmetric. Another study on this topic was performed by Klahm et al. [63] featuring circular and rectangular cross-section channels. The authors conclude that for a circular channel the optimum angle is 45°, while for a rectangular channel it is between 30° and 45°. Following these outcomes, a 45° angle of inclination was applied to the horizontal tubes condenser, for the horizontal facility. As previously mentioned, benefits of this reflux condenser approach comprise enhanced heat transfer in the condenser tubes, a smaller amount of necessary subcooled liquid, ease of design implementation, with one less pipe, leading to a more compact product.

4.4. Vertically oriented prototype facility

The major driving force for the design of the vertical prototype was the attempt to overcome the negative effect of using connecting pipes between the evaporator and condenser in a reflux setup. This will be discussed in detail in chapter 6. Hence, a potential configuration emerged as a one-body compact assembly of the condenser and evaporator into one circulation chamber only. This would further reduce the dimensions of the product to devise, being an important measure towards product development, considering the strong geometrical restrictions to install such a cooling device. In fact, since the cooler is intended for fitting on a CPU inside a computer, concerns regarding the available space inside the computer body were to be addressed, so a CAD model of the computer's interior was created, as a reference for the cooler's CAD assembly. For the computer space CAD model, a Cooler Master® Elite 370 case and an Intel® DH67BL motherboard were used, being part of the computer in which the prototype would later be mounted. The resulting model is as follows in figure 4.10.

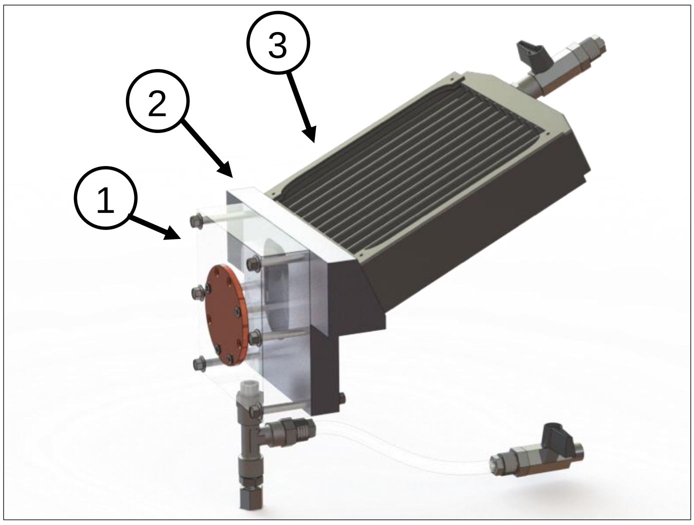

Figure 4.10 - Final design for prototype with vertical oriented hot surface (CAD model - SolidWorks).

The three major components of the final assembly are: (1) The evaporator body, where the boiling occurs; (2) The middle body, an interface between the evaporator and condenser; (3) The condenser, with further adaptations after it was used in the horizontally oriented facility. With the purpose of developing a compact vertical prototype like the one above, many challenges were to be overcome, and many design iterations and attempts were carried out before reaching the final design. Challenges like the impossibility to keep the reflux condenser at a 45° angle with the horizontal due to computer space constraints; the fitting of the condenser to the remaining parts; the materials to build the evaporator and middle body; the correct pairing of the surfaces to the evaporator and this one to the middle body; the surface roughness tolerances in the interface from the evaporator to the middle body; The toughest part to design was the middle body. It underwent the biggest number of design changes through the process, taking the longest time to manufacture. In fact, it is a crucial component, of major importance to the structural stability and good function of the system. Next sections will cover some of these design iterations and overcame challenges, as a means of sharing the acquired knowledge base for future projects with similar specifications.

4.4.1. Compact one-body design

The initial challenge to address was, under the assumptions of a vertical hot surface, a reflux condenser and a continuous fluid chamber absent of pipes, to decide which approach would be used to connect the evaporator and condenser, ensuring structural strength, size compatibility with the computer case and which technology to use for the connections, to make the assembly leak proof. Leakage would later prove to be the biggest challenge to overcome, with HFE-7000's significantly small surface tension, behaving in a much different way than water and other common fluids. On the other side, since the system chamber pressure is most frequently lower than ambient pressure, it must also account for leakage from external air into the system. Hence, it would be of major interest to design the prototype with the minimum possible number of parts and interfaces between them, to minimize the number of leak risk regions. Another step for the development of the one-body design was to cut the condenser's two lower threaded plenum chambers, opening its lower side and leaving a 3 mm contour of the initially existing plenums to then pressure fit this contour into whichever middle component was to be developed. This cutting procedure was performed in the department's shop floor, with a horizontal band saw machine. Figure 4.11 shows the condenser after the cutting process:

Figure 4.11 - Condenser component after band saw machine cut.

Four design project iterations were necessary to reach the final stage. The initial design project was very similar to the final obtained model, since it naturally resembles the most compact approach for the desired end. It accounted for the same three components and with similar shapes. Differences were at the shape of the inner fluid chamber, with more complex contours than the final rounded-corners rectangular shape. The final design accounts for four screw connections to attach the copper surface to the evaporator body, whereas the first one had the same four connections but disposed in a different way, in a symmetric cross shape, which required for a threaded hole in the middle of the inner chamber, making it more complex to manufacture. Additionally, the outer six fixing threaded studs for connection of the evaporator and middle bodies were the same for the initial and final designs, although for the first, all of them were passing through and had washers and nuts in the extremities, requiring for two boxes to be cut on the top surface of the middle body, since the backside was unreachable due to the presence of the condenser body. For the final prototype, the top two studs are screwed into threaded holes in the upper region of the middle body instead, as can be seen in figure 4.10. Finally, all these manufacturing complexities caused all the available shop floor technicians in the department to deny the machining of such components and that put the author's efforts away from this approach for a period, seeking for alternatives and easier to manufacture designs.

The second and third design projects were similar and mostly based on simpler shapes assembled together. These easy shaped bodies would be easy to find available in the department's material inventory or to manufacture by the author as required. The second design consisted of a horizontal cylinder as the evaporator, followed by a square volume body as an interface to a second, equal cylinder at a bigger height. This second cylinder would then connect through two pipes (one above the other) into yet another cylindrical chamber where the condenser's open side would fit in. This design approach was quickly left behind as some premature CAD models had shown the whole final product would be too complex and too big to fit the computer case. In an attempt to minimize and simplify this approach, the third design project featured an adaptation where once again there would be no need for the connecting pipes, by directly connecting the second cylinder into the condenser plenum cylinder, as the following figure denotes:

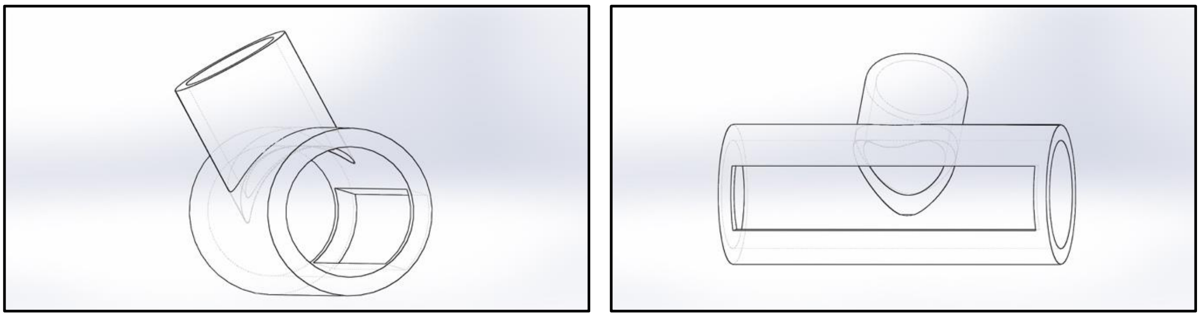

Figure 4.12 - Design approach, 3rd step.

Although this adaptation could effectively reduce the general dimensions of the product, it was still not enough, besides the emerging problem with excessive surface interfaces and parts, increasing the risk of leaks. In fact, the current third design project featured at least eight different main structural components to assemble, whereas the first design featured only four.

So, a new focus on the initial design emerged, and manufacturing simplifications were sought to surpass the previous shop floors denial. With the advice of their machining expert technicians, solutions started to roll-out and an easier configuration was designed which met all the requirements. An important design aspect of the final configuration was the condenser angle with the horizontal. As mentioned, it was impossible to keep the optimal 45° angle due to unavailable space within the computer case. A dimensional analysis for the current configuration set the maximum allowed angle as 26°, and that was a crucial aspect of the middle body design, in which the condenser fits. The 26° inclination still allows for a fully developed condensed laminar flow within the tubes, being a suitable compromise solution. The following figure shows a section view of the final facility, displaying the whole inner chamber:

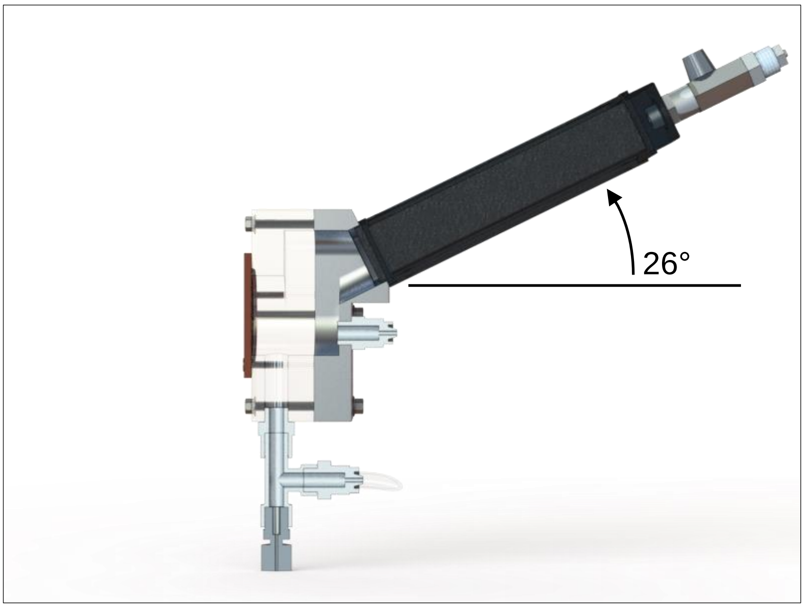

Figure 4.13 - Final vertical oriented surface prototype midsection view.

This figure allows for a good prediction of the fluid dynamics in the interior of the system. The amount of liquid must be carefully controlled at operation in order to achieve the equilibrium between fully submerging the hot surface and not flooding the condenser's entrance. The designed shape allows for this equilibrium to be achieved, and later experiments show the good functioning of the system, with surface dry-out avoided up to very high imposed heat fluxes. Finally, all parts in the proposed design as seen above were adapted or available, except the evaporator and middle body, having these two been accepted for manufacturing at the shop floors. The following sections will deal with specific challenges found during the design and manufacturing phases of these two components, as well as materials selection

4.4.2. Evaporator body

Since the academic side of this project requires the visualization of the boiling fluid flow, some transparent or translucent component had to be included in any prototype to allow this objective to be fulfilled, even if just in qualitative terms. For the previous horizontal facility, vast majority of components except the condenser were indeed transparent. For the current one, the flow visualization could mean a bigger challenge, as not many transparent materials are available for machining processes. Acrylic tubes had previously been used for the horizontal prototype's evaporators, and once again, it was decided to use acrylic as a material for the evaporator body. On one side, it would be easy to machine, whereas glass wouldn't, but on the other side, when machined with conventional available machines the surface finish wouldn't be good enough to make the material fully transparent. In fact, every machined surface of the evaporator body became translucent only, although allowing for a proper flow visualization, as will be shown later in chapter 6.

Another important aspect of this component's design was its fixing connection to the copper surface. Every tested copper surface features eight passing-through holes suitable to fit M3 flat-head screws, arranged in a circular pattern. An initial discussion regarding the use of all eight connections for extra leak safety concluded that it wouldn't be possible, due to unavailable volume to open threaded holes in the region where these would overlap the evaporator's inner open chamber. Then, it was decided to use four screw connections only, applying the proper mentioned O-rings and anaerobic adhesive. These four screws would ideally be symmetrically dispersed around the surface, but again due to the dimensional constrains, the resulting screw pattern is only vertically symmetric, with two screws in the bottom of the surface and two others in its sides, as easily perceived with the following figure:

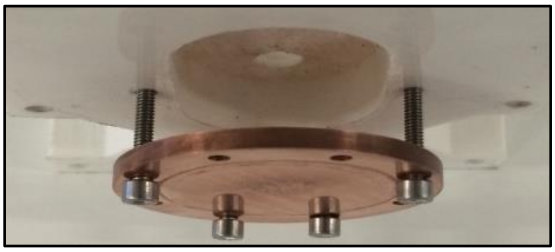

Figure 4.14 - Screws pattern in copper surface.

Please do note this figure does not feature the evaporator body neither the screws used in the final prototype, but represents the previously described physical constrain and the opted solution, displaying the same contour geometry as the evaporator body.

4.4.3. Middle body

This was the lengthiest component to design and conceive in the vertical prototype. It is the interface component combining the geometries from the evaporator and condenser side. Following the initial attempts to make transparent material components, this middle body was also thought to be manufactured in acrylic material. But due to the high complexity of its mechanical design and limitations with available shop floor machinery a new, innovative and more flexible approach to manufacturing was sought and investigated, as presented next.

3D printed

The 3D printed middle body project went through three different approaches, with three resulting prototypes, with increasing experience and learning about the process. For the first prototype, the wish to obtain a transparent component was still considered and a transparent nylon printing material filament was used. To achieve the desired result, the printing fill rate parameter was also set to the maximum so that the density would be the highest, since the transparency requires a highly homogeneous body. Unfortunately, for a consumer-grade printer, the author found out such homogeneous state is not reachable through this process, and the obtained prototype was roughly translucent only. Besides that, for that printer, due to high thermal grades during material filament melting and deposition at the defined fill rate, the prototype's upper surface was bended and the designed shape was not possible to achieve. New filament materials like the clear HDglass™ by FormFutura®, which offer excellent transparency characteristics, have meanwhile emerged and could be a better suit. Further investigation on 3D printing materials for transparency purposes is recommended for future works, as well as ways to surpass the printing thermal gradient issue.

For the second prototype, transparency was left behind and a white 2.85MM EasyFil™ PLA by FormFutura® was used in an Ultimaker^2 printer. Some design changes were applied to reduce material usage, since full design flexibility was available through this process. Figure 4.15 shows the ongoing printing process.

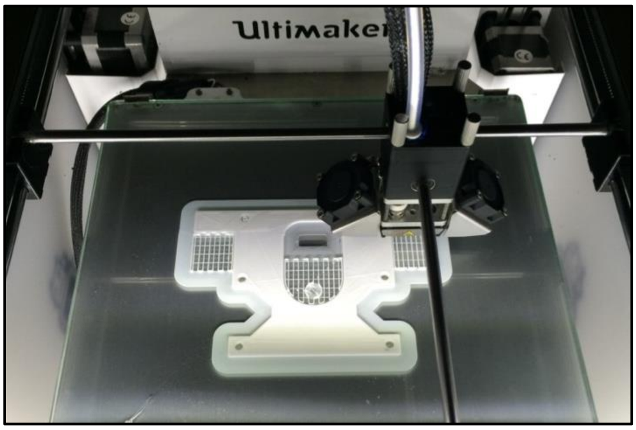

Figure 4.15 - Ongoing 3D printing process.

The prototype was successfully built with the desired shape. It was then fitted and glued to the condenser, with an epoxy glue, and the resulting assembly was structurally stable. So, the new vertically oriented facility was cold tested for leakage and hot tested for heat load resistance. Once again, results were not good, as, against expected after the fill rate was once again set at a high value, the component presented leakage through its body. So, a new problem with porosity was found out, which didn't allow this raw material to be used, even with high fill rates, for such a consumer-grade printer. The facility was then disassembled with an unavoidable damaging of the 3D printed part. A third and final prototype was printed with the same material and printer, but with maximum fill rate and some printing process improvements for porosity decrease. Later, it was decided to apply a water-proofing resin surface treatment and good results were obtained avoiding porosity through the component's body, but still another issue was noticed as for such 3D printed and resin treated surfaces, the finish and roughness profile was very rough and caused leaking at the surface interfaces of the middle body with the consecutive evaporator and condenser bodies. This issue put an end to the 3D printing project and a more conventional approach was then adopted.

Aluminium machined

Finally, at the expense of a bigger manufacturing budget, the component was requested for build at one of the university's shop floors (NOF, Núcleo de Oficinas, Técnico Lisboa), with some design changes discussed with NOF's personnel, for machining enabled production. It was decided to be built with aluminium, due to its light-weight and strength characteristics. One of the requested specs was for the finest surface roughness tolerance the shop floor could achieve with their machinery, for minimization of leak risk in the evaporator to middle body surface interface. The resulting prototype was successfully able to operate without leaking and enabled the project to proceed into experimentation and real condition tests. The figure below shows the assembly of the aluminium part and the condenser, glued to the first with an epoxy glue:

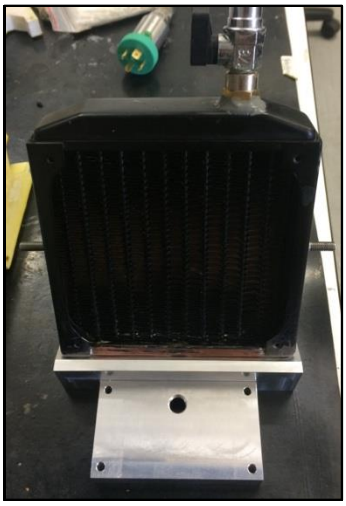

Figure 4.16 - Aluminium middle body and condenser assembly.

The figure also displays two screws and the degassing tap, around the condenser. These were glued using a two-part metal weld glue, using it as a leak cover in the degassing tap's case.

Figures displaying the whole resulting assembled prototypes will be featured in chapter 6.

5. Experimental methodology

The present chapter gives an overview of the followed methodology, covering the used control and measurement instruments and systems, the signal processing and data handling and recording. It covers the production methods for the manufacturing of the tested copper surfaces, as well as a characterization of each surface. It wraps up with an overview of the experimental procedure followed during the preparation and execution of each set of experiments.

5.1. Instrumentation and acquisition

For a safe and methodical execution of experiments and gathering of relevant data, an electronic system was developed enabling for both the controlled operation of actuators, like the heat load applied to the CPU transistor simulator and the acquisition, processing and recording of data signals from the thermocouples and pressure transmitter. An overview of the experimental setup will thus be introduced, as well as its comprised electronic circuit. The obtained LabVIEW main algorithm for signal processing and user interfaces for control of the experimental campaigns will also be introduced.

5.1.1. Electronic control and acquisition system

The experimental setup is schematically represented in the following page, figure 5.1. It comprises the thermosyphon system in the bottom, which parameters were tested during experimental campaigns, being the main region of interest. Around the thermosyphon, the components which interact with it are represented: the transistor which simulates the heat release effect of a processor (as previously introduced), the sensors (k-type thermocouples and pressure transmitter) and the fan which forces convection on the thermosyphon condenser's fins to remove heat, working as a heat sink. There are three thermocouples: one is placed in the region of the transistor's surface, to measure the copper surface to transistor junction temperature, representative of the temperature a CPU would achieve in real conditions; the second thermocouple is an insulated probe inserted inside the thermosyphon's evaporator, near the boiling side of the copper surface, to measure the saturation temperature in the system's closed chamber; the third thermocouple is upstream to the condenser's fan forced convection air flow, to measure a reference ambient temperature to which heat is being removed, as seen in figure 5.2. Results obtained in chapter 6 are computed from these thermocouple readings. The pressure transmitter was physically attached to the thermosyphon's closed chamber, and its signal was amplified with a power source regulated to 30V, as stated by the sensor's requirements. Its readings were converted to digital by a National Instruments® USB-6008 DAQ board, also connected to the computer through an USB cable. The two remaining components, the transistor and fan were control required, so they are attached to an electronic control board developed within the scope of this work, which will later be presented. Through this control board, signals from the computer converted to analog in the NI®

DAQ board were sent to the fan to control its rotating speed and the transistor to control the power dissipated by Joule effect. An additional 12V fan is connected to the control board to cool down some of its electronic components, such as four resistors. To provide the necessary voltage to modulate and feed the many components, two power sources are connected to the control board, one deploying 60V (for the high-power transistor application) and an Intel® computer power source unit, from which a 12V voltage was obtained to feed the fans and electronic components such as an operational amplifier comprised in the control board.

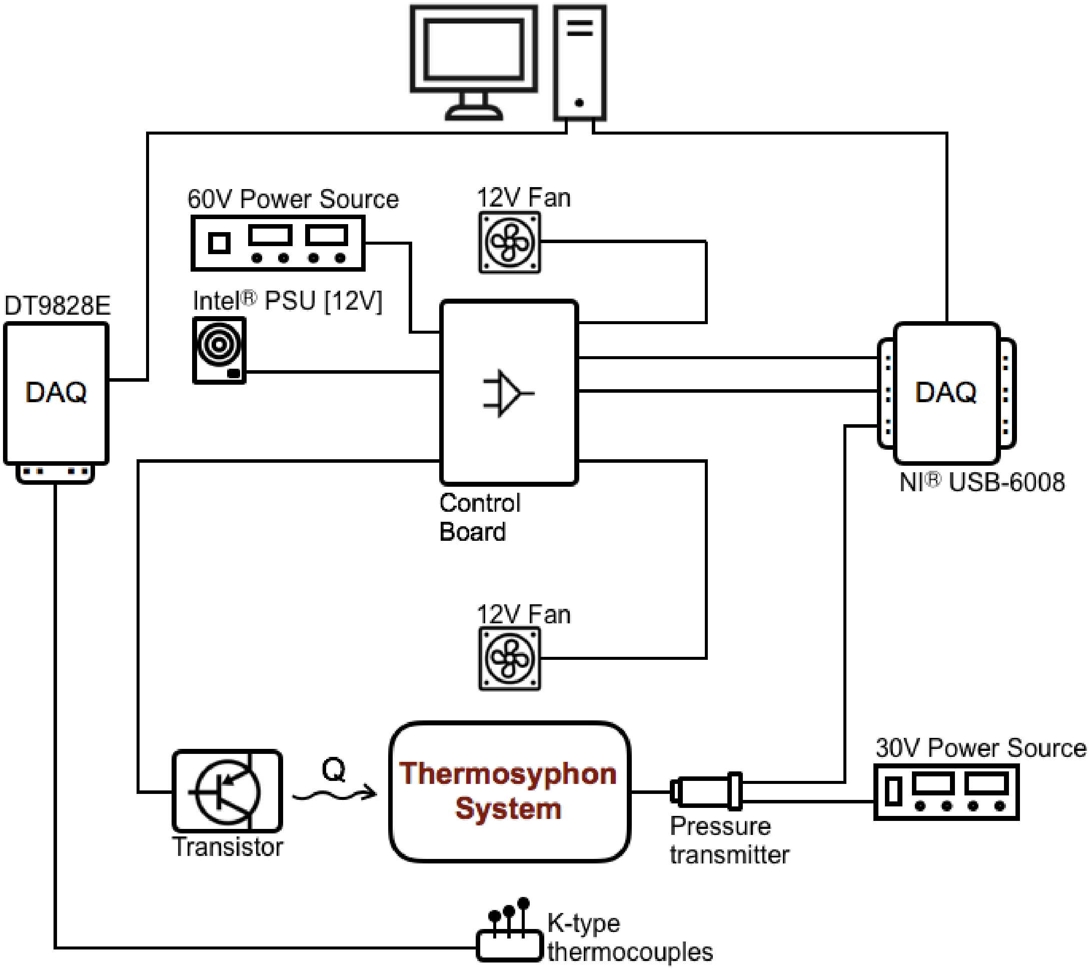

Figure 5.1 - Electronic control and acquisition system diagram.

It is important to note the previous diagram is purely representative of the experimental setup and the icons for each component are not in scale with their real physical dimensions.

Deepening the understanding of the used sensors, they are presented next. The pressure transmitter is manufactured by the Italian company Gefran®. Its product model is TK-N-1-E-NO2U-M-V, with 0 to 10 Vdc output and -1 to 2 bar measurement range and has a ±0,5% FSO Typical accuracy. It features a G¼ gas female pressure connection, a 4 pole connector solenoid as electric connection and a fast response time (<1 msec). The three thermocouples are manufactured by Omega®, being two K-type calibration MTSS series probe thermocouples, while the one measuring ambient temperature is a surface thermocouple of the SA1XL series. These thermocouples have an accuracy of ±1°C. The

Analog to Digital Converter used for these thermocouples is a DT9828E by American company Data Translation®, with 24-bit conversion and an accuracy of 0,1 K. Figure 5.2 shows two midsection cuts of the horizontal and vertical facilities, clarifying the thermocouples and pressure transmitter measurement positions.

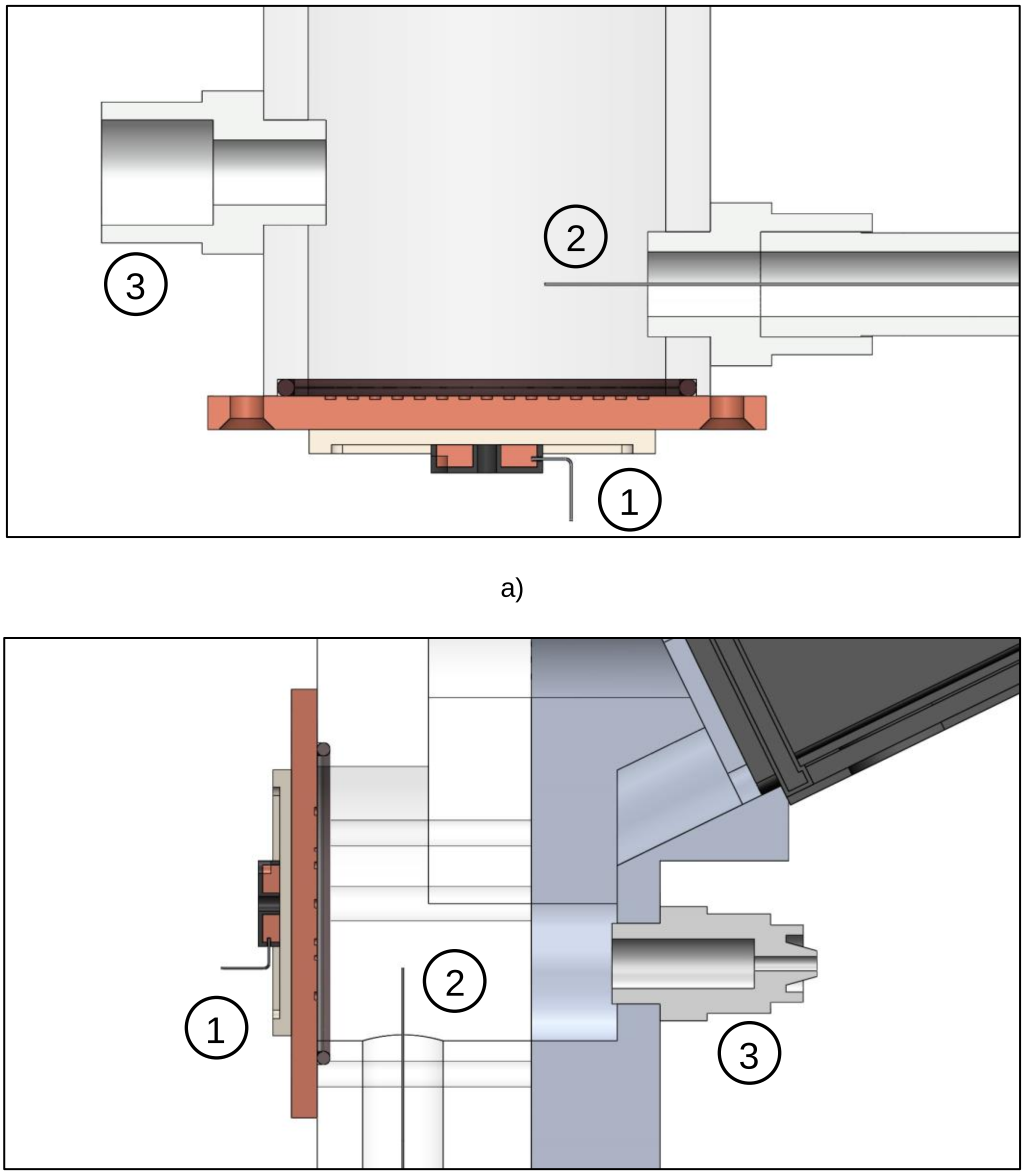

b)

Figure 5.2 - Horizontal and vertical facilities midsection cuts. [a) horizontal; b) vertical]

For both images, number (1) is the first probe k-type thermocouple, used for measuring the junction temperature T_j, in the nearest available position, inside the transistor’s own copper heat spreader. Number (2) is the second probe k-type thermocouple, used for obtaining the saturated vapour-liquid temperature, T_{sat} in the region near the hot surface, being placed 1 cm far from the later. Number (3) is in both images the position of the accessory used to connect a small diameter pipe leading to the pressure transmitter, where inner chamber pressure p is interpreted and transferred for acquisition.

Covering now the topic of the electronic control board, it consists of an electronic circuit which enables the imposition of the heat generated by the transistor, as well as the control of both the 12V computer fans. Figure 5.3 displays a simplified scheme of the circuit and the connected transistor, related to its power control component.

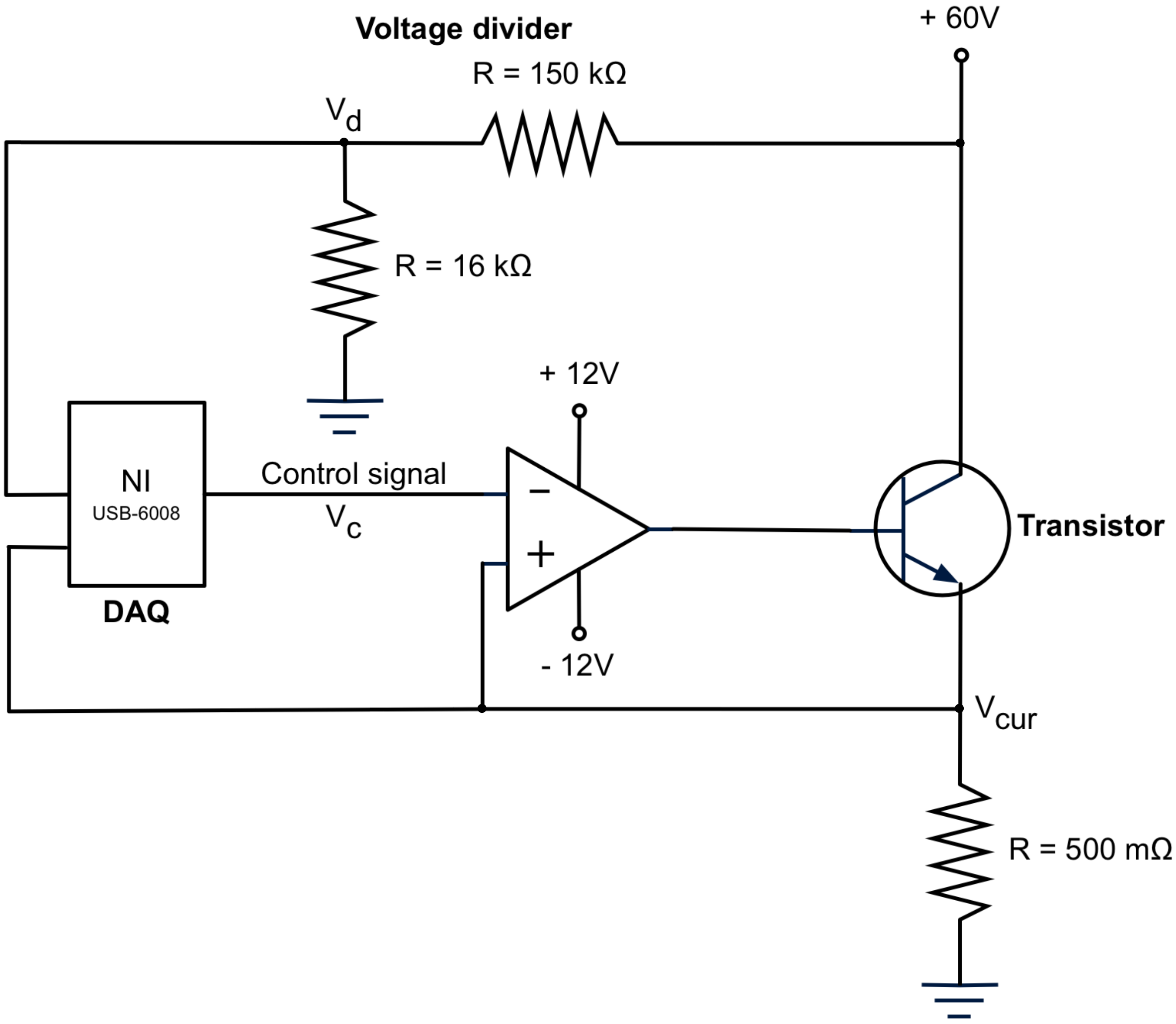

Figure 5.3 - Transistor power control circuit scheme.

The heat dissipated by Joule effect in the transistor is obtained as the product of the voltage drop across the transistor collector and emitter terminals and the current flowing through. Voltage drop is acquired by means of a voltage divider, directly connected to the NI DAQ board. As a result of the signal processing carried through in LabVIEW environment (which will be later addressed), this board then outputs a low voltage control signal V_c to one of the terminals of the Op-amp. This Op-amp is working as a comparator, sending its output signal to the transistor's base terminal, adjusting the gain accordingly so that the output voltage at the emitter terminal of the transistor, V_{cur}, is the same as V_c. The Op-amp is therefore causing the following relation:

$$V_{cur} = V_c \tag{5.1}$$

With this imposed V_{cur} and knowing V_d, i.e. the divided voltage reading which can be used to obtain the power source voltage V_{ps} in LabVIEW environment (as later seen in Voltage divider subsection below), which should compute to 60V, one can know the voltage drop across the terminals of the transistor, $V_T = V_{ps} - V_{cur}$. To obtain the current value flowing through the processor, Ohm's law is used across 4 parallel Burdon precision high power resistors of $R_B = 2{,}0\,\Omega \pm 1\%$, cooled by the top 12V fan as featured in figure 5.1, to maintain the temperature within the valid region of accuracy, as stated in the resistors data sheet. Overall resistance R for the 4 parallel resistors is given by the expression,

$$R^{-1} = 4 * {R_B}^{-1} = 4 * 2^{-1} = 2 \Leftrightarrow R = 0{,}5\,\Omega = 500\,m\Omega \tag{5.2}$$

as denoted in the bottom resistor represented in figure 5.3. With this resistance value and knowing the respective voltage drop across the paralel resistors, Ohm's law states:

$$I = \frac{V}{R} = \frac{V_{cur}}{R} = \frac{V_{cur}}{0{,}5}\ [A] \tag{5.3}$$

This current value is the same current flowing through the transistor, $I = I_T$, and knowing that the power source voltage is $V_{ps} = 60\,V$, the dissipated power can finally be computed as:

$$P_T = V_T * I_T\ [W] \tag{5.4}$$

which, replacing the voltage drop difference and Ohm's law current value is equivalent to

$$P_T = \left(V_{ps} - V_{cur}\right) * \frac{V_{cur}}{R}\ [W] \tag{5.5}$$

With $V_{cur} = V_c$, one can now derive the expression to compute the control signal required to obtain a certain dissipated power value, P_T at the transistor:

$$P_T = \frac{V_{ps}V_{cur}}{R} - \frac{V_{cur}^2}{R} \Leftrightarrow V_{cur}^2 - V_{ps}V_{cur} + RP_T = 0 \tag{5.6}$$

Being the mathematical solution of the equation the following, with two solutions for any initial conditions, R, P_T and V_{ps}.

$$V_{cur} = \frac{V_{ps} \pm \sqrt{{V_{ps}}^2 - 4RP_T}}{2}\ [V] \tag{5.7}$$

As V_{cur} values bigger than V_{ps} lead to a negative heat load power, P_T, these values don't have a physical application to the current problem, being the final solution to the controlled voltage V_{cur} as follows:

$$V_{cur} = \frac{V_{ps} - \sqrt{{V_{ps}}^2 - 4RP_T}}{2}\ [V] \tag{5.8}$$

and for the current problem's conditions, with an actual measured resistance of $R = 502{,}82\,m\Omega$, and $V_{ps} = 60\,V$, V_{cur} in function of P_T comes as:

$$V_{cur}(P_T) = \frac{60 - \sqrt{3600 - 2{,}0113\, P_T}}{2} = 30 - \sqrt{900 - 0{,}5028\, P_T}\ [V] \tag{5.9}$$

Voltage divider

From Ohm's law for electric circuits $V = R * I$, and recurring to Kirchhoff's laws of electric charge conservation over an electric circuit, derives the following relation for the voltage division,

$$V_{out} = \frac{R_2}{R_1 + R_2} V_{in} \tag{5.10}$$

, being $R_1$the upstream and R_2 the downstream resistor to V_{out}, which enables the measurement of the power source voltage, otherwise too big for the NI DAQ range. With $V_{in} = V_{ps} = 60\ V$, $R_1 = 150\ k\Omega$ and $R_2 = 16\ k\Omega$, the expression for $V_{out} = V_d$ comes out as:

$$V_d = \frac{16}{166}\, V_{ps} = 0{,}0964\, V_{ps} \tag{5.11}$$

However, the used resistors featured a ±5% precision and later calibration measurements shown that the actual division ratio was

$$V_d = 0{,}1015\, V_{ps} \tag{5.12}$$

with $V_d = 6{,}089\ V$ for $V_{ps} = 60\ V$. This divided voltage was then measured into the DAQ board and the division was then digitally compensated back to the original power source value with properly calibrated transfer equations within the LabVIEW software, as will be presented in the next section covering signal processing.

5.1.2. Signal processing

Having just introduced the analogic side of the experimental setup, this section will now cover the digital side, namely what kind of data handling and processing is occurring within the computer's LabVIEW and QuickDAQ software and the two DAQ equipment used within this work. Covering the simpler process for the Data Translation□ DAQ first, its three digital temperature signals in degrees Celsius are directly read and plotted with the compatible software QuickDAQ provided by the manufacturer (Data Translation□). It offers the additional option to extract a data log into Microsoft□ Excel, useful to analyse the collected data. QuickDAQ plotting function was used during the realization of all experiments for visualization of junction temperature T_j, the critical safety parameter which should not exceed a limit or should not sharply increase when a near-critical heat flux state was attained. Annex A.1 (as found in Annexes section in the end of this document) shows a snapshot of the QuickDAQ in typical experimental operation conditions.

Now focusing on the dissipated power control function, among others, implemented on National Instruments□ LabVIEW environment, a more complex data processing was necessary, both to obtain the DAQ output power control signal V_c, as to accurately plot the remaining variables such as system pressure P, the computed transistor current I_c or the transistor computed dissipated power due to joule effect P_j (which should match the actual physical equivalent power P_T). Figure 5.4 in the next page shows a scheme of the algorithm in which the LabVIEW block programming was based.

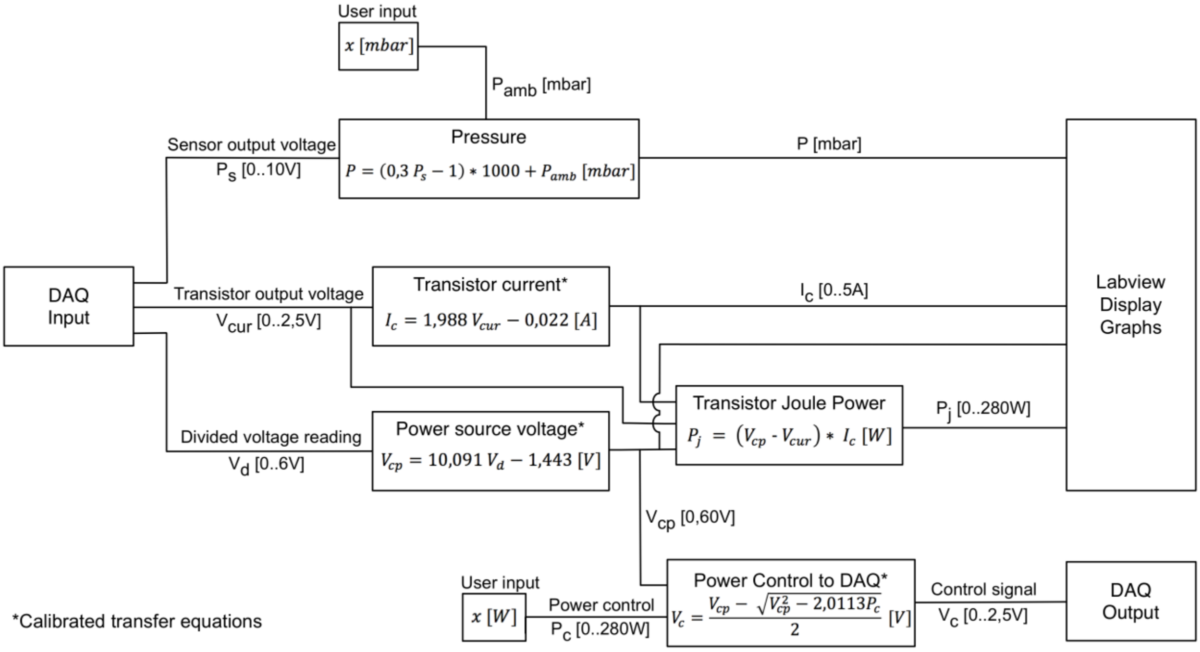

Figure 5.4 - LabVIEW visual programming algorithm diagram.

Three analog signals are input to the DAQ board where they get converted to digital. These digital signals are then USB transferred to the computer's memory where they are read by the LabVIEW software. Regarding the divided voltage reading V_d first, this is used to compute the power source voltage V_{cp}, through the following experimentally calibrated transfer equation,

$$V_{cp} = 10{,}091\ V_d - 1{,}443\ [V] \tag{5.13}$$

From this value and the user defined desired transistor power value P_c, the control signal V_c is obtained through the adaptation of equation 5.8 for the current conditions, $V_{ps} = V_{cp}$, $R = 502{,}82\ m\Omega$, $V_{cur} = V_c$, resulting in:

$$V_c = \frac{V_{cp} - \sqrt{V_{cp}^2 - 2{,}0113P_c}}{2}\ [V] \tag{5.14}$$

Note that it is important to obtain this calculated power source value V_{cp} and have it plotted on graph to make sure the voltage divider is in proper function and the manually fine regulated power source voltage value of 60V matches the readings. This assures the dissipated power is the same as the user defined value. V_c is then USB transferred back to the DAQ board where it gets converted to analog. As previously seen, due to the comparator Op-amp, the analog components of the signals V_{cur} and V_c are forced the same but it is still important to read V_{cur} into the DAQ for extra warranty the circuit is properly functioning. This equality also causes the calculated transistor current I_c and transistor Joule Power P_j to be indirectly dependent of the user defined power control value P_c, besides of the correct calibration of the transistor current transfer equation, based on the real measured resistance on the four $2{,}0\ \Omega \pm 1\%$ parallel resistors. The calibrated equation resulted as:

$$I_c = 1{,}988\, V_{cur} - 0{,}022\ [A] \tag{5.15}$$

and for the joule effect dissipated power, its digital component equation is as follows, according to equation 5.4,

$$P_j\ =\ \left(V_{cp}\ -\ V_{cur}\right) *\ I_c\ [W] \tag{5.16}$$

As for pressure, P_s, the third signal read into the DAQ board, Gefran manufacturer specifies the sensor's output range of 0 to 10V for a measurement range of -1 to 2 bar relative to ambient pressure. The resulting transfer equation for absolute pressure P is then:

$$P = (0{,}3\, P_s - 1) * 1000 + P_{amb}\ [mbar] \tag{5.17}$$

with user specified P_{amb}. As well as T_j, this is an observed critical safety parameter which should not exceed an operational limit set at 1300 mbar otherwise jeopardizing the integrity of the thermosyphon prototype. Minimum and maximum observed P values were about 600 and 1250 mbar respectively.

Although the introduced algorithm represents the major content of the devised LabVIEW routine, it included some additional useful features like a manual slide button to control the thermosyphon fan's rotating speed; a data logging component which recorded all the plotted digital signals into user specified Excel files with buttons to start and stop the recording and possibility to adjust the recording time; an experiment counter which would sum up one number every time the recording would restart and would reset to 0 when a single experiment would finish.

A later version of the routine also included a special feature, found to be very helpful during the degassing process which will later be described in this chapter. It consisted of a pressure control routine which would turn the fan on if the pressure would increase above a value set by the user with a slide button, and turn it off again as soon and if the pressure would decrease back under that set pressure value. A third version of the LabVIEW routine finally included the possibility to apply an automated heat load time sequence, which allowed for the experiments with power profiles as will be presented in next chapter. To trigger the sequence, the user simply had to turn on a switch button. Annex A.2 (as found in Annexes section in the end of this document) shows a screenshot of the designed GUI during a representative operation state.

5.2. Manufacturing and characterization of the micro-structured surfaces

Micro-structured surfaces are characterized by a microarray of structures or microcavities. The main characterization and test parameter for each surface is, as previously mentioned in section 2.3, the S parameter, orthogonal distance between each etched cavity. Several copper surfaces were machined and later went through a finish process, which can be described as follows: they were first abraded with SiC papers (from 800 to 2000 grades), polished to mirror and then ultrasonically cleaned for 10 min in absolute ethanol (A.R. Beijing Chemical Works). Afterwards, the arrays of microstructures were produced by laser etching (FB20-1, New Industries, China). The laser system parameters assessed were the depth and diameter of laser-ablated micro-cavities, respectively 15 and 100 µm according to the supplier. Different surfaces were obtained with different S distance parameters, out of which a set of surfaces was defined to use in all the experiments performed in the present work. Surfaces for this test group are, from this point on, defined and addressed according to a code based on their S [µm] parameters and other characteristics as follows, from biggest to smallest: 600; 400; 42T; 200; 200D; 100; Smooth. Surfaces with codes 600, 400, 200 and 100 are self-explanatory as they respectively have a measured cavity distance parameter S = 600; 400; 200; 100 µm. The Smooth surface simply hasn't been etched, only machined, being used for reference for comparative purposes with the other surfaces. "Irregular" surfaces with codes 200D and 42T differ from the previous ones regarding their etching process and cavities pattern. Surface 200D was manufactured to have a distance parameter S = 200 µm as the previously mentioned 200 surface, but etchings' depth and diameter is bigger, and will later be quantified. Surface with code 42T means it is characterized by having two different S parameter regions, hence the T stands for "Two-regions", with different diameters, being the inner diameter region with S = 400 µm and the outer diameter S = 200 µm, hence the numbers 4 and 2 in the code. The following figure shows a schematic overview of the surfaces for better understanding:

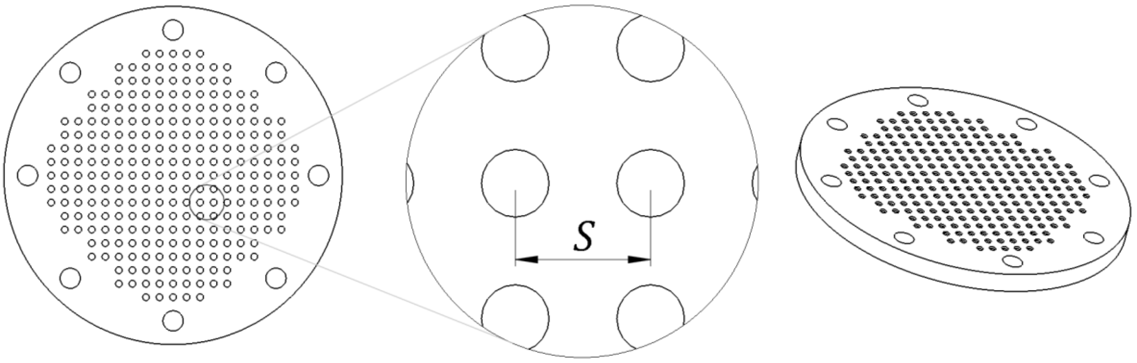

Figure 5.5 - Copper surfaces with cavities model.

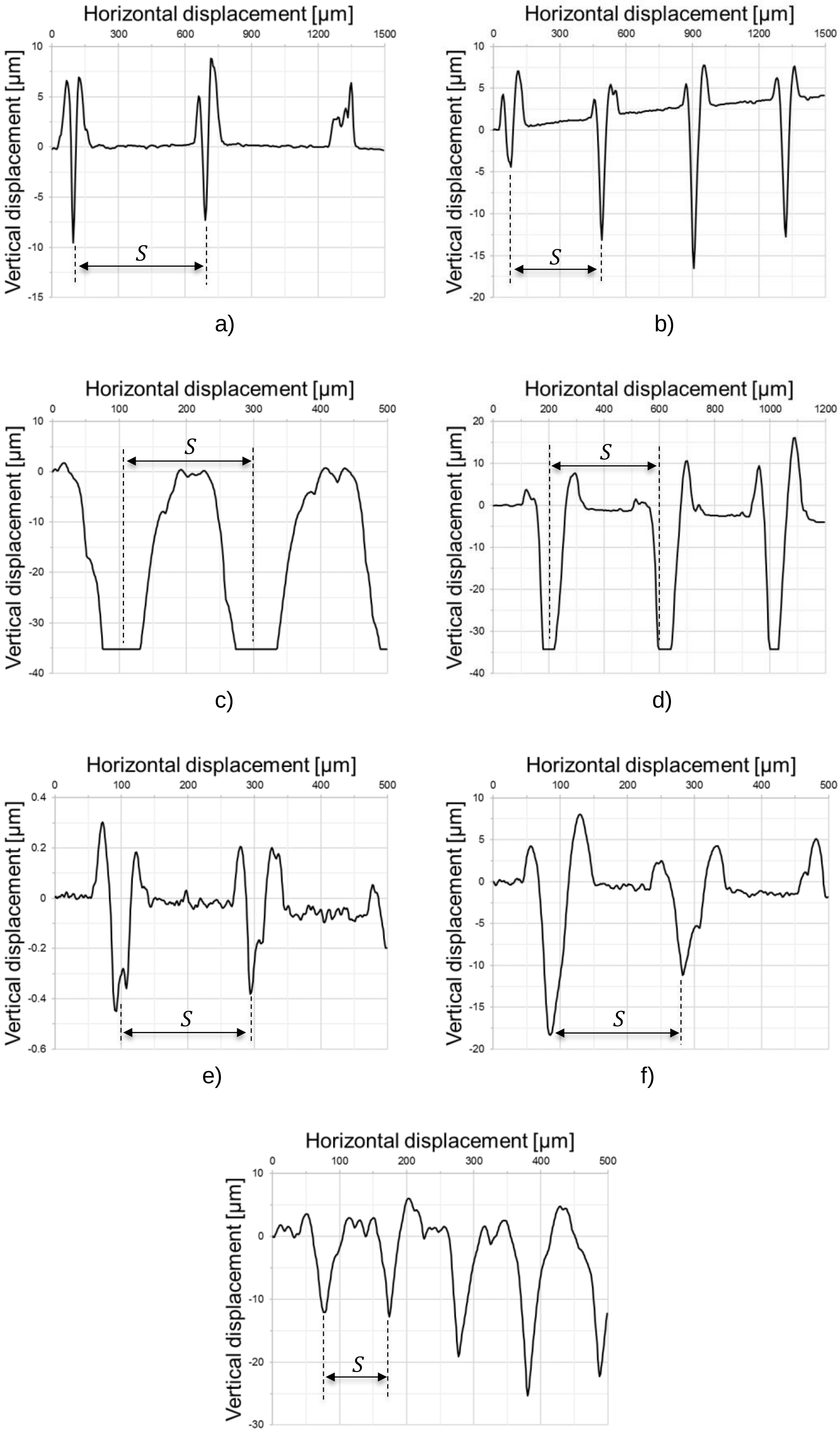

a) b) c) d) e) f) g)

Figure 5.6 - Surface roughness profiles. [a) Surface 600; b) Surface 400; c) Surface 42T external diameter; d) Surface 42T internal diameter; e) Surface 200; f) Surface 200D; g) Surface 100]

The profiles of each test group surface were measured recurring to a profile meter (Dektak 3, by Veeco ©), with a vertical resolution of 0,02 µm. Typical roughness profiles are presented in the previous page, figure 5.6. This procedure was performed to confirm the surface etching characteristics, namely the distance between the cavities and to obtain some more detail in the actual shape of the cavities, and possibly relate that to the heat and mass transfer mechanisms occurring during the boiling process. This profile meter consists of a tiny vertical needle that travels along a surface within a pre-selected horizontal displacement and changes its vertical displacement according to the surface topography, constantly resting on the surface by the action of gravity. In every graph, the x-axis is the distance travelled by the needle while the y-axis represents the vertical displacement of the needle (relative to a reference position zero, which was set at the beginning of the measurement) in nanometres.

One can observe how every surface indeed matches the provided information about S parameters, as in every graph the distance between cavities (noticeable vertical perturbations relative to the reference surface height) matches the respective S distance, established according to the aforementioned nomenclature. One can easily notice how the shape of each cavity does not indeed look like a regular cavity, having an annular material elevation around the margin of the cavity. This is explained by the production process of such cavities. During the laser etching process, part of the material removed from the cavity is deposited on that area around it and becomes solid. The presence of these excess material deposits somehow affect the cavity depth measurement as it doesn't let the needle fully rest on the bottom surface of the cavity, thus explaining the apparent depth mismatching from one cavity to the other in every graph, except in the 42T surface case, where the needle was actually able to reach full depth of 350 µm. Nevertheless, observed depth for other surfaces ranges from 40 to 250 µm. One can also observe that, according to provided details, cavity diameter is roughly 100 µm for surfaces 600, 400 and 42T. Smaller S parameter surfaces, 200D, 200 and 100 present a lower cavity diameter, as the available area for cavities is naturally smaller. Diameter for these surfaces is roughly 50 µm. The 3rd and 4th figures are respective to the same surface 42T but since this one is composed of two different cavity regions, with 200 and 400 µm respectively, each region is represented in its own graph. As for the case of the 5th and 6th figures, these respectively show the profile for surface 200 and 200D. In fact, although they are very similar, both the cavity diameter and depth are noticeably different. Surface 200 is characterized by a diameter of 25 µm while surface 200D's diameter is 50 µm. Depth stands at 40 µm for surface 200 while it goes up to 150 µm for surface 200D. The surface topography is known to affect the contact angles which quantify the wettability, that, in turn, affect the pool boiling heat transfer [29], as revised in chapter 2. However, the fluid used here, HFE-7000 has a very low surface tension, when compared to other common fluids, such as water (see table 4.1), so the equilibrium angles, which are often addressed to characterize wettability were close to zero for all the tested surfaces, hence this fluid is taken as a well wetting fluid for the results analysis.

5.3. Experimental procedure

The current subsection documents all the steps performed during every phase of an experiment. The two first fundamental preliminary phases of every experiment were the surface removing from a previous experiment, its subsequent cleansing and the placement of a new surface on the experimental facility, either be it the vertical or horizontal prototype, and the facility's degassing through a cyclic process to remove all unintended gaseous and dissolved air from the interior chamber. These two phases are introduced first, followed by an overview of the procedure carried through in the actual experiments, both at controlled simulated conditions (horizontal or vertical) and at real working conditions for the final proof of concept tests.

5.3.1. Surface change

Horizontal facility

In order to change the copper surface under test, the current one must first be removed. For the horizontal facility case this is achieved by first letting the system stabilize without any heat load if it was applied recently. Once stabilization was achieved the degassing tap on the top of the condenser should be opened to let air in, thus changing the controlled experimental conditions, which must be re-established afterwards. Air will flood in since typical pressure at stabilized state ranges 650 to 750 mbar, which stands below ambient pressure. Afterward, assembling a liquid syringe into the liquid supply tap on the bottom, all liquid should progressively be removed from the inside of the thermosyphon system, although there will always be a small liquid amount impossible to drain out in the surroundings of the surface. This amount will then evaporate as soon as the system is dissembled. The transistor assembly is then removed from below the Teflon base, unscrewing four nuts which hold tensioning springs which would otherwise push the copper surface up as soon as the evaporator would be dissembled. Next step is to unscrew the four evaporators' threaded studs and nuts which provide the evaporator's structural stability, allowing for a further dissembling of the top acrylic cover and acrylic cylinder of the evaporator. The only part remaining will then be the copper surface, on top of the Teflon base. The surface is then removed and methodically cleansed, with a 20 minute supersonic bath in acetone to remove any impurities in its surface, after a rough manual cleansing with cotton to remove remains of the anaerobic adhesive. It is then safely stored between cotton pads in a plastic container for that purpose. This concludes the procedures for removing and storing a surface, allowing for the placement and test of a new one, as seen next.

To prepare the placement process, one should first apply thermal compound over the copper surface's side which is in contact with the used Integrated Heat Spreader. The same quantity was always used to assure repeatability of the tests. The surface and IHS assembly should then be placed on the Teflon base, in the appropriate cavity position. Afterwards, anaerobic adhesive should be applied on the two O-rings used for sealing in each extremity of the evaporator's acrylic cylinder, followed by a manual placement of the evaporator and O-rings over the copper surface, visually centring the whole assembly, and then closing it with the top acrylic part. Using one hand to keep the assembly together and properly centred, the other hand should then be used to screw the studs and bring stability to the system, closing the evaporator component. In its current state, the assembly should then be left to rest and dry overnight, to reduce the chances of aftermost leakage, and before applying any additional stress to the system. The condenser and fan assembly should then be tightened in the 45° position followed by a proper positioning of the ambient temperature thermocouple. Finally, the transistor subassembly is placed under the IHS, through the Teflon base's cavity. Four equal tensioning springs are then placed on the bottom of this subassembly to assure a constant contact pressure (equal through experiments) between the transistor and the IHS, again to assure repeatability. To assure this a 2 cm mark is used when adjusting the springs' strain. The system should now be prepared for filling with liquid, degassing and experiments.

Vertical facility

The described process is very similar for the vertical facility, although easier and faster during some assembling steps. Since the copper surfaces are screwed to the acrylic evaporator body, a manual placement and centring is not required. Differences from the previously described procedure to remove a surface for the horizontal facility are in fact that for the current one, it is not necessary to dissemble the whole evaporator but only the screwed surface itself, after the transistor and IHS were removed.

When assembling the system, one should then apply anaerobic adhesive over one O-ring which seals the surface to the evaporator body, then screwing the surface to the body. Afterwards, the independent and structurally stable system is screwed to the vertically placed Teflon base for later placing the transistor subassembly. After this, every other step is the same as previous except that the condenser doesn't need to be fixed since its incorporated into the vertical prototype system.

5.3.2. System degassing

After the first stages of surface placement and system assembling, the system can now be filled with cooling liquid HFE-7000. The process is similar both for the horizontal and vertical setups so it won't be discretized as before.

First step is to fill a syringe with liquid. Then, with both the bottom and top taps open, the liquid should be inserted into the system, through the bottom liquid supply line, until the system is full and up until the liquid level reaches some point at the pipe connecting the top tap to the external condensation liquid recovery system. This external system is crucial for the purpose of cost saving, being HFE-7000 a very volatile and expensive fluid, acting as a recovery system for the substance evaporated during the degassing process. After this filling process is complete, the system should manually be moved around and shaken to help any enclosed air bubble or bag to move out of the system. From experience, this probably causes the liquid height to decrease a lot, and more liquid should then be inserted through the syringe. This process should be repeated until the liquid height level decreases no further with shaking.

At that point, both taps should then be closed, turning the thermosyphon into a closed loop completely full of liquid. From this point on, the actual degassing starts. The LabVIEW control routine should be started, using the pressure control functionality and setting this to 1250 mbar, so that the air forcing fan is turned on and condensation begins for safety, at higher pressure values. At this point pressure should be slightly higher than ambient pressure (30 to 50 mbar), due to the liquid column height over the pressure transmitter level (near surface). Then, using this same LabVIEW routine, an initial 5W load should be applied, which starts an observable fluid natural convection. After stability is achieved, the load should be increased to 25W, which will cause the occurrence of nucleation sites. Pressure will slowly start to increase. Steps of 5W should slowly be applied until a maximum of 50W is achieved, or until pressure is increasing at a significant rate of 3 to 5 mbar/s. When pressure climbs above 1240 mbar, the degassing uppermost tap must be opened to let evaporated vapour out. This will rapidly decrease the pressure in system, and the tap should carefully be closed back when pressure is as low as 1100 mbar (it can't be lower than ambient pressure or air will start to flow into the system). It is noticeable a lot of liquid will flow out during that process. Now, a cyclic process starts, where the operator must repeatedly open the tap to let vapour out and decrease the pressure, and close it back for pressure to increase. From experience, the tap was often open for about 1 to 3 seconds only, which was enough. At a certain point, after about 10 repetitions, the heat load should be taken off, turning off the power source, and instantaneously the fan should be turned on to full speed with the LabVIEW routine and top tap closed, to let the system rest and achieve thermal and pressure stability. System pressure should be lower than ambient pressure, for instance 800 mbar. This is a warranty the degassing process is properly achieving its purpose, before all excess liquid is evaporated. The cyclic process should then be continued, with a direct 50W heat load once again applied to the system. As many repetitions should be performed until the intended liquid height is achieved, typically about 40 to 50 repetitions. Once again, the heat load should now be removed, and the fan turned fully on to enhance condensation and cool down the system, until it achieves stability. If system pressure at steady state is within a range of the pure HFE-7000 saturation pressure for the given ambient temperature the degassing was performed correctly. This range is recommended as 20 mbar, but can go up to a maximum of 50 mbar above saturation pressure, without affecting the thermosyphon system's function.

5.3.3. Controlled simulated conditions

Steady-state experiments

For the characterization of the structured surfaces boiling, both on the horizontal and vertical oriented facilities, which was the main experimental campaign, an experimental procedure was followed, where a number of measurements were taken from the sensors connected to the system. These measurements were taken after the dynamic thermosyphon system (evaporator and condenser cycle) stabilized into a steady pressure and temperature state, after every transistor joule effect power step increase. Indeed, all tests were characterized by a heat load ascending through time, with step increases of different amplitude, as will be described. A single observation was the mean result value of a 20 Hz AD conversion sample rate lasting 3 seconds, hence an average of 60 values.

A full test may comprehend a variable number of measurement points associated with each power step, varying according to the occurrence of critical heat flux, or in case it doesn't occur, can go up until a maximum safety heat power value of 250W is reached. This value is set according to the specifications of the electronic control system. Above 250W, risk of electronic components overheating and further damage is too high for continuation of measurements.

In a CHF situation, a safety routine is implemented in the control system which detects sudden temperature increases and immediately cuts the power source and stops the measurement readings. Otherwise, the high temperatures attained in a near film boiling regime would damage the transistor and the experimental facility. It is of major importance to characterize the surfaces' heat flux value to which CHF occurs, so that safe usage design parameters can be established for the product to develop, which functions under the nucleate pool boiling regime only. It is also important to clarify how the heat flux values are computed. Being defined as the heat flowing through a given surface area per unit time, the heat flux is considered for the purpose of this work as the ratio between the transistor Joule effect dissipated power (heat per time) and a circular area in the tested surfaces accounting for the inner diameter of the acrylic tubes used as evaporator bodies, 32 mm. For the final proof of concept analysis, same approach is used although dissipated power is given by the computer system software, as seen in the next section.

Every surface is tested 5 times, for repeatability. For each test, the first measured point is at room temperature and 0W power, followed by the mentioned power step increase sequence. The sequence is as follows: 5W steps from 0 to 40W; 10W steps from 40 to 250W or the occurrence of CHF. The first stage of 5W steps is due to a more accurate observation of the transition regime from natural convection to nucleate boiling, through the appearance of the first bubbles.

Transient experiments

Transient state measurements were only performed on the vertical prototype, and followed in every way a very similar procedure to the previous steady-state experiments, meaning the same sensors and remaining equipment, respective connections and computer user interfaces were used. Minor adaptations were implemented in the later LabVIEW GUIs and virtual instrument routines, such as the programming of a time-dependent variable to substitute the user input power value as the mentioned control power variable P_c, allowing the application of a transient power profile. The major difference now is related to the observation length. Where previous steady-state observations took 3 seconds to represent an operation point, at these transient observations the interest is to register all variables as they change in time, so the observation time can be as long as the experiment states, or until a steady state is again attained. The experimental procedure can be described as follows: first, the system should be left to rest with no heat load, until it stabilizes at ambient conditions; data recording should then be activated, followed by the triggering of any heat load step or combined step sequence for which the dynamic system response is sought; data recording should be stopped whenever temperature and pressure stabilize.

Each surface was tested under five different transient scenarios: four single power steps from quiescent state and a power profile. The four power steps were chosen as 20W, 60W, 100W and 140W, covering the span of typically applied power values and representative of different boiling regimes, as observed during previous steady-state campaigns. The transient power profile mentioned above is an adaptation of the benchmark CPU power profile proposed by Isci and Martonosi [64], which simulates four different regions of typical CPU operation such as computations with integers and floating points, cache hits, taken branch predictions and the use of software Gnumeric. The current adaptation keeps the time-dependency of the authors' profile but scales the power values proportionally to a maximum of 100W where before it was 60W. Figure 5.7 depicts the current power profile:

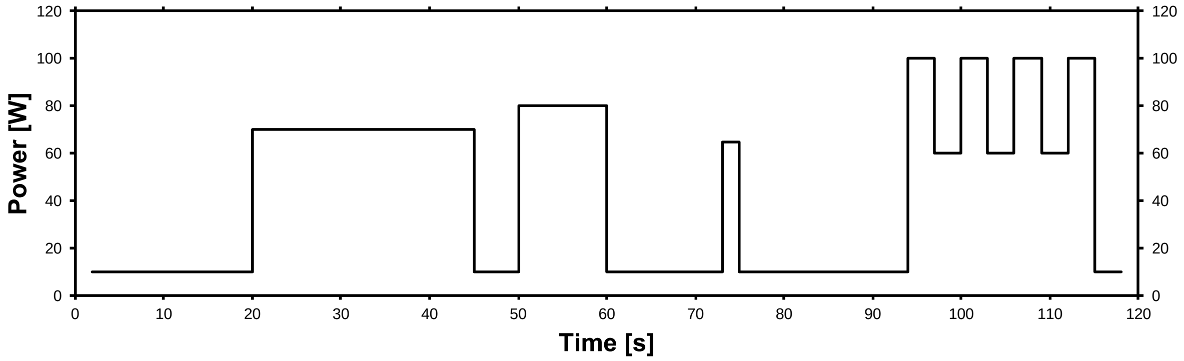

Figure 5.7 - Benchmark CPU power profile. [Adapted, [64]]

5.3.4. Real working conditions

A proof of concept test was carried through with the vertical prototype in order to address and evaluate its real working conditions operation, with an actual CPU mounted on a computer. Due to resources availability, the computer to which experimental data is recorded through the DAQ boards is the same to which the prototype cooling system was attached. This caused some issues to arise, since the overloading of the CPU, as will later be described affects its ability to save data to memory, causing some minor data loss. Nevertheless, the problem was overcome with repeated experiments. A system diagnostic and benchmarking software called AIDA64 Extreme was used to measure CPU core temperatures, the major variable of interest, as well as CPU load, fan speed and CPU consumed power. The software allowed access to its system diagnostic logs, which data was used to obtain the intended results. Furthermore, it contained a stress testing tool, used to obtain a transient thermal response after the sequenced activation and deactivation of its stress configuration which caused a 100% CPU load. A customized power profile such as the one from previous section would preferably be applied but current possibilities allowed for only two different loads to be used, namely full load (100% CPU load) and idle state (about 17% CPU load). A simple alternating sequence was then applied with a longer period of three minutes full load and three later separate full load periods of 20 seconds each. This sequence's thermal response was then obtained to compare the standard fan and heat sink technology included with the computer to the developed cooling system.

For these tests to be performed, the factory standard forced air convection solution must be carefully removed, allowing for the installation of the devised prototype. The bare surface of the CPU block to which the prototype's copper surface will be attached must first be cleaned to remove any thermal compound left and any other dust or dirty residues, followed by the application of fresh thermal compound for the surfaces contact. Then the prototype should be fixed with the appropriate threaded stud connections. Thermocouples may be disconnected from the prototype as they won't be used.

5.4. Uncertainty analysis

For the present work, three sources of uncertainty were identified, namely the following, as seen in table 3: (1) the pressure readings at the pressure transmitter and consecutive digital conversion in the respective DAQ board; (2) the temperature readings through the thermocouples and consecutive digital conversion in their respective DAQ board; (3) the heat load control, which implies voltage readings from the power source to the DAQ and, after the appropriate signal processing, digital to analog conversion for the power control signal to the Op-amp.

Technical data on the associated instruments provided the following accuracy figures, for the present experimental setup configuration:

Table 3 - Accuracy data for featured instruments.

(1) Pressure readings		**(2) Temperature readings**		**(3) Heat load control**	
Transmitter	DAQ	Thermocouple	DAQ	AI*	AO*
0,5%	7,73 mV	± 1K	± 0,1K	7,73 mV	7 mV

(*) AI – Analog input; AO – Analog output.

The uncertainties associated to the later presented boiling curves have thus one major source: the error associated with the thermocouples with which the surface junction temperature T_j and the liquid saturation temperature T_{sat} are obtained and used to compute the wall superheat. This error is estimated according to equation 5.18:

$$E\Delta T = \sqrt{ET_j^2 + ET_{sat}^2} \tag{5.18}$$

in which each temperature error is estimated according to the following equation 5.19 [65]:

$$ET = \sqrt{U^2 + (2\sigma)^2} \tag{5.19}$$

where U is the instrument uncertainty and σ the standard deviation of a certain measurement. For instance, for the surface with S = 100 µm, the T_{sat} standard deviation value for a heat load of 100 W was of σ = 0,72 K and the T_j standard deviation was of σ = 0,58 K, while the associated instrument uncertainty is $U = U_{thermocouple} + U_{DAQ} = \pm$ 1,1 K, so the uncertainty computes to $ET_{sat} = \sqrt{1{,}1^2 + (2 * 0{,}72)^2} = 1{,}82\ \mathrm{K}$ and $ET_j = 1{,}61\ \mathrm{K}$. This gives an estimated wall superheat error of $E\Delta T = \sqrt{1{,}82^2 + 1{,}61^2} = 2{,}43\ \mathrm{K}$. With a wall superheat measured value of $\Delta T = 33{,}5\ \mathrm{K}$ this corresponds to a relative error of 7,26%. Same reasoning and arithmetic could be applied to estimate the uncertainty associated with pressure readings and the output heat load the electronic control system applies to the thermosyphon system.

6. Results and discussion

The current chapter will present the results obtained through the different experimental conditions and equipment as well as a discussion on these data. It is mandatory to start by providing sufficient proof of experimental conditions conservation throughout one experiment, to validate the experimental setup and methodology as well as comparing results with the corresponding equivalent obtained in previous works. After this, conditions are met to present the main group of results, steady and transient state extensive characterizations of the two devised facilities: horizontally and vertically oriented systems, as well as comparing them, before discussing a “proof of concept” real working conditions application, meaning the vertical prototype was attached to a real operating microprocessor.

6.1. Experimental conditions validation

As previously mentioned in subsection 4.3.1, an early oversized facility was developed to validate the experimental conditions in which further efforts were undertaken. This facility, comprised of an oversized evaporator with 100 mm height and an excessive amount of cooling liquid, 40 ml, was tested to proof the functionality of the devised thermosyphon system. The results obtained with this “proof of concept” facility were then compared to results obtained in the previous work developed by Moura [2] for the purpose of validation, and both are shown in the following figure. The smooth surface was used in both sets of results:

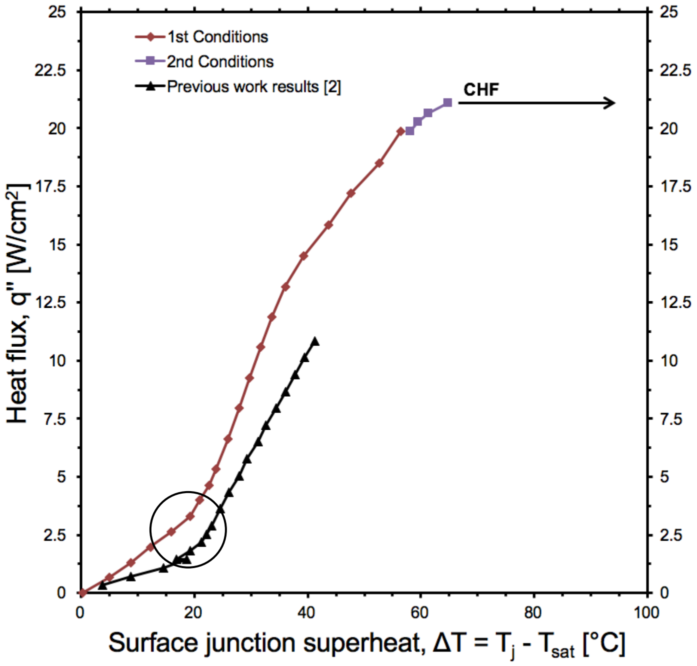

Figure 6.1 - Proof of concept experimental results validation, heat flux (boiling curve). [1st conditions: 0 to 150W; 2nd conditions: 150 to 180W]

The heat flux curve follows the trend of a typical boiling curve, as expected, though conditions are not the same, since pressure is not maintained constant as it is the case for benchmark boiling curves. Nevertheless, different boiling regimes can be distinguished in the figure, namely natural convection followed by nucleate pool boiling, with the transition as marked with a circle. In the results obtained in this experiment, two sets of results, identified as 1st conditions and 2nd conditions in the figure's caption, were distinguished due to a non-intentional sudden power break in between the obtaining of the two sets, thus leading to a fast temperature cool down, proceeded by a new rise in temperature. Due to high reversibility and reproducibility, both before and after the event curves smoothly match. This power break occurred at 150W. Around the 65°C superheat, 2,2x10^5 W/m^2 heat flux region, a critical heat flux condition was obtained and the system was automatically shut down. The following figure shows the evolution of pressure through the experiment, naturally increasing as the vapour phase quantity increases inside a closed chamber, as is the current case:

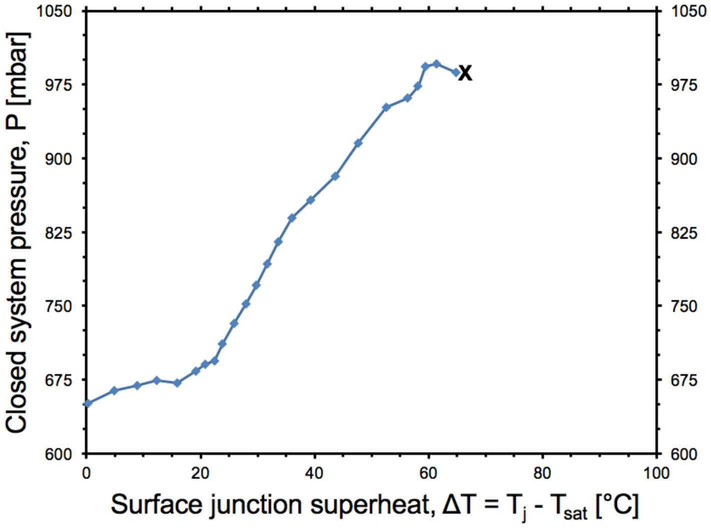

Figure 6.2 - Proof of concept experimental results validation, pressure.

6.2. Experimental facility: horizontal orientation

The current subchapter covers the outcomes of the study performed on the devised experimental facility, designed for the evaporator's heat exchange surface in a horizontal orientation, with the purpose of a full systematic study and characterization of each tested surface's heat exchange characteristics within the proposed cooling system. Limiting operational boundaries are defined according to their critical heat fluxes, CHF, and every surface performance is characterized through parameters as the heat transfer coefficient, h and the absolute thermal resistance, R. Initial remarks cover the challenges to overcome regarding the control of pressure throughout experiments.

Figure 6.3 in the next page features an image of the actual first version of the horizontal installation, assembled and operating according to the designs and methodologies introduced in the two previous chapters. The image also contains the external condensation liquid recovery system in the top right, the recovered liquid reservoir and the used syringe in the bottom and the computer used for data acquisition and analysis in the left.

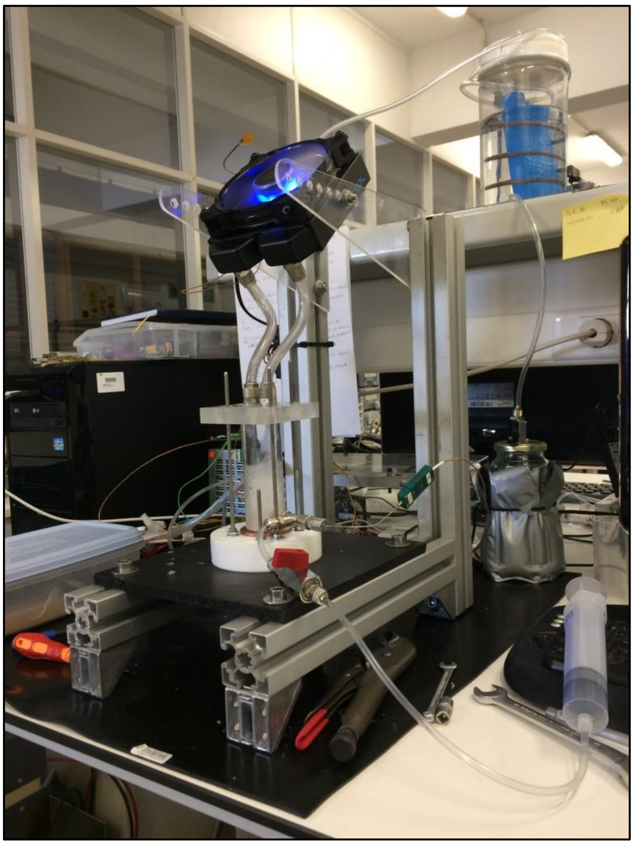

Figure 6.3 - Horizontal experimental installation in an operational state.

6.2.1. Pressure control

Typically, boiling curves used to assess the properties of heat transfer devices as the current one which uses pool boiling, are determined at constant pressure [51], [53]. Initial tests were performed to evaluate if the devised system could in any circumstance operate at constant pressure, to more easily compare its performance to other systems, and to obtain better representative steady state boiling curves. For such purpose, a PID pressure controller was implemented in the LabVIEW control routine previously mentioned. PID parameters were fine tuned to control the fan rotating speed, which defines the condensation rate, thus indirectly controlling the pressure inside the system’s closed chamber. For the devised system, pressure usually varies between 650 and 1200 mbar, proportionally to the imposed heat load. Higher pressures usually correspond to an imminent Critical heat flux situation. Lower pressure is not attainable due to saturation pressure at typical ambient temperatures of 19 to 22°C floating in the range of 620 to 670 mbar. PID control pressure values were subsequently set to 900, 950 and 1015 mbar, being the last value chosen as equivalent to ambient pressure, and for which test results are presented in figure 6.4 featured in the following page.

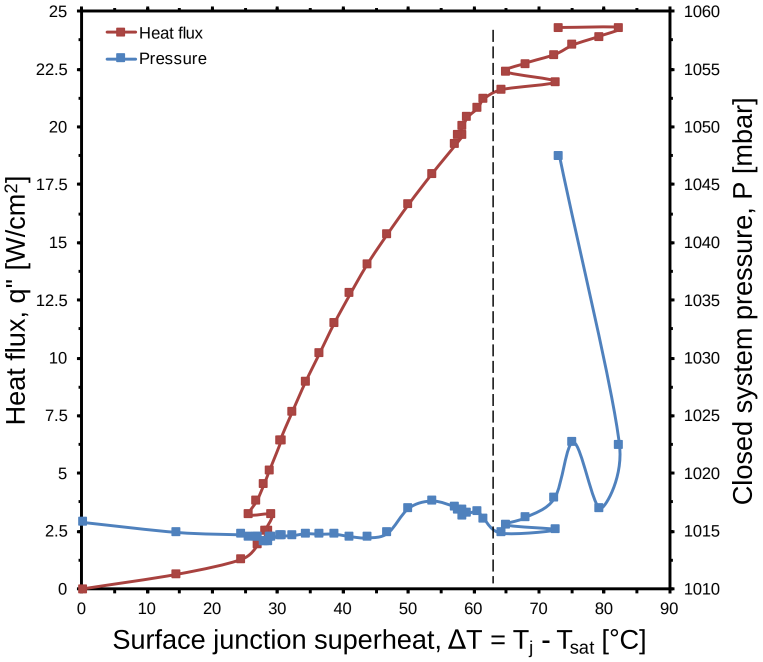

Figure 6.4 - Experimental results for PID controlled pressure set at 1015 mbar. The working fluid is HFE-7000.

As can be seen in the figure, pressure was successfully kept constant as the surface junction superheat was kept below 60°C and the heat flux was below $2x10^5$ W/m^2. After this it was not possible to control the pressure any further, as the required cooled liquid flow rate was not sufficient with the fan working at its maximum speed, leading to a most certain pressure increase, as it is possible to observe in the figure. To each heat flux curve point a pressure point corresponds, for the same superheat value. This uncontrolled region transition is denoted by the vertical line in the figure. Logically, the same issue occurred even earlier in the previous two experiments with 900 and 950 mbar set pressure. A solution to this problem could be to increase the set pressure even further, alongside a proper PID parameters tuning, but, on the other hand, a different problem derives from that approach in earlier low heat loads. It then takes a long time for the system to get to the set pressure, with the fan not rotating at all, which affects the performance of the system at low heat loads. It might not even reach the desired pressure at all, if the onset of boiling doesn't occur. Hence, it was then decided not to follow this approach of obtaining the boiling curves under controlled constant pressure. Such procedure would be interesting in scientific terms but not at a practical point of view, considering the product development, since the CPU cooling system is unlikely to work under controlled constant pressure in real operating conditions. So, the pressure throughout all further experiments is self-determined by the system dynamics, and is always the lowest for each heat load, as the fan is always set to its maximum rotating speed. Pressure ranges from around 650 to 1200 mbar as previously stated.

6.2.2. Effect of surface micro-structures on the cooling behaviour: steady-state analysis

In this section, the effect of the surfaces' cavity distance parameter, S, over the cooling behaviour of the devised cooling system is studied, being the optimization of this parameter its major objective. All the presented results were obtained with the system operating at steady-state, with each data point requiring for a stabilization period before values were registered. Each curve was obtained as the average of 5 experiments. Figure 6.5 displays the boiling curves up to the near critical heat flux region for each surface previously introduced and tested on the horizontal setup, with the smooth surface as a reference for the remaining six surfaces.

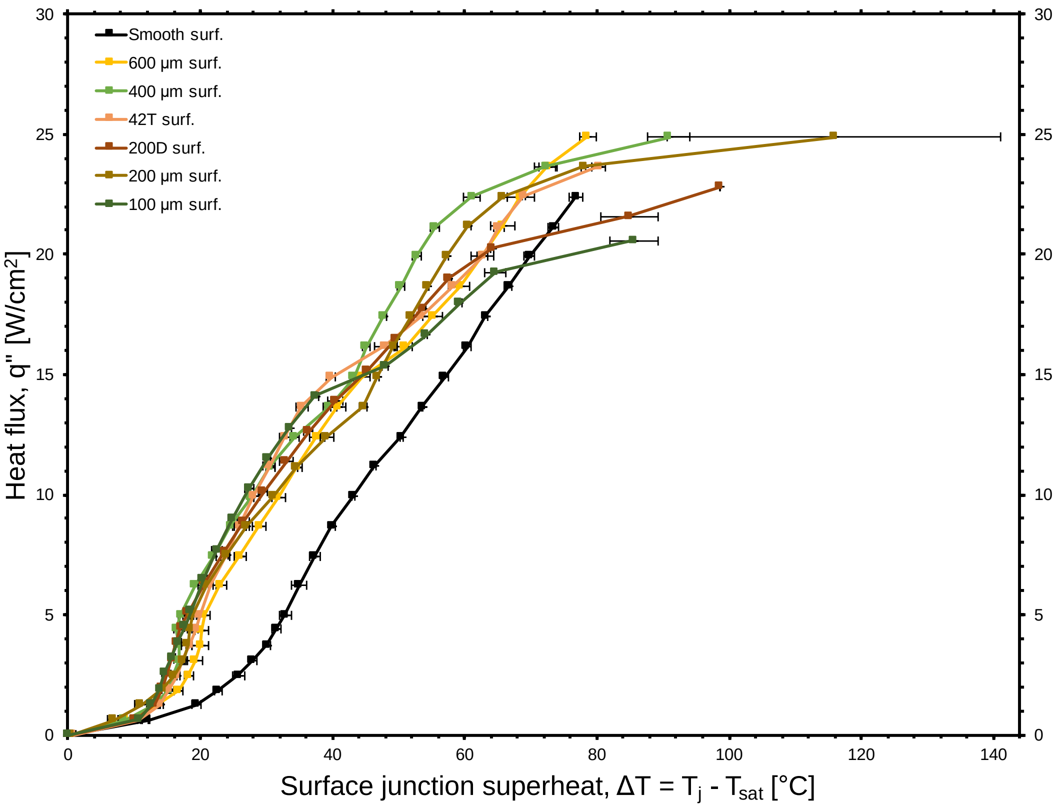

Figure 6.5 - Adapted boiling curves for all surfaces tested with HFE-7000 as working fluid. [Horizonal]

It is important to note that the presented curves should not technically be addressed with the term boiling curve, they are just representative heat flux against surface superheat curves, but not obtained under constant pressure conditions as should be in the case of formal boiling curves, as obtained by Nukiyama [51]. Also, it is worth reminding that the superheat is taken using the junction temperature, which is more representative in terms of the application in study than the surface temperature. Hence, these curves are named as adapted boiling curves. Every curve was taken up to its near critical heat flux values of heat flux, sometimes having achieved this condition, as clearly was the case for the 200 µm surface curve, displaying large standard deviation values for its higher temperature point, due to different temperature values having been observed during CHF, in successive experiments. Error bars represent the surface junction temperature standard deviation from repeated experiments. Heat flux was dictated by means of the devised power control system, so the values were kept the same in successive experiments, for each increasing power step level. It's very clear how the presence of surface structures alters the heat transfer dynamics, improving the dissipation of heat from the hot surface to the liquid, thus reducing the superheat temperature for every structured surface as compared to the smooth surface, for any heat flux value, up to the region of 2x10^5 W/m^2. From this heat flux value on, high uncertainty does not hold the previous statement. Reasons for this highly disperse behaviour in higher heat fluxes will be further discussed. Having stated there is a clear influence of surface structuration on the cooling behaviour, it's not so easy to conclude how the surface parameter, S influences results, from a straight analysis of the previous figure.

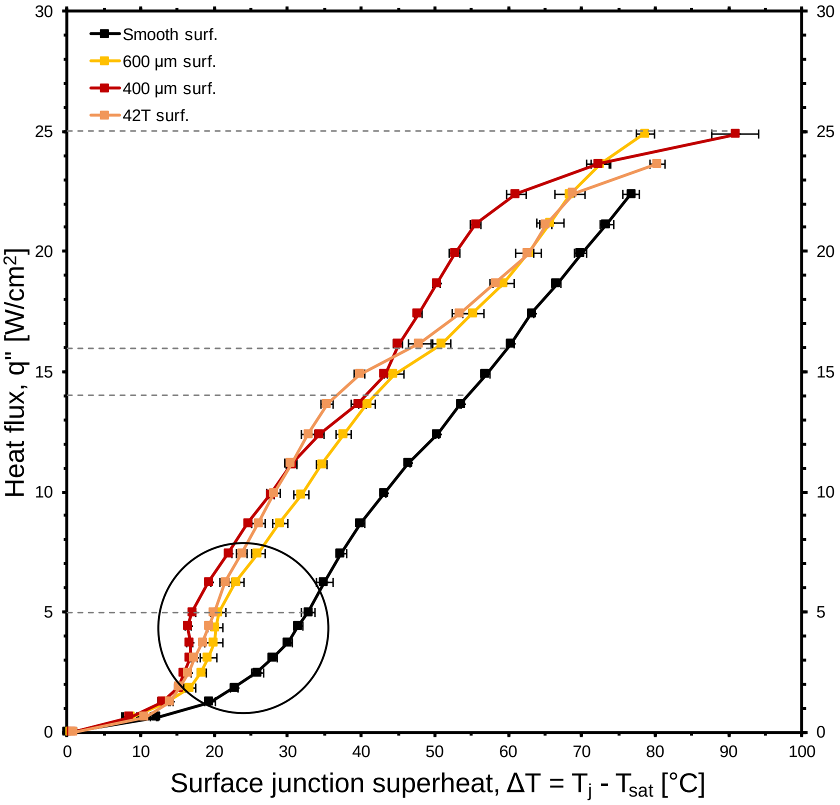

Figure 6.6 - Adapted boiling curves for surfaces 42T, 400, 600 and Smooth, with HFE-7000 as working fluid. [Horizontal]

Figure 6.6 displays the same results as the previous figure, although with less surface curves, selected for representability and ease of analysis. The circle denotes the regime transition from natural convection to nucleate pool boiling. Horizontal dashed lines denote the two heat flux ranges of interest for the present study, 0,5 to 1,4x10^5 W/m^2 and 1,6 to 2,5x10^5 W/m^2 as will later be addressed. Focusing in heat fluxes ranging from 0,5 to 1,4x10^5 W/m^2, where a nucleate boiling regime can be observed, a general trend can be observed for the boiling on surfaces with lower values of the cavity distance parameters S: the same values of the heat flux are attained for lower values of surface junction superheat, so the boiling heat transfer is improved for these surfaces. This is clear comparing the surfaces with S = 600 µm and S = 400 µm with the smooth surface. In this figure, the curve obtained with the additional surface 42T displays a mixed behaviour starting similarly to the curve obtained with surface S = 600 µm, at lower heat fluxes, but then gradually improving its cooling performance over increasing heat flux values. This mixed behaviour can be explained due to its mixed pattern of two regions with different cavity distances, 400 and 200 µm, with each region having a different contribution to the boiling process during different phases of the experiment. Transition from natural convection to nucleate regime, identified by the sudden increase in the slope of the curve, starts at a heat flux value of around 3x10^4 W/m^2 for each structured surface, as observed in figure 6.5, whereas for the smooth surface it starts for higher heat flux values, around 6x10^4 W/m^2, and higher surface junction superheat, suggesting the presence of cavities promotes bubble nucleation and an earlier onset of boiling, leading to improved cooling performance. As heat flux values increase over values of 1,4x10^5 W/m^2 surface superheat temperatures seem to behave in a quite disperse way, with low correlation to any physical phenomenon and with any apparent trends. This is due to flow issues arising from the reflux condenser setup with counterflow previously mentioned in section 4.3.2. This setup implies that both downward liquid and upward moving vapour phases flow through the same two pipes connecting the condenser to the evaporator. At higher heat fluxes, mass flow rates increase as more liquid evaporates in contact with the hot surface. At a certain point these two opposing flows block each other's passage through the pipes, which would need a higher diameter to allow both phases to counterflow efficiently. This "choking" effect happens cyclically, since pressure in the evaporator rapidly increases while the pipes are blocked and vapour phase continues to generate, eventually leading to an overcome of the vapour phase pushing liquid back into the condenser. This causes large temperature fluctuations and sets an operating limit to the thermosyphon, being the major cause for highly uncertain values at high heat fluxes. It may also dangerously cause surface dry-out and lead to unintended temperature peaks, as the supply of condensed saturated liquid is cut off in the choking process. It is then concluded the option to design the horizontal facility in a reflux condenser setup, with such undersized connecting pipes, did not contribute to the quality of results obtained, being part of a strategy to study different designs and achieve improvements in the CPU cooling product development point of view. Previous studies on reflux condenser setups [22], [66], [67], accounted for the same temperature fluctuation issues, reporting the same vapour-liquid pipe flow behaviour, arriving at similar conclusions regarding the cause for these fluctuations and defining an operating limit in a closed two-phase thermosyphon with a uniform pipe.

Figure 6.7 in the following page shows some frames taken from a Phantom high-speed camera film, during the emergence of critical heat flux, obtained after a heat load of 200W was applied, with surface 600. The second frame on the top right in particular clearly shows the oscillatory vapour film in the bottom, near the surface, while big bubble formations is also witnessed in the following frames. No trend was observed regarding the heat flux values for which CHF occurred, with changing microstructure cavity distance parameter, S. Perhaps due to the reported flow issues brought by the reflux condenser setup, CHF would occur at any value above 150W and under 220W, without any correlation to S.

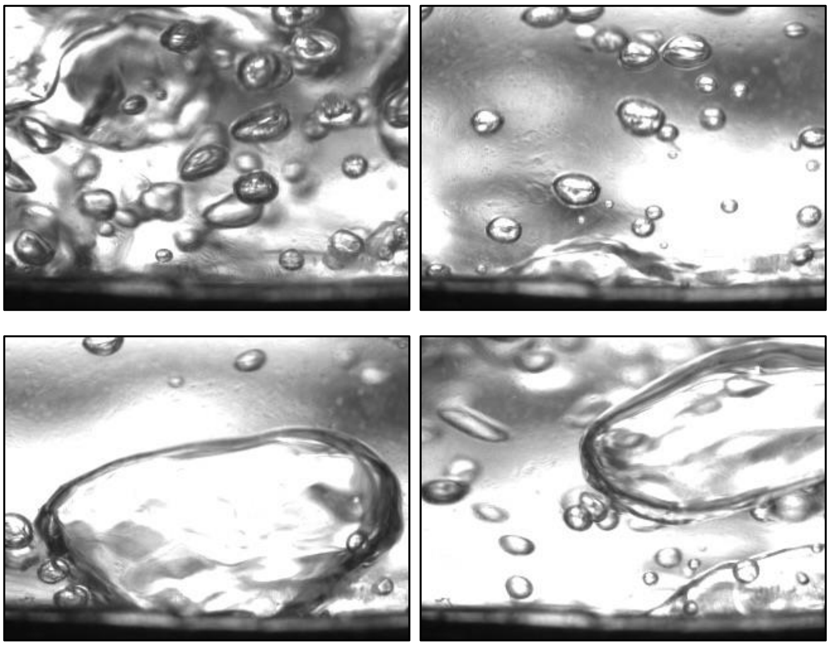

Figure 6.7 - High-speed camera time consecutive frames show near-surface transition to CHF, with big bubbles formation and a vapour film on the bottom. Surface 600 at 200W was used.

Figure 6.8 plots the average heat transfer coefficient ratios of each surface to the average heat transfer coefficient of the smooth surface, against their respective cavity distance surface parameter, S.

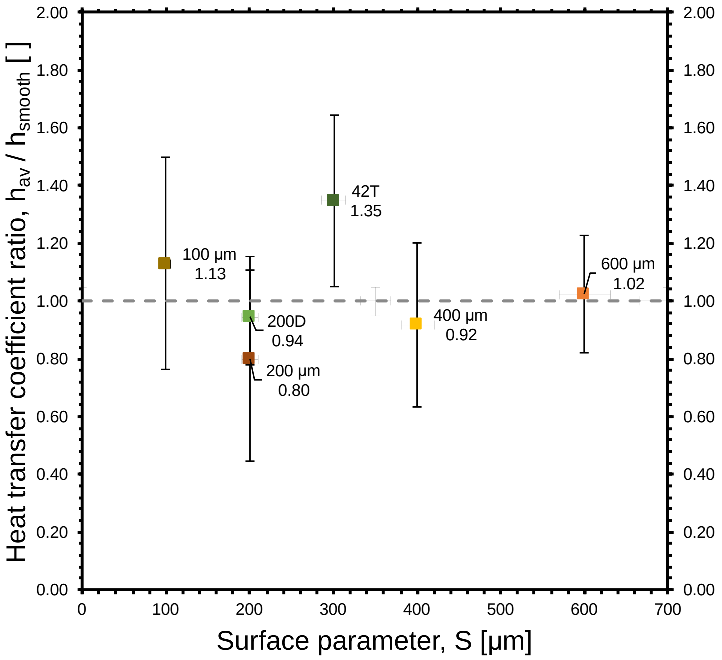

Figure 6.8 - Structured to smooth surface average h ratios per surface parameter, S. [Horizontal]

Average heat transfer coefficients were computed over the first heat flux range of interest, 0,5 - 1,4x10^5 W/m^2. Error bars symbolize the relative standard deviation obtained in the average calculation. Heat transfer coefficient values were computed from previous boiling curve values recurring to a finite difference method, being the slope of the boiling curve at each measured point. Since surface 42T has a two-region structuration, with S = 400 and 200 µm each, the author opted to attribute an average equivalent surface parameter of S = 300 μm to plot this surface's values, for ease of representation. This graph enables an easy interpretation of data referring to each surface's h and their performance, and is used as a means of comparison between the various surfaces used in this study. There is not an apparent trend for h improvement with the decrease of the cavity distance parameter, which doesn't match previous observations by Moita et al. [68], Moura et al. [17], and Teodori et al. [3]. Many possible causes for this can be introduced. First, the used experimental facility design was substantially different than previous setups, with the mentioned reflux condenser, among other different components, which affects the behaviour of the system. Secondly, an additional physical mechanism might negatively impact heat transfer. Moita et al. [68] and Valente et al. [69] refer that the shortening of distance between nucleation sites increases interaction mechanisms between departing bubbles, leading to coalescence of bubbles, which in turn negatively affects boiling performance. Hence, the distance between cavities must be fine-tuned for the best balance between the positive effect of promoting the activation of nucleation sites and the negative effect of excessive interaction between them. Nevertheless, surface 42T shows the best performing results, suggesting the combination of two differently patterned structure regions could take the best of both worlds, benefiting of high nucleation sites activation on the one hand, through the 200 μm pattern, and avoiding coalescence with the 400 μm pattern on the other hand.

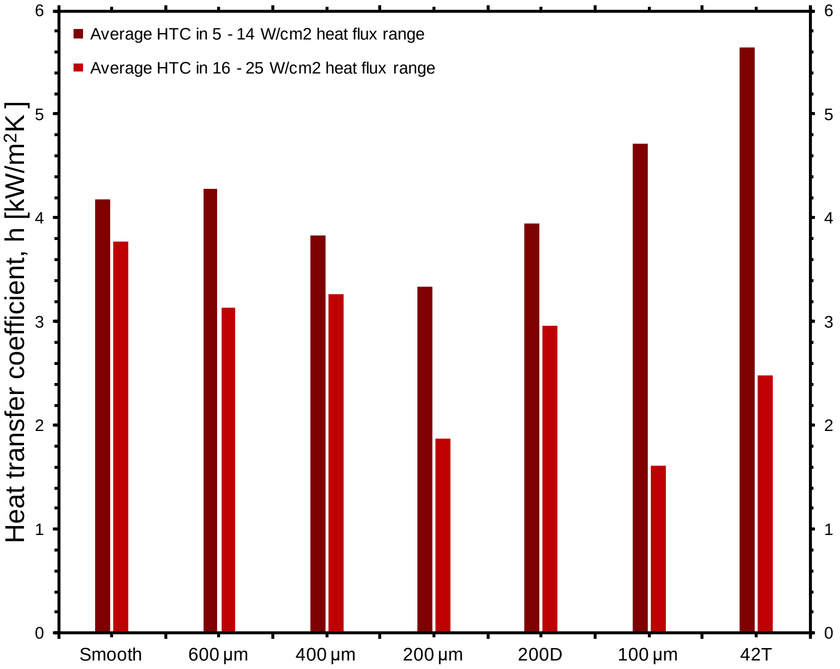

Figure 6.9 - Average h over two distinct wall superheat regions. [Horizontal]

Figure 6.9 shows the average heat transfer coefficients over the two identified heat flux regions of interest, 0,5 to 1,4x10^5 W/m^2 and 1,6 to 2,5x10^5 W/m^2, as previously introduced, for each surface. The first and more relevant region, corresponding to the nucleate boiling regime, is represented in dark red, showing a noticeable progression from values ranging from 4 to 6 kW/m^2K. The lighter red colour bars, corresponding to the second boiling regime and characterized by strong temperature fluctuations and obstructed flow, display a worse h performance for every surface, as the boiling process is negatively affected, as previously stated. To better understand the heat transfer coefficient trend throughout the nucleate boiling regime, figure 6.10 plots this parameter against heat flux values obtained during the experiments, a common procedure for works in this field [41]. As can be seen, the general trend is for the h to reduce with increasing heat flux, over the given range of superior experimental relevance.

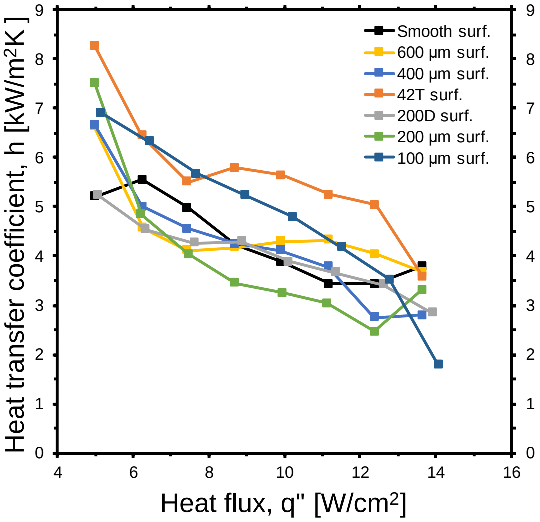

Figure 6.10 - Nucleate boiling regime h results. [Horizontal]

Closing the current subsection, the following figure 6.11 shows the average absolute thermal resistance, R, for each surface plotted against the heat load power deployed at each steady-state power level throughout all the experiments.

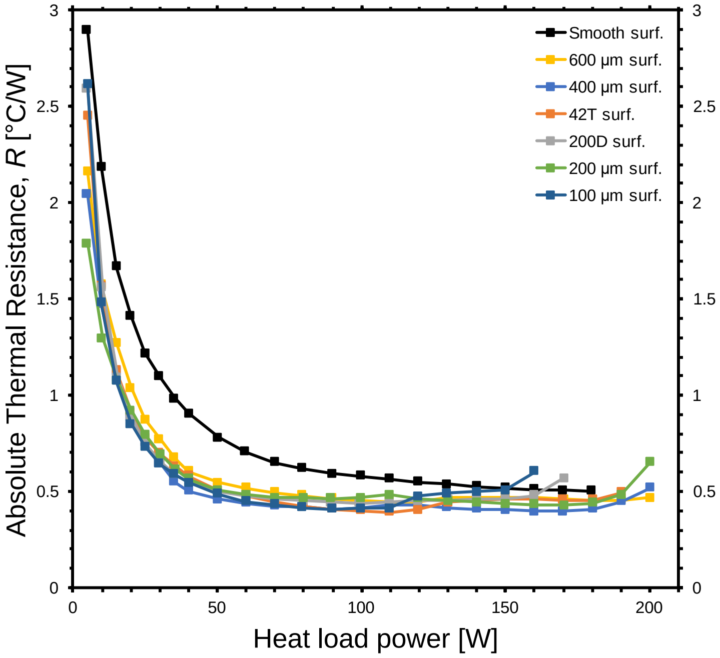

Figure 6.11 - Absolute thermal resistance, R, for each surface. [Horizontal]

The absolute thermal resistance is computed from junction to ambient temperature. The smooth temperature shows the highest resistance, as expected, with surfaces 200, 100, 400 and 42T successively performing best regarding lowest resistance. It is of the best interest regarding the development of an optimized CPU cooling product to reduce this parameter to the least possible values, reducing layers of thermal resistance from the heat source, to the heat sink, or, in other words, from the CPU to the condenser where heat is dissipated to the environment. Finally, it can be concluded that, for the specific context of the devised horizontal test facility, the outcome of the cavity distance optimization process, with regards to cooling behaviour, is the option to choose surface 42T, and being this one a newly introduced approach to surface design, this outcome strongly suggests that further research studies should be developed to evaluate additional possible multi-pattern surface structure designs.

6.3. Experimental facility: vertical orientation

The current subchapter covers the results obtained on the devised experimental facility, designed for the evaporator's heat exchange surface in a vertical orientation, with the purpose of a CPU cooling oriented product optimization. A full systematic study and characterization of each tested surface's heat exchange characteristics was performed, within the proposed optimized cooling system. Like in previous section 6.2.2, limiting operational boundaries are defined according to the surfaces' critical heat fluxes, and every surface performance is characterized by the heat transfer coefficient. Regarding the facility's fill charge, it is not subject to further study as there is only a very little range of available levels, due to design constraints. Only in this narrow liquid level height range the system, due to its compact design (for fitting inside a computer body), can fully submerge the evaporator's boiling surface and not flood the condenser body simultaneously.

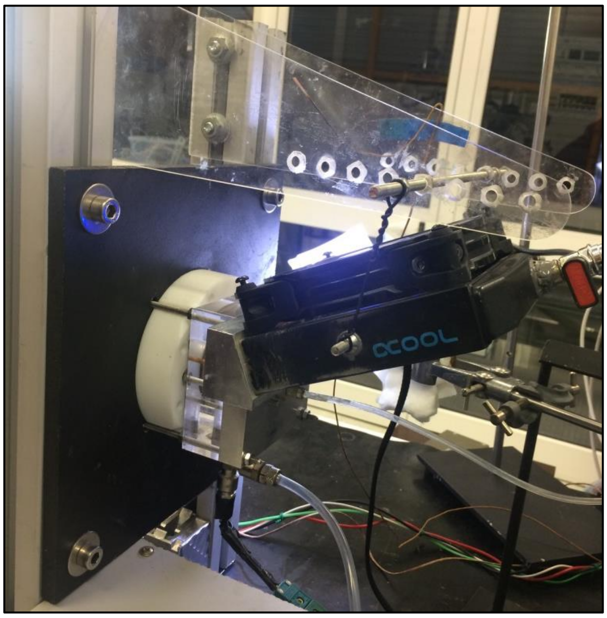

Figure 6.12 - Vertical experimental installation in an operational state.

6.3.1. Effect of surface micro-structures on the cooling behaviour: steady-state analysis

As in previous section 6.1.2, this section covers the study of the influence of the cavity distance parameter, S, over the cooling behaviour of the developed system, this time in its vertically oriented surfaces lay-out. The optimization of the S parameter for this setup is the main objective. All results were obtained with the system operating at steady-state, with each data point requiring for a different stabilization period before values were registered. Every curve results of a sequence of the average data points obtained for 3 separate experiments with each surface. Figure 6.13 displays the boiling curves up to the near critical heat flux region for each surface tested on this vertical orientation purpose-aimed prototype, consisting of all data acquired for its characterization. Further results are derived from these:

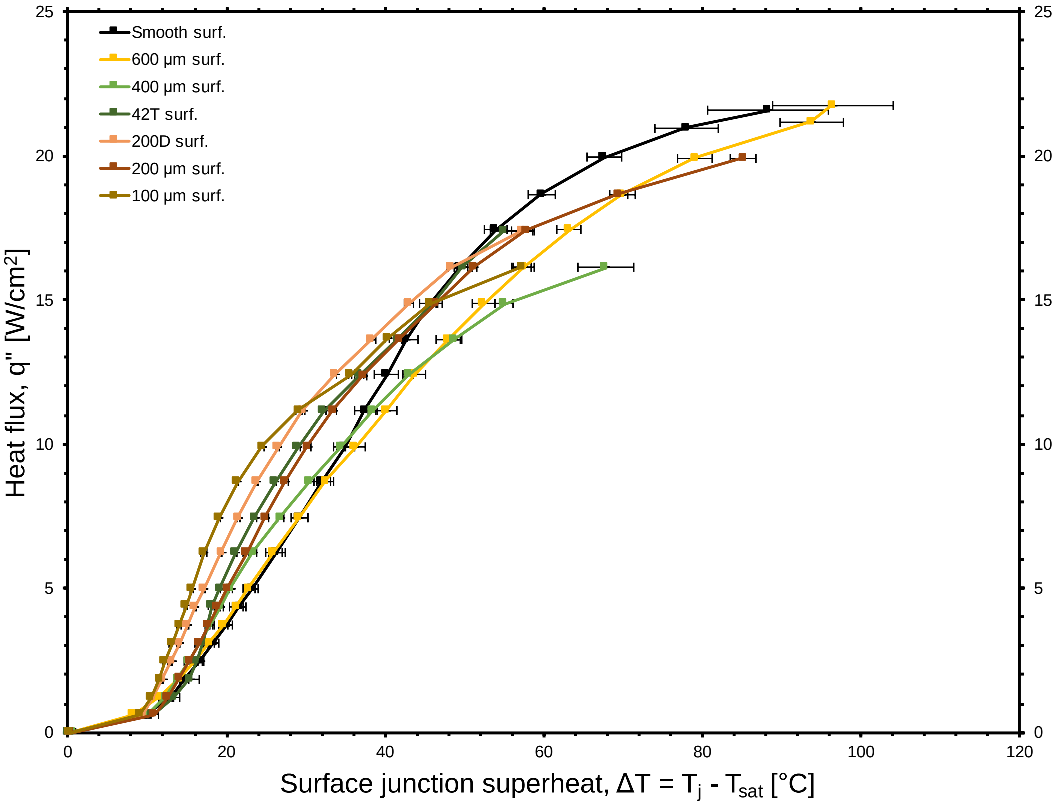

Figure 6.13 - Adapted boiling curves for all tested surfaces. [Vertical]

This time, against what was previously discussed for the horizontal experimental campaign, a nucleate boiling regime was reached up to the emergence of critical heat flux, for every surface, hence leading to the conclusion there were no flow impeding factors influencing the results. In fact, this was attained due to the integrated design previously presented for the current facility. The existence of a one-chamber fully integrated evaporator and condenser body allows for unobstructed flow from one to the other, nulling any pressure drops or differences. Again, the presented curves should not technically be addressed with the term boiling curve, they are just representative heat flux against surface superheat curves, with pressure varying according to the heat and fluid dynamics within the system. Error bars represent the surface junction temperature standard deviation from repeated experiments. These bars tend to increase as heat flux rises, initially due to increasing temperature fluctuations and perturbed flow, and finally due to the emergence of CHF. Heat load applied to the system was controlled so no deviation is associated with heat flux values, with a constant heat exchange area, hence the absence of vertical error bars. One can observe how the cavity distance can affect the boiling behaviour, with an overall trend for cooling improvement as the parameter S is reduced, at least for initial heat flux values, up to $8x10^4$ W/m^2. Opposite from the observed in previous horizontal installation, the smooth surface does not stand far from the structured surfaces regarding its superheat values, with no temperature gap from this surface to the others, as was the case of the horizontal orientation, and instead a smooth decrease in temperatures is observed. In fact, after $8x10^4$ W/m^2, every other structured surface ends up surpassing the smooth one's superheat temperatures. Figure 6.14 resumes previous figure to a selection of relevant surfaces, for ease of representation and analysis:

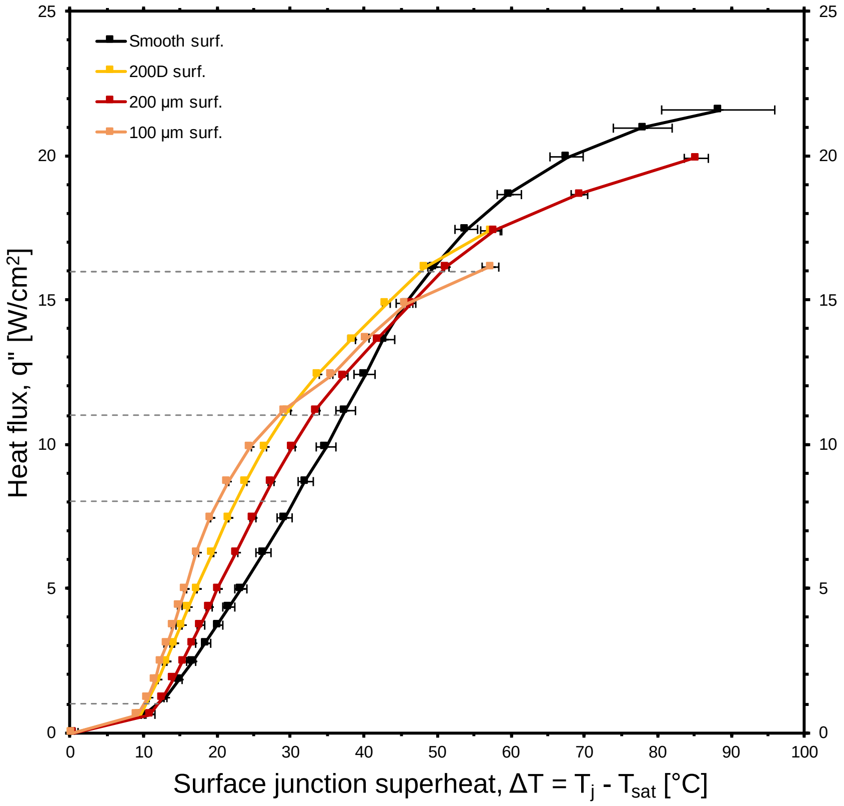

Figure 6.14 - Adapted boiling curves for surfaces 42T, 400, 600 and Smooth. [Vertical]

This time, selected heat flux ranges of interest are 1 to 8x10^4 W/m^2 and 1,1 to 1,6x10^5 W/m^2, as denoted by the dashed lines. First range accounts for a nucleate boiling regime with constant heat transfer coefficient (linear curve) and with divergent superheats for each surface. Second range is still under nucleate boiling regime, but in turn presents an irregular h behaviour (considering the slope of the curves) and converging superheats, with all curves crossing around 1,5x10^5 W/m^2. There is a cooling behaviour inflection point around 10^5 W/m^2. It is of great interest, in the CPU cooling product development point of view, to pick the surface which minimizes surface junction superheat, and up to this point either surface 100, 200D or Smooth could be strong candidates for further studies, for different heat load regimes. Nevertheless, other factors must be considered, such as the heat transfer coefficients. Hence, following the procedure addressed in the previous subsection, Figure 6.15 plots the average heat transfer coefficient ratios of each surface to the average heat transfer coefficient of the smooth surface, against their respective cavity distance surface parameter, S. Average heat transfer coefficients were computed over the first heat flux range of interest, 1 - 8x10^4 W/m^2. Error bars symbolize the relative standard deviation obtained in the average calculation. Same calculating methods and reasoning for surface 42T display as if it were S = 300 µm are applied, as in equivalent figure 6.8 of previous subsection 6.2.2.

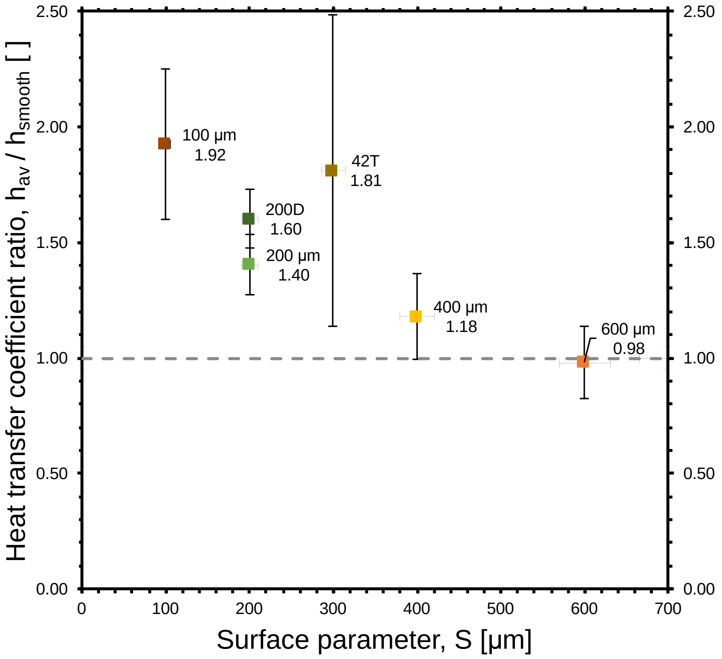

Figure 6.15 - Structured to smooth surface average *h* ratios per surface parameter, *S*. [Vertical]

As opposed to the previous horizontal orientation analysis, the vertical orientation enabled a notorious improvement in the *h* of structured surfaces, and this time the predicted correlation between a reducing *S* parameter and an increasing *h* ratio is achieved, matching previous observations by Moita et al. [68] and Moura et al. [17]. From a straight analysis, surfaces 100 and 42T seem to be the best performing in terms of *h* improvement. The wider and deeper cavities of surface 200D also enabled for an additional performance benefit compared to surface 200. Only surface 600 achieved a smaller *h* than the smooth reference. At this point, it is important to address the causes for the cooling behaviour inflection point around 10^5 W/m^2, which justifies the division in two different heat flux ranges, both at nucleate boiling heat transfer regime. This behaviour is caused by bubble's lateral coalescence. As heat flux increases and bubble nucleation and departure rate increase, buoyancy forces responsible for the departure pull the bubbles parallel to the surface, causing some of these to coalesce, creating bigger bubbles, therefore, higher thermal resistance due to the vapour presence. This causes surface temperature to increase and, ultimately, to reach CHF earlier (i.e. at lower heat fluxes) than if it were in a horizontal position. The smooth surface, which does not feature cavities, is not affected by the coalescence of bubbles in its surface either, explaining as well why every other curve achieves CHF at a higher surface junction superheat than the smooth one, relative to the same heat flux value. Figure 6.17 shows how the *h* is significantly lower for the second range of interest, 1,1 - 1,6x10^5 W/m^2, for every surface, except the smooth.

The following set of images comprises high speed photographs taken during a typical experimental procedure with the smooth surface, starting from a quiescent state, progressively increasing the applied heat load up to 130 W, through the observable heat exchange copper surface, which is initially fully submerged. Progressive increase of departed bubbles frequency can be witnessed, as well as an increasingly turbulent flow inside the chamber. The dark unfocused body in the top right corner of each picture is the beginning of the condenser, from which return condensed liquid flows into the evaporating region. Liquid level height initially starts to increase as more bubbles find its way to the liquid-vapour interface, but gradually decreases at higher heat fluxes due to the gradually less amount of available liquid.

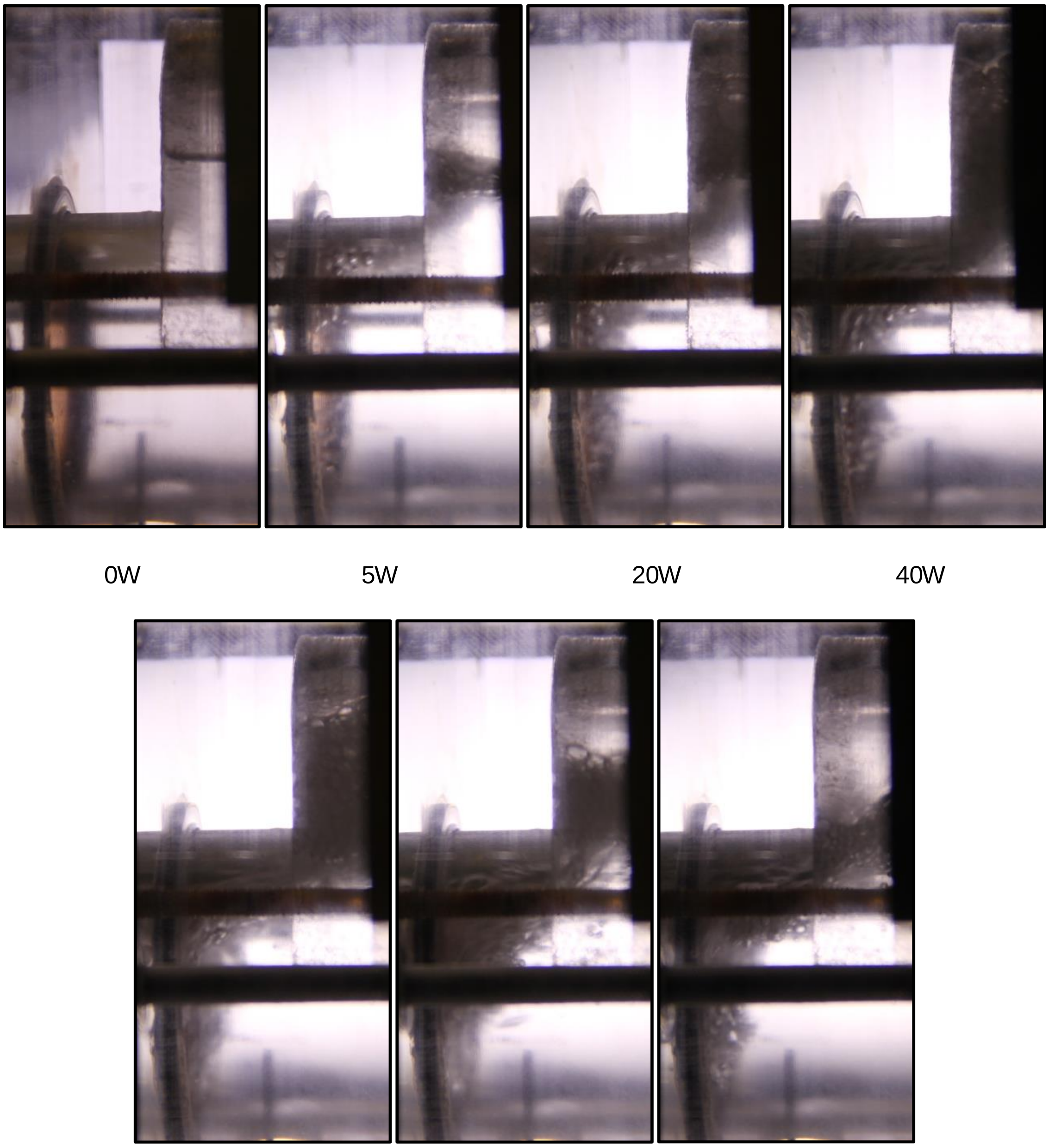

0W 5W 20W 40W

70W 100W 130W

Figure 6.16 - Boiling flow high-speed photographs within evaporating chamber, increasing power.

Inspecting the bubbles flow and how the high heat flux flow seems to generate an inclined free liquid-vapour interface, avoiding the flow resistance caused by the sharp inner edge (as seen in the picture centre), this could suggest a design improvement to round those edges, adding an inner fillet feature, or a chamfer for lower production costs.

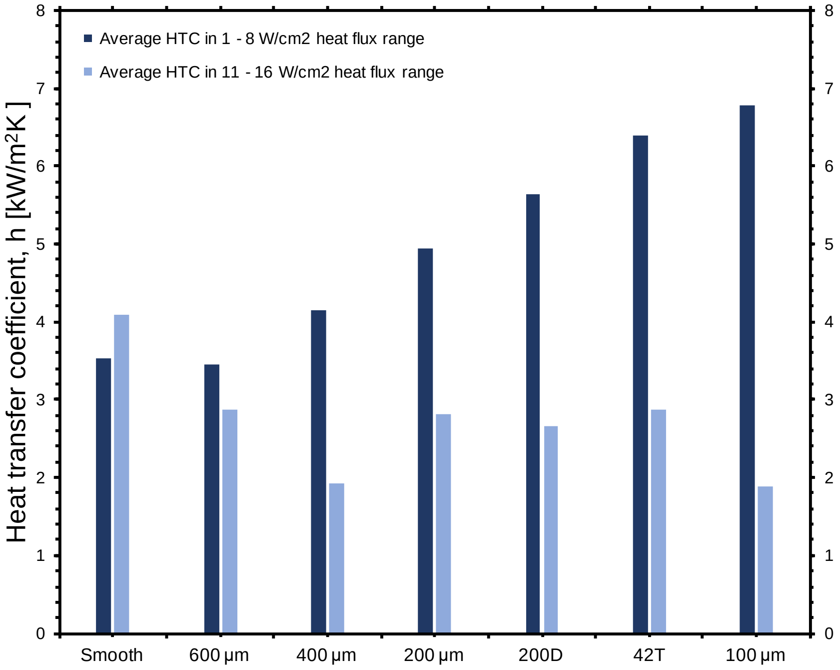

Figure 6.17 - Average h over two distinct wall superheat regions. [Vertical]

Contrary to the previous coalescence disadvantage featured by the vertical oriented surface, benefits notoriously arise at lower heat flux values (1 to 8x10^4 W/m^2), mainly due to the compulsory thermal boundary release effect caused by bubbles rising along the boundary layer. With the thermal boundary layer being disrupted by the departing bubble, the rate of heat removal is proportional to various factors such as the number of nucleation sites and the bubble departure frequency and diameter, determined by the cavity distance and geometry, explaining how different surfaces behave differently. In a simplistic analysis, smaller S parameter means more nucleation sites, which means more departing bubbles, leading to more thermal layer disruption and finally a cooler surface junction (or CPU core).

Figure 6.18 shows the variation of the instantaneous heat transfer coefficient computed for each data point, plotted against the successive heat flux values through the experiments. Against the approach previously sought for the horizontal case, this figure displays all heat flux values, enabling an overall overview of the h behaviour. Starting from the convective flow heat transfer regime, h rapidly increases up to its maximum point, associated with the occurrence of the onset of boiling. Smooth surface shows a later onset, explaining why its h values increase until higher heat fluxes. After the onset of boiling, during the developing of nucleate boiling regime, the h tends to slowly decrease, due to multiple heat transfer and fluid dynamics mechanisms, such as the increasing coalescence of bubbles at the surface or the limited return supply of quenching liquid provided by the condenser at maximum operational mode, with its fan rotating at maximum speed. Liquid level height also plays a role, since, as it lowers throughout an experiment due to the increasing total evaporated vapour mass and decreasing liquid mass, less area of the surface is covered in liquid, thus not fully utilizing the available heat transfer potential, and leading to a junction temperature increase. The apparent increase of h for surface 600 in the very last data point is due to experimental error associated with uncertain temperature observation at the imminence of critical heat flux.

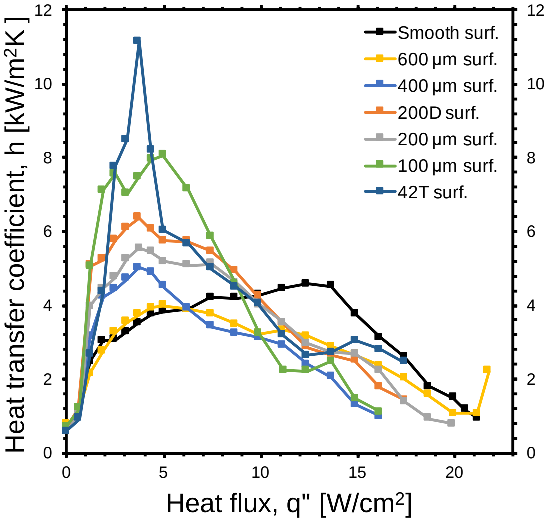

Figure 6.18 - Nucleate boiling regime h results. [Vertical]

To close this subsection, final figure 6.19 shows the absolute thermal resistance, R, of each surface, for all imposed heat loads. Surface 100 again displays the lowest resistance through its entire heat load span, followed by surface 200D. Thermal resistance tends to increase by the very end of each curve, as the fully developed boiling regime got close to CHF, due the reported issue with vertical bubble coalescence.

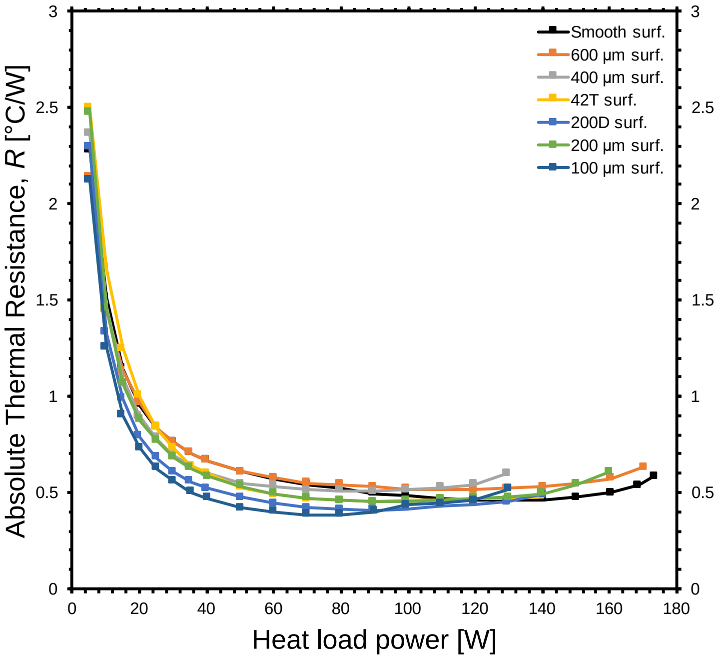

Figure 6.19 - Absolute thermal resistance, R, for each surface. [Vertical]

To conclude, the final remark is that the most relevant or best performing surface for the vertical case is surface 100, with S = 100 µm, which suggests further studies in vertical orientation should be carried through with smaller cavity distances.

6.3.2. Cooling behaviour under transient analysis: benchmark heat dissipation profile

The current subsection covers the study of the results obtained in a transient state analysis of three selected surfaces. Initially, four different power steps, 20 W, 60 W, 100 W and 140 W, were applied from ambient temperature and at quiescent system state, with an equilibrium of saturated liquid and vapour. Afterwards, from the same quiescent state, the benchmark CPU load profile adapted from Isci and Martonosi [64], introduced in section 5.3.3, was applied to the system. Obtained results are reported in the two next figures, where for figure 6.20 the power step plots are just representative drawings and in figure 6.21 the power profile values are plotted in the graph.

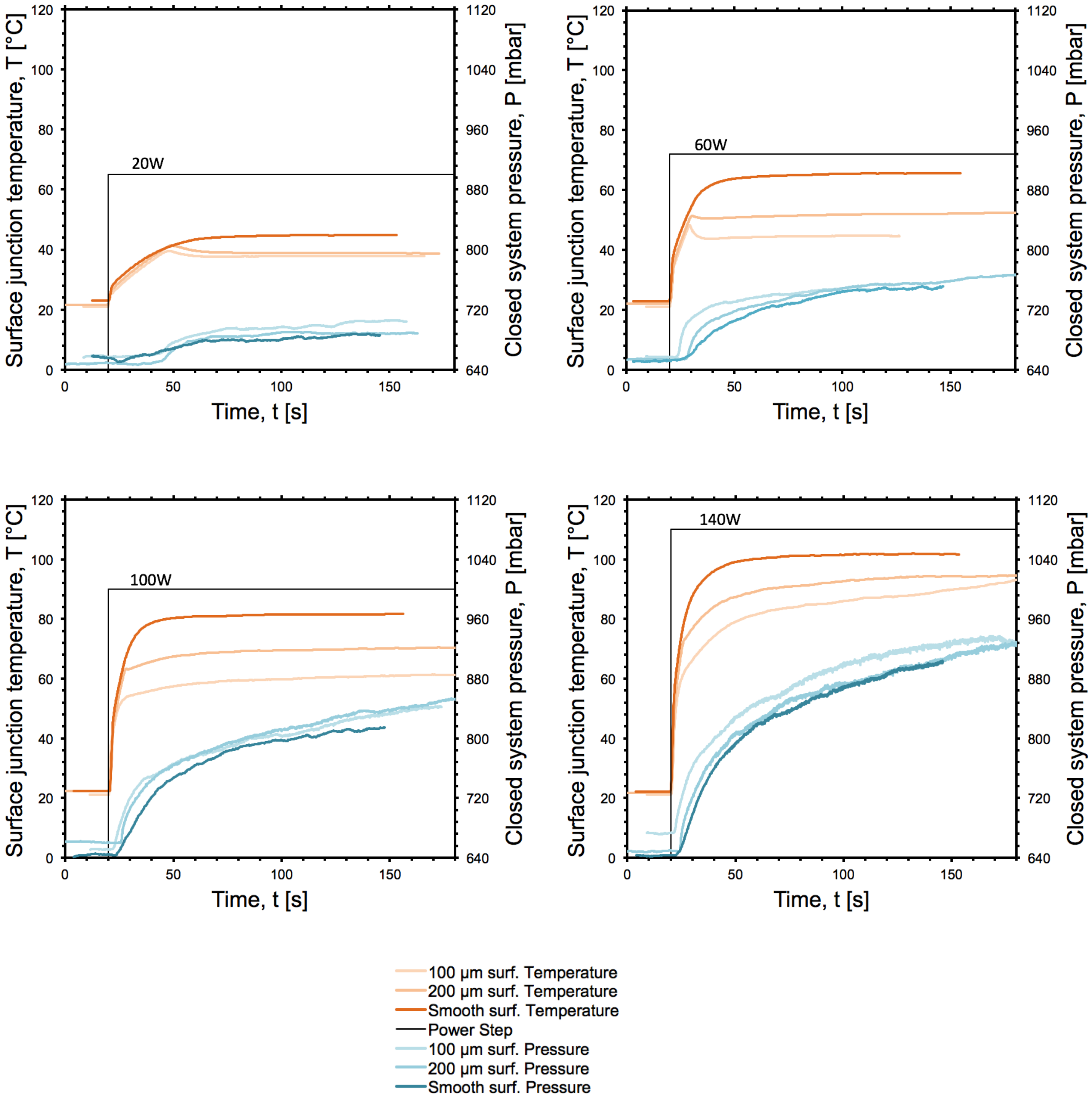

Figure 6.20 - Thermal and pressure response to heat load power steps, for 3 selected surfaces.

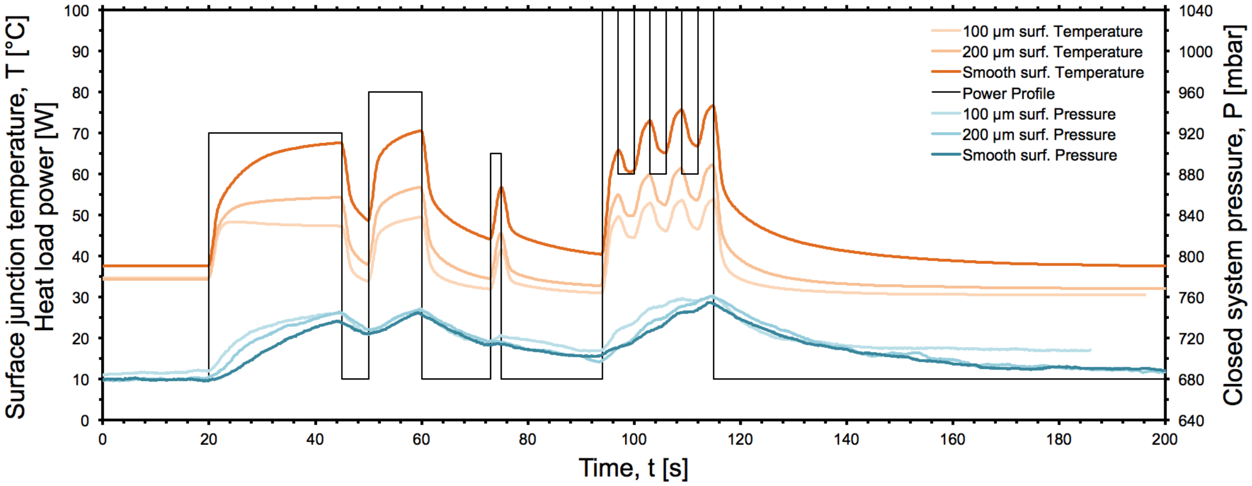

Figure 6.21 - Thermal and pressure response to an adapted power profile, for 3 selected surfaces.

Selected surfaces were 100, 200 and Smooth, being the first the best performing surface on previous section, 200 for comparison and inspection of cavity distance influence, and Smooth as a reference. The present study was carried through with the vertical oriented facility, with the purpose of evaluating the transient system response to heat inputs and to infer on main design parameters for the CPU cooling product to develop. In fact, it is of major interest to know the maximum temperature achieved throughout a standard benchmark cycle like the one applied, should this temperature be below recommended values for CPU reliability and performance. Maximum allowed temperatures stand between 65 and 75°C for most commercial applications in standard clock speed operation. When CPU core temperatures go higher than these values, it can cause malfunction or CPU breakdown, often known as a "blue screen", and reduce the processor's lifespan. In the present scenario, the smooth surface would cause malfunction, as its maximum temperature, achieved at around 114 s, was almost 80°C. The surface with S = 100 µm would safely perform throughout all the cycle's timespan, with maximum temperature of around 50°C. The design parameter CPU manufacturers provide for cooling systems design is the Thermal Design Power, TDP, which is the maximum heat load generated by the CPU that the cooling system is designed to dissipate in typical operation. Boiling onset and steady-state temperatures on a power step from 0 W to TDP should then stay below the maximum allowed temperatures. On the previous work by Moura [2], a similar transient analysis was performed, although on horizontal surfaces, with major outcome that the critical design parameter is the onset of nucleate boiling, due to the overshoot in the temperature always above steady-state values. The results shown point to different conclusions, as the settled (steady-state) temperatures in many cases were higher than temperature at boiling onset peak, many times not having a peak at all, as in the case of the Smooth surface for all power steps. For steps 20 W and 60 W, surfaces 100 and 200 in fact present their maximum temperatures at onset peak, contrary to higher steps. In fact, it was observed that due to a smooth progression from convective flow to nucleate boiling (h didn't rise sharply), the temperature smoothly increased and stabilized instead of sharply reducing after instantaneous onset of boiling. Nucleation points were progressively activated, being the process slower for the smooth surface and faster for the structured surfaces.

Conclusions can be draught about the current vertical facility, where, much unlike other designs, due to its fully integrated one-chamber evaporator and condenser design, system response does not comprehend onset of boiling peak temperature issues, defining the settled temperature as the critical design parameter to consider.

6.4. Experimental facility: comparison of horizontal and vertical cases

Now that both horizontal steady-state and vertical steady-state and transient cases were presented and analysed (horizontal transient is not of this work's best interest, since the aimed product to develop is in vertical position), a comparison of both steady-state cases is introduced, for better understanding and quantification of improvements. Figure 6.22 represents both horizontal and vertical boiling curves for surfaces Smooth and 200D.

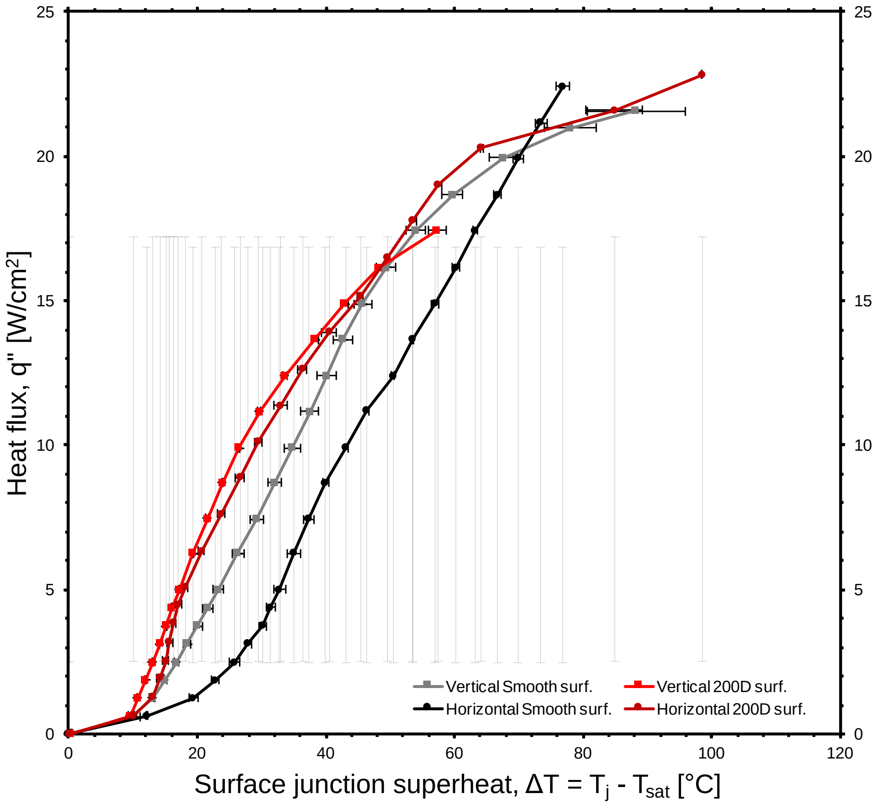

Figure 6.22 - Adapted boiling curves for surfaces 200D and Smooth. [Horizontal and vertical]

For both surfaces, junction superheat temperatures were registered as lower for the vertical case, with a much bigger difference for the smooth surface, with an average 10°C reduction in temperature for the fully developed nucleate boiling regime. As for surface 200D, average reduction was about 2°C. This surface was chosen, being the easiest to compare results, out of the six available structured surfaces.

Regarding our common heat transfer coefficient ratio vs cavity distance surface parameter plot, the following figure displays both vertical and horizontal results and error bars, for comparison purposes. It is important to note that these value sets are not relative to the same heat flux ranges but indeed to equivalent ranges of fully developed nucleate boiling regime. Surface 600 behaves similarly for both orientations, whereas one can witness a gradual improvement in the ratio, as the surface parameter *S* decreases (with special attention to the hybrid surface 42T). Surface 100 shows the largest improvement for vertical against horizontal, roughly 70%. The deeper and wider cavities of surface 200D have shown to behold an improvement of the same scale for both orientations.

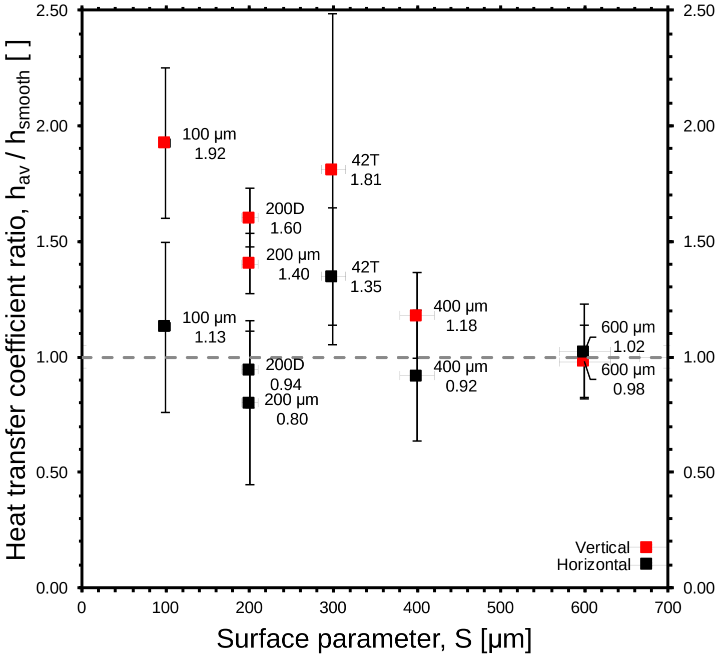

Figure 6.23 - Structured to smooth surface average *h* ratios per surface parameter, *S*. [Horizontal and vertical]

Previous works [46] have stated that a tilted evaporator surface and particularly the vertical surface case would cause a performance reduction. Present results show that this should not always be granted as the rule, as, in fact, for the particular case of a horizontal device with a reflux condenser connected to a cylindrical evaporator by pipes and the pipe-less integrated one-chamber vertical prototype with the same reflux condenser setup, as featured in the present work, the vertical one performs better, benefiting from additional advantages such as being more application oriented to CPU cooling. In fact, CPUs are often mounted in a vertical orientation in a conventional motherboard, inside a desktop computer. Previous figure reinforces conclusions regarding the option for test surfaces of major potential. Two future research directions should address: surfaces with even finer micro-arrays, with *S* parameters smaller than 100 µm; new hybrid surface designs, combining the advantages of different micro-array characteristics, following the success achieved with the prominent 42T surface.

6.5. Vertical prototype in real working conditions

As initially proposed, the developed vertical prototype was tested within its application purpose. It was inserted inside the desktop computer under study, and attached to its CPU unit, a QuadCore Intel® Core i7-2600K with 3600 MHz and Thermal design power, TDP = 95 W, with thermal compound between the prototype cooler's copper surface and the Integrated heat spreader of the processor, as common practice in the CPU cooling field. Figure 6.24 features a photograph of the obtained setup, with the cooler mounted on the CPU unit:

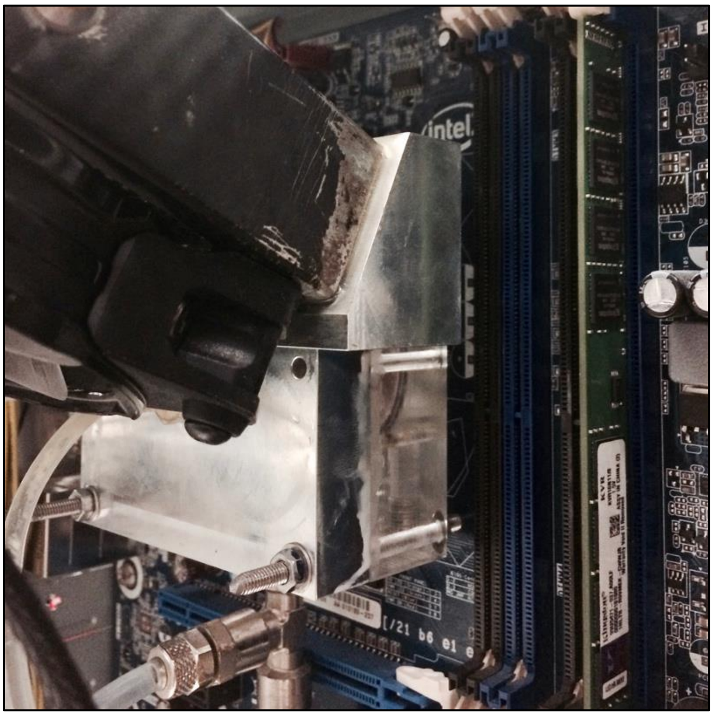

Figure 6.24 - Vertical prototype mounted on Intel motherboard.

As a result of all previous product development efforts, this analysis was crucial to infer if the devised prototype could fit and efficiently provide the cooling needs for the aimed processor. Next section will cover the results obtained after performance tests, both with the cooler and the standard factory installed Intel® fan and heat sink, for comparison and improvement quantification.

6.5.1. Proof of concept transient analysis

With available resources, a transient analysis was performed to the CPU temperature response after an applied heat load profile. Software package AIDA64 for computer diagnosis and benchmark tests was used. Available version allowed for stress tests with a 100% CPU usage load to the four cores only, so every heat load profile would depend in two possibilities: idle CPU usage load, around 16 to 18% or full load, 100%. This prevented the adoption of any kind of more complex heat profile, such as the previously adapted from Isci and Martonosi [64], in section 6.3.2, so a further simplified adapted version, inspired on some of the typical computer routines, as addressed in the previous profile, was adopted. The AIDA64 software additionally allowed for the reading and logging of every internal sensor in the computer, so it was used for obtaining the temperature values [°C], the CPU load [%], as well as fan rotating speeds [RPM] and electric power the processor unit consumes [W]. Figure 6.25 below shows the outcome of the described proceeding. The resulting CPU load profile varies, as mentioned, from idle to full load (stress test mode). The same profile was applied twice, with different equipped cooling technologies, the standard fan and this work's developed cooler. Results show how the temperature response to the resulting dissipated heat behaves differently for each case. In the maximum achieved temperature with the fan, around 00:09:00 time, the cooler resulted in a 12% temperature reduction.

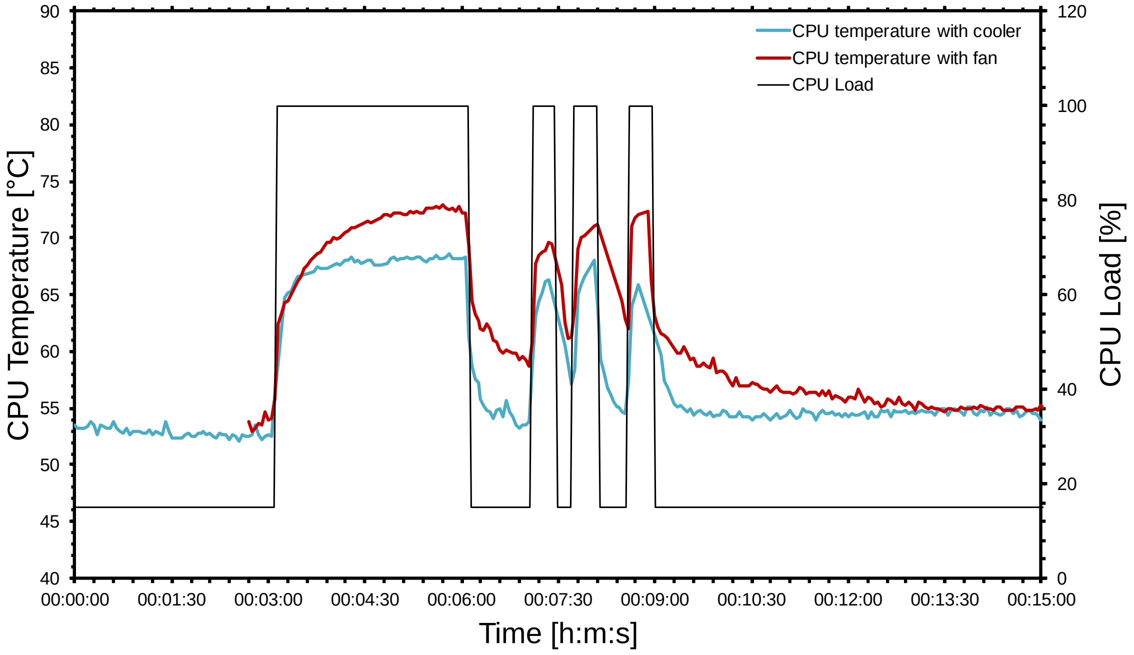

Figure 6.25 - Thermal response to an adapted heat load power profile in real CPU application.

In general, the cooling device presented a significant average 5°C temperature reduction at stress test, with the additional advantage of a lower system response time. In fact, this shorter time response, or, in other words, a better ability to achieve settled temperature after some heat input stimulus, is very significant, since it allows for a faster reduction of temperature when the CPU goes back to idle (or any lower load than before). It takes 4:30 minutes for the fan temperature response to completely reduce to idle temperature, where the cooler temperature response takes less than 1 minute. In the long term, this will improve the lifespan of the CPU unit, which is known to be affected by continuous exposition to high temperatures. One final remark should be stated relative to the surface opted for this real working conditions experiment, which was the Smooth one. Due to results in previous sections, there is a strong suggestion using other structured surfaces could further improve the results obtained at this experiment, so it is left as a suggestion for future work.

7. Conclusions and future work

7.1. Conclusions

The present work covers the test and optimization of an advanced microprocessor cooling product based on a two-phase closed loop thermosyphon, to operate under real conditions, meaning it was tested on a real computer CPU block. A dielectric liquid was used, HFE-7000, with the purpose of direct contact of the CPU's integrated heat spreader or even its core with the cooling liquid, in future optimization iterations. Besides having small to no environmental impact, this fluid also offers excellent thermal characteristics for the operating temperatures range of a typical modern CPU.

Following the previous initial work developed under this product development project, an initial prototype was manufactured in a horizontal surface orientation to first validate the experimental conditions conservation from previous works, while also implementing different design approaches such as the reflux condenser setup. This facility was then tested and surfaces with different cavity distance parameter, S were fully characterized for a steady-state operation mode. A general trend was observed for surfaces with smaller cavity distance parameters S to have lower surface superheats for equivalent heat fluxes, while also the presence of cavities promoted the onset of boiling to occur earlier. On the other hand, high temperature fluctuations were observed for the higher heat flux regimes, due to the reflux condenser setup, with connecting pipes, leading to an earlier onset of critical heat flux.

The same approach was then initially followed for a later manufactured vertical optimized prototype, featuring a single chamber integrated evaporator and condenser design approach, more compact and with no pipes to constrain the flow. Thus, it was also tested at steady-state and the same set of surfaces was fully characterized for further optimization. The single chamber design avoided the previously witnessed temperature fluctuations. Heat transfer coefficient improvement due to changing S parameter was in this case much higher than for the horizontal case. Best performing surfaces regarding h improvement were surface 100 and 42T. Bubbles vertical lateral coalescence was identified as a deteriorating effect in the convective heat transfer, leading to earlier CHF and higher near-CHF wall superheats for surfaces with cavities. On the other hand, at lower heat fluxes, compulsory thermal boundary release through bubble departure and rise along the surface boundary layer was observed as a heat transfer enhancement factor. Overall, the S = 100 µm surface was the best performing.

The ensuing approach consisted in the transient state response characterization of the devised system, with three selected best performing surfaces and with different heat load power inputs consisting of steps and a time-dependent profile. The smooth surface resulted in higher cycle peak temperatures while surface 100 safely performed within the typical allowed CPU temperature range. Contrary to statements in the previous work, the critical design parameter was observed as final settled temperature instead of the onset of nucleate pool boiling.

Finally, results for the horizontal and vertical developed systems were compared and their performance was analysed and interpreted, followed by a study of the real conditions application of the later vertical prototype. It was attached to a real operating Intel® i7 processor and its thermal results at stress test were compared to the conventional air cooling fan core thermal behaviour, showing an average 5°C temperature reduction at stress test, with an additional lower system response time.

7.2. Future work

Results obtained during the vertical facility experimental procedures have shown a trend for heat transfer improvement as the cavity distance parameter S was reducing. The surface 100 was the smallest S parameter tested, with yet improving results, which suggests the further study of finer micro-arrays, with S parameters smaller than 100 µm. On the other hand, the hybrid design surface 42T also showed good results, combining characteristics from different surfaces, which also suggests the further research of new hybrid structuration designs.

During the real conditions application of the devised prototype, only the smooth surface was tested. Future research of structured surfaces in real CPU application for either stress tests (100% CPU load) or overclocking tests (CPU load >100%) should be carried out, with previous results in simulated conditions showing big potential for improvement.

The main reason for the option to choose a dielectric cooling fluid is to follow the target of direct contact between the fluid and the CPU chip encapsulation, eliminating all thermal resistive layers in the way, possibly maximizing the cooling potential. That said, next steps in the current project should address the initial removal of the copper surfaces which were tested, applying micro-array cavities directly onto the factory integrated heat spreader, IHS of the processor, while designing new dimensionally matching prototypes. Afterwards, the final step of optimization should be the evaluation of the feasibility of directly immersing the processor in the working fluid by removing the IHS. While this procedure allows decreasing the thermal resistance of the system, it also dramatically reduces the contact area available to dissipate the thermal power, thus should be subject to extensive research to infer on its effective enhancement of the system performance under these conditions.

Regarding design issues, one of the problems faced while 3D printing was to obtain transparent parts, for flow and boiling visualization, while being able to manufacture complex shapes, made much easier with 3D modelling and printing. Meanwhile, since this work started, there has been development in the available materials for 3D printing state of the art, and the new material HDglass™ should be considered for future component printing. Liquid impermeability, related with leakage issues found during this work should also be high for this material, since transparency requires a very dense compact material solid structure. That said, there is yet a strong potential for 3D printing development for cooling two-phase flow appliances with low saturation temperature fluids.

Other improvements to the cooling device could be thought of, such as artificially reducing saturation pressure under the equivalent to ambient temperature, by means of a molecular vacuum pump and a better sealed chamber, recurring to some product design changes to make it more compact, simple and easy to scale up production.

References

[1] G. E. Moore, “Cramming more components onto integrated circuits,” *Electronics*, vol. 38, no. 8, 1965.

[2] M. Moura, “Design and development of a two-phase closed loop thermosyphon for CPU cooling,” M.S. thesis, Instituto Superior Técnico, Lisboa, 2015.

[3] E. Teodori, A. S. Moita, and A. L. N. Moreira, “Characterization of pool boiling mechanisms over micro-patterned surfaces using PIV,” *Int. J. Heat Mass Transf.*, vol. 66, pp. 261–270, 2013.

[4] J. Hennessy and D. A. Patterson, *Computer Architecture: A Quantitative Approach*. Morgan Kaufmann, 2003.

[5] D. Brooks and M. Martonosi, “Dynamic thermal management for high-performance microprocessors,” *Proc. 7th Int. Symp. High-Performance Comput. Archit.*, no. January, pp. 171–182, 2001.

[6] M. S. El-Genk and H. Bostanci, “Saturation boiling of HFE-7100 from a copper surface, simulating a microelectronic chip,” *Int. J. Heat Mass Transf.*, vol. 46, no. 10, pp. 1841–1854, 2003.

[7] D. A. Hall, G. C. Vliet, and T. L. Bergman, “Natural Convection Cooling of Vertical Rectangular Channels in Air Considering Radiation and Wall Conduction,” *J. Electron. Packag.*, vol. 121, no. 2, pp. 75–84, 1999.

[8] G. P. Peterson, *An Introduction to Heat Pipes: Modelling, Testing and Applications*. New York: Wiley, 1994.

[9] S. S. Tonapi, R. A. Fillion, F. J. Schattenmann, H. S. Cole, J. D. Evans, and B. G. Sammakia, “An overview of thermal management for next generation microelectronic devices,” *ASMC (Advanced Semicond. Manuf. Conf. Proc.*, vol. 2003–Janua, pp. 250–254, 2003.

[10] T. Cader, L. J. Westra, and R. C. Eden, “Spray cooling thermal management for increased device reliability,” *IEEE Trans. Device Mater. Reliab.*, vol. 4, no. 4, pp. 605–613, 2004.

[11] M. R. O. Panão, J. P. P. V Guerreiro, and A. L. N. Moreira, “Microprocessor cooling based on an intermittent multijet spray system,” *Int. J. Heat Mass Transf.*, vol. 55, no. 11–12, pp. 2854–2863, 2012.

[12] I. Mudawar, “Assessment of High-Heat-Flux Thermal Management Schemes,” *IEEE Trans. COMPONENTS Packag. Technol.*, vol. 24, no. 2, pp. 122–141, 2001.

[13] R. C. Chu, “The Perpetual Challenges of Electronics Cooling Technology for Computer Product Applications – from Laptop to Supercomputer,” *Natl. Taiwan Univ. Present.*, 2003.

[14] C. L. M. Lasance and R. E. Simons, “Advances In High-Performance Cooling For Electronics,” *Electronics Cooling*, 2005. [Online]. Available: http://www.electronics-

cooling.com/2005/11/advances-in-high-performance-cooling-for-electronics/.

[15] J. Gorbold, “AMD overclocks Bulldozer to 8.429GHz,” *Bit-tech.net*, 13-Sep-2011.

[16] A. Bar-Cohen, M. Arik, and M. Ohadi, “Direct liquid cooling of high flux micro and nano electronic components,” *Proc. IEEE*, vol. 94, no. 8, pp. 1549–1570, 2006.

[17] M. Moura, E. Teodori, A. S. Moita, and A. L. N. Moreira, “2 Phase Microprocessor Cooling System with Controlled Pool Boiling of Dielectrics over Micro-and- Nano Structured Integrated Heat Spreaders,” *15th IEEE ITHERM Conf.*, 2016.

[18] C. C. J. Vincent and J. B. W. Kok, “Investigation of the overall transient performance of the industrial two-phase closed loop thermosyphon,” *Int. J. Heat Mass Transf.*, vol. 35, no. 6, pp. 1419–1426, 1992.

[19] A. Pal, Y. K. Joshi, M. H. Beitelmal, C. D. Patel, and T. M. Wenger, “Design and performance evaluation of a compact thermosyphon,” *IEEE Trans. Components Packag. Technol.*, vol. 25, no. 4, pp. 601–607, 2002.

[20] H. Farsi, J.-L. Joly, M. Miscevic, V. Platel, and N. Mazet, “An experimental and theoretical investigation of the transient behavior of a two-phase closed thermosyphon,” *Appl. Therm. Eng.*, vol. 23, no. 15, pp. 1895–1912, 2003.

[21] M. Zhang, Z. Liu, G. Ma, and S. Cheng, “Numerical simulation and experimental verification of a flat two-phase thermosyphon,” *Energy Convers. Manag.*, vol. 50, no. 4, pp. 1095–1100, 2009.

[22] T. Inoue and M. Monde, “Operating limit of heat transport in two-phase thermosyphon with connecting pipe (heated surface temperature fluctuation and flow pattern),” *Int. J. Heat Mass Transf.*, vol. 52, no. 19–20, pp. 4519–4524, 2009.

[23] G. B. Wallis, *One-dimensional two-phase flow*. New York: McGraw-Hill, 1969.

[24] T. E. Tsai, H. H. Wu, C. C. Chang, and S. L. Chen, “Two-phase closed thermosyphon vapor-chamber system for electronic cooling,” *Int. Commun. Heat Mass Transf.*, vol. 37, no. 5, pp. 484–489, 2010.

[25] A. Samba, H. Louahlia-Gualous, S. Le Masson, and D. Nörterhäuser, “Two-phase thermosyphon loop for cooling outdoor telecommunication equipments,” *Appl. Therm. Eng.*, vol. 50, no. 1, pp. 1351–1360, 2013.

[26] A. A. Chehade, H. Louahlia-Gualous, S. Le Masson, I. Victor, and N. Abouzahab-Damaj, “Experimental investigation of thermosyphon loop thermal performance,” *Energy Convers. Manag.*, vol. 84, pp. 671–680, 2014.

[27] A. Franco and S. Filippeschi, “Experimental Analysis of Heat and Mass Transfer in Small Dimension, Two Phase Loop Thermosyphons,” *Heat Pipe Sci. Technol. An Int. J.*, vol. 1, no. 2, pp. 163–182, 2010.

[28] M. C. Vlachou, J. S. Lioumbas, and T. D. Karapantsios, “Heat Transfer Enhancement in Boiling

Over Modified Surfaces : a Critical Review,” *Interfacial Phenom. Heat Transf.*, vol. 3, no. 4, pp. 341–367, 2015.

[29] I. Malavasi, E. Teodori, A. S. Moita, A. L. N. Moreira, and M. Marengo, “Wettability effect on pool boiling: a review,” *Encyclopaedia of Two-Phase Heat Transfer and Flow*. Heat Transfer Research, Inc. (HTRI), 2017.

[30] V. K. Dhir, “Boiling heat transfer,” *Annu. Rev. Fluid Mech.*, vol. 30, pp. 365–401, 1998.

[31] D. E. Kim, D. I. Yu, D. W. Jerng, M. H. Kim, and H. S. Ahn, “Review of boiling heat transfer enhancement on micro/nanostructured surfaces,” *Exp. Therm. Fluid Sci.*, vol. 66, pp. 173–196, 2015.

[32] S. S. Kutateladze and I. I. Gogonin, “Growth rate and detachment diameter of a vapour bubble in free convection boiling of a saturated liquid,” *High Temp.*, vol. 17, pp. 667–671, 1979.

[33] M. Poniewski and J. Thome, *Nucleate boiling on micro-structured surfaces*. Warsaw, Lausanne: Heat Transfer Research, Inc. (HTRI), 2008.

[34] M. Jakob, *Heat transfer in evaporation and condensation*. Illinois: Urbana Ill. : University of Illinois, 1937.

[35] B. J. Jones, J. P. McHale, and S. V. Garimella, “The Influence of Surface Roughness on Nucleate Pool Boiling Heat Transfer,” *J. Heat Transfer*, vol. 131, no. December 2009, p. 121009, 2009.

[36] J. P. McHale and S. V. Garimella, “Bubble nucleation characteristics in pool boiling of a wetting liquid on smooth and rough surfaces,” *Int. J. Multiph. Flow*, vol. 36, pp. 249–260, 2010.

[37] T. M. Anderson and I. Mudawar, “Microelectronic cooling by enhanced pool boiling of a dielectric fluorocarbon liquid,” *J. Heat Transfer*, vol. 111, pp. 752–760, 1989.

[38] H. Honda and J. J. Wei, “Enhanced boiling heat transfer from electronic components by use of surface microstructures,” *Exp. Therm. Fluid Sci.*, vol. 28, pp. 159–169, 2004.

[39] L. Dong, X. Quan, and P. Cheng, “An experimental investigation of enhanced pool boiling heat transfer from surfaces with micro/nano-structures,” *Int. J. Heat Mass Transf.*, vol. 71, pp. 189–196, 2014.

[40] M. Shojaeian and A. Koşar, “Pool boiling and flow boiling on micro- and nanostructured surfaces,” *Exp. Therm. Fluid Sci.*, vol. 63, pp. 45–73, 2015.

[41] A. S. Moita, E. Teodori, and A. L. N. Moreira, “Influence of surface topography in the boiling mechanisms,” *Int. J. Heat Fluid Flow*, vol. 52, pp. 50–63, 2015.

[42] J. Gess, S. Bhavnani, B. Ramakrishnan, R. W. Johnson, D. Harris, R. W. Knight, M. Hamilton, and C. Ellis, “Impact of surface enhancements upon boiling heat transfer in a liquid immersion cooled high performance small form factor server model,” *14th IEEE ITHERM Conf.*, pp. 435–443, 2014.

[43] V. Chekanov, “Interaction of centers during nucleate boiling,” *Teplofiz. Vysok. Temp.*, vol. 15, pp. 121–128, 1977.

[44] D. C. Das, K. Ghosh, and D. Sanyal, “A scale analysis model for film boiling heat transfer on a vertical flat plate with wide applicability,” *Int. J. Heat Mass Transf.*, vol. 90, pp. 40–48, 2015.

[45] S. Ishigai, K. Inoue, Z. Kiwakit, and T. Inai, “Boiling heat transfer from a flat surface facing downward,” in *International Heat Transfer Conference*, 1961.

[46] A. H. Howard and I. Mudawar, “Orientation efects on pool boiling critical heat flux (CHF) and modeling of CHF for near-vertical surfaces,” *Int. J. Heat Mass Transf.*, vol. 42, pp. 1665–1688, 1999.

[47] K. Nishikawa, Y. Fujita, S. Uchida, and H. Ohta, “Effect of surface configuration on nucleate heat transfer,” *Int. J. Heat Mass Transf.*, vol. 27, no. 9, pp. 1559–1571, 1984.

[48] K. Ferjančič and I. Golobič, “Surface effects on pool boiling CHF,” *Exp. Therm. Fluid Sci.*, vol. 25, no. 7, pp. 565–571, 2002.

[49] B. Jiao, L. M. Qiu, X. B. Zhang, and Y. Zhang, “Investigation on the effect of filling ratio on the steady-state heat transfer performance of a vertical two-phase closed thermosyphon,” *Appl. Therm. Eng.*, vol. 28, no. 11–12, pp. 1417–1426, 2008.

[50] *McGraw-Hill Dictionary of Scientific & Technical Terms*, 6th ed. McGraw-Hill Companies, Inc., 2003.

[51] S. Nukiyama, “The maximum and minimum values of the heat-Q transmitted from metal to boiling water under atmospheric-pressure,” *Int. J. Heat Mass Transf.*, vol. 27, no. 7, pp. 959–970, 1934.

[52] J. H. Lienhard IV and J. H. Lienhard V, *A heat transfer textbook*. Massachusetts, USA: Phlogiston Press Cambridge, 2004.

[53] T. B. Drew and C. Mueller, “Boiling,” *Trans. AIChE*, vol. 33, p. 449, 1937.

[54] W. M. Rohsenow and P. Griffith, “Correlation of maximum heat transfer data for boiling of saturated liquids,” *Chem. Eng. Prog. Symp.*, vol. 52, no. 18, 1956.

[55] S. S. Kutateladze, “A hydrodynamic Theory of Changes in Boiling Process under Free Convection,” *Proc. Russ. Acad. Sci.*, vol. 4, p. 529, 1951.

[56] N. Zuber, M. Tribus, and J. Westwater, “The Hydrodynamic Crisis in Pool Boiling of Saturated and Subcooled Liquids,” *International Development in Heat Transfer: Proceedings of 1961-62 International Heat Transfer Conference*, Boulder, CO, USA, pp. 230–236, 1961.

[57] J. H. Lienhard and V. K. Dhir, “Extended Hydrodynamic Theory of the Peak and Minimum Heat Fluxes,” NASA CR-2270, 1973.

[58] J. H. Lienhard and M. Z. Hasan, “On Predicting Boiling Burnout with the Mechanical Energy Stability Criterion,” *ASME J. Heat Transf.*, vol. 101, pp. 276–279, 1979.

[59] S. L. Kim, I. C. Bang, J. Buogiorno, and L. W. Hu, “Surface wettability change during pool boiling of nanofluid and its effect on critical heat flux,” *Int. J. Heat Mass Transf.*, vol. 50, pp. 4105–4116, 2007.

[60] F. Incropera, T. Bergman, A. Lavine, and D. DeWitt, *Fundamentals of Heat and Mass Transfer*. Wiley, 2011.

[61] T. Moita, “Evaluation and Development of Advanced Cooling Systems for Microelectronics,” M.S. thesis, Instituto Superior Técnico, Lisboa, 2008.

[62] S. Fiedler and H. Auracher, “Experimental and theoretical investigation of reflux condensation in an inclined small diameter tube,” *Int. J. Heat Mass Transf.*, vol. 47, no. 19–20, pp. 4031–4043, 2004.

[63] T. Klahm, H. Auracher, and F. Ziegler, “Heat transfer during reflux condensation of an R134a/R123 mixture in vertical and inclined narrow tubular and rectangular channels,” *Int. J. Refrig.*, vol. 33, no. 7, pp. 1319–1326, 2010.

[64] C. Isci and M. Martonosi, “Runtime Power Monitoring in High-End Processors: Methodology and Empirical Data,” *Proc. 36th Annu. IEEE/ACM Int. Symp. Microarchitecture*, pp. 93–104, 2003.

[65] R. Abernethy, R. Benedict, and R. Dowdell, “ASME measurement uncertainty,” *J. Fluids Eng.*, vol. 107, no. 2, pp. 161–164, 1985.

[66] T. Fukano, K. Kadoguchi, and H. Imuta, “Experimental study on the heat flux at the operating limit of a closed two-phase thermosyphon,” *Chem. Pharm. Bull.*, vol. 53, no. 487, pp. 1065–1071, 1987.

[67] M. Monde and Y. Mitsutake, “Enhancement of CHF in open thermosyphon with heated bottom chamber,” *Int. J. Heat Mass Transf.*, vol. 43, no. 18, pp. 3341–3346, 2000.

[68] A. S. Moita, E. Teodori, and A. L. N. Moreira, “Enhancement of pool boiling heat transfer by surface micro-structuring,” *J. Phys. Conf. Ser.*, vol. 395, 2012.

[69] T. Valente, “Study of the effects of wettability on pool boiling conditions in a quiescent medium,” M.S. thesis, Instituto Superior Técnico, Lisboa, 2015.

Annexes

A.1. QuickDAQ GUI

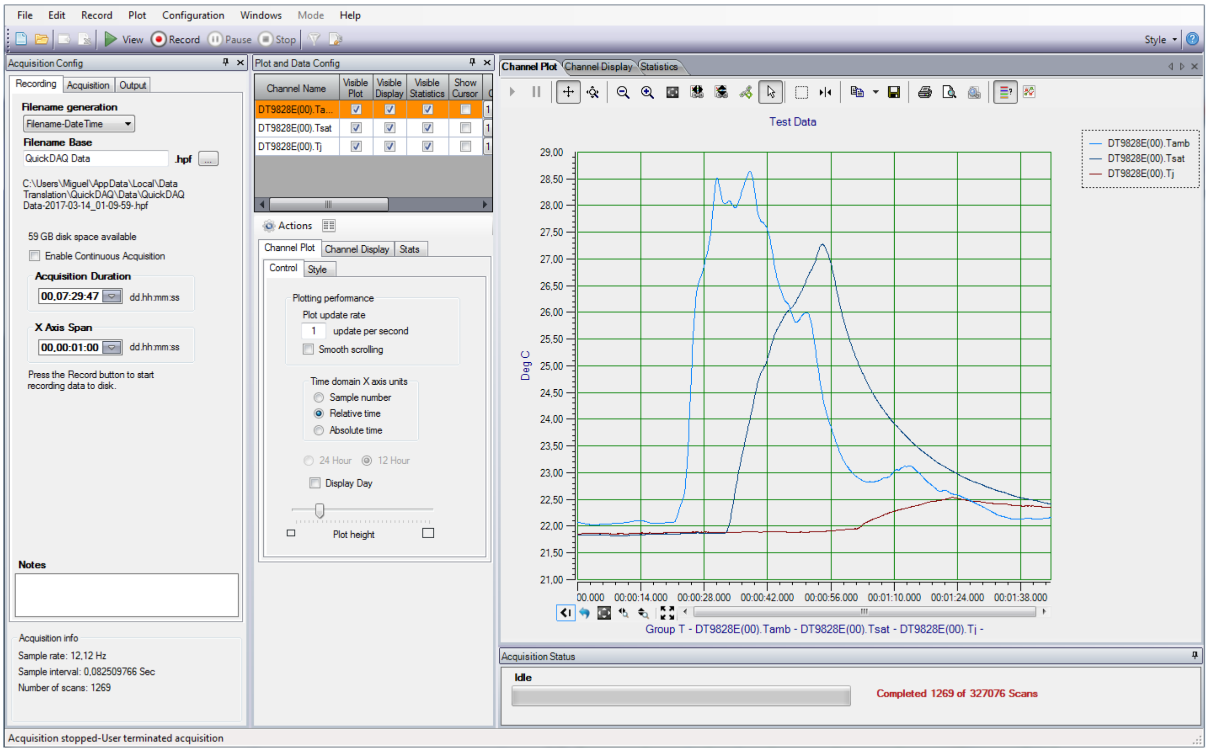

Filename generation

Filename-DateTime

Filename Base

QuickDAQ Data .hpf

C:\Users\Miguel\AppData\Local\Data Translation\QuickDAQ\Data\QuickDAQ Data-2017-03-14_01-09-59-.hpf

59 GB disk space available

☐ Enable Continuous Acquisition

Acquisition Duration

00,07:29:47 dd.hh:mm:ss

X Axis Span

00,00:01:00 dd.hh:mm:ss

Press the Record button to start recording data to disk.

Notes

Acquisition info

Sample rate: 12,12 Hz

Sample interval: 0,082509766 Sec

Number of scans: 1269

Channel Name	Visible Plot	Visible Display	Visible Statistics	Show Cursor
DT9828E(00).Ta...	☑	☑	☑	☐
DT9828E(00).Tsat	☑	☑	☑	☐
DT9828E(00).Tj	☑	☑	☑	☐

Plotting performance

Plot update rate

1 update per second

☐ Smooth scrolling

Time domain X axis units

○ Sample number

● Relative time

○ Absolute time

○ 24 Hour ● 12 Hour

☐ Display Day

Plot height

Idle

Completed 1269 of 327076 Scans

Acquisition stopped-User terminated acquisition

A.2. LabVIEW GUI

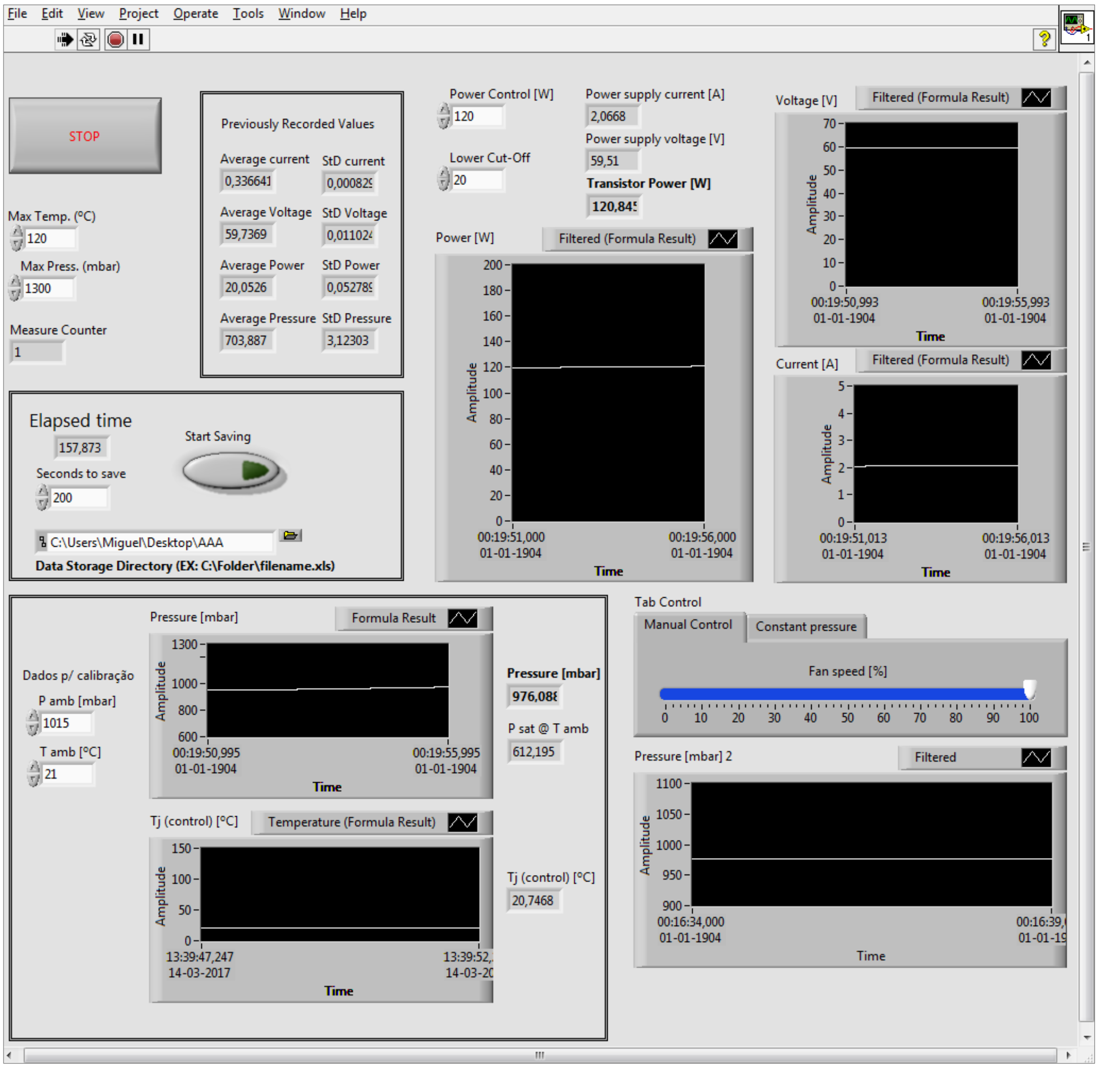

Max Temp. (ºC) 120

Max Press. (mbar) 1300

Measure Counter 1

Previously Recorded Values

Average current 0,336641	StD current 0,00082
Average Voltage 59,7369	StD Voltage 0,01102
Average Power 20,0526	StD Power 0,05278
Average Pressure 703,887	StD Pressure 3,12303

Power Control [W] 120

Lower Cut-Off 20

Power supply current [A] 2,0668

Power supply voltage [V] 59,51

Transistor Power [W] 120,84

Elapsed time 157,873

Seconds to save 200

C:\Users\Miguel\Desktop\AAA

Data Storage Directory (EX: C:\Folder\filename.xls)

Dados p/ calibração

P amb [mbar] 1015

T amb [ºC] 21

Pressure [mbar] 976,08

P sat @ T amb 612,195

Tj (control) [ºC] 20,7468